DEVELOPMENT OF SIMULATION TECHNOLOGY FOR FORMING OF ADVANCED HIGH STRENGTH STEEL

By
XIAOMING CHEN

A Thesis Submitted to the School of Graduate Studies
In Partial Fulfilment of the Requirement for the
Degree of Doctor of Philosophy

McMaster University Doctor of Philosophy (2012) Mechanical Eng.

TITLE: Development of Simulation Technology for Forming of Advanced High Strength Steel

AUTHOR: Xiaoming Chen, B.Eng. and M.A. Sc (University of Science and Technology, Beijing)

SUPERVISOR: Dr. Peidong Wu

Pages: xv, 150

ABSTRACT

Advanced high strength steels (AHSS) exhibit significant higher springback and different fracture modes in forming processes and these problems cannot be accurately predicted using conventional simulation methods in many cases. In this thesis, new simulation technologies have been developed to improve the predictability for AHSS forming. The technologies integrated various aspects of simulation techniques, including development of material models and local formability criteria, calibration of the models with experimental data, and simulation method and parameter optimisations. Both laboratory and full scale parts were used to validate the simulation technologies developed. These technologies are originally applied to solve AHSS forming problems.

The springback predictions have been significantly improved using the newly developed simulation technology. The technologies include the implementation of the smooth contact to reduce contact errors, modification of mass scaling to reduce dynamic effect, implementation of isotropic/kinematic hardening model and optimization of simulation parameters. Shear fracture (a stretch bending fracture on a small radius) have been successful predicted using Modified Mohr Coulomb (MMC) fracture criterion. Both laboratory experiments and full scale parts have been used to validate the predictions. Shearing and pre-forming effects on hole expansion and edge stretching have been investigated. A new approach was introduced to evaluate AHSS sheared edge deformation and quality by measuring material flow line angle change on a shearing edge. Shearing processes were simulated using MMC failure criterion and the sheared edge deformation has been integrated to hole expansion simulation to produce a more accurate prediction. The pre-forming effect on edge cracking has been investigated through both experiments and simulations. The limit strains have been measured by experiments. Simulation technology was also developed to predict surface strains of pre-form and subsequent stretching. Formulation of plane stress characteristics considering normal anisotropy have been developed and applied to analyze the flange deformations and optimum blanks for cup drawing. The method of plane strain characteristics has been used to predict earing throughout the entire cup drawing process.

ACKNOWLEDGEMENT

I would like to gratefully acknowledge my supervisor, Dr. Peidong Wu, for his excellent guidance, encouragement, patience and support for the completion of my thesis.

I would like to thank Dr. Joseph McDermid and Dr. Mateusz Sklad for their great advice and support to my thesis work.

It is with great grief that I wish to express my remembrance to the passing of Dr. Robert Sowerby. I will always remember the times I spent with him when he was my first PhD supervisor. He spent a lot of time advising and guiding me in my research and assisting me with life in Canada. I will always remember his professionalism and his kindness.

Finally, I would also like to deeply thank to my wife, Jianqi He, for her patience, understanding and great support.

TABLE OF CONTENT

LIST OF FIGURES

LIST OF TABLES

LIST OF ABBREVIATIONS AND SYMBOLS

σ	Stress tensor
σ_{ij}	Stress component in i plane and j direction, e.g. σ_{xy} . is the stress component in x plane and y direction.
σ_n	Normal stress
$\bar{\sigma}$	Equivalent stress
τ	Shear stress
ε	Strain tensor
$\bar{\varepsilon}_f$	Equivalent stain at fracture
ε^p	Plastic stain
$d\lambda$	Proportionality in flow rule
η	Stress triaxiality $\eta = -p/\bar{\sigma}$
p	Hydrostatic pressure
α , β	Co-ordinate axis in the slip line field
θ	Lode angle
φ , ω	Parameters used for plane stress characteristics
ϕ	The anticlockwise rotation from the x-axis to the maximum algebraic principal stress
C_1, C_2, C_3	Material parameters for MMC fracture criterion
J_2, J_3	First and second invariants of stress deviator
D	Damage factor
n	Exponent for power law of work hardening

$\overline{R}$	Average Lankford anisotropic ratio of three different sheet orientations
R/t	Ratio of radius over thickness
Vx , Vy	In-plane components of velocity.
BUT	Bending under tension
CP	Complex phase steels
DIC	Digital image correlation
DP	Dual phase (e.g. DP780 means dual phase steel with minimum tensile strength of 780 MPa)
DQSK	Draw quality special killed
F, G, H	Anisotropic parameters in Hill's yield criterion
FEA	Finite element analysis
FEM	Finite element method
FLC	Forming limit curve
HER	Hole expansion ratio
HSLA	High strength low alloy
HSS	High strength steel
MMC	Modified Mohr-Coulomb
MS	Mass scale
NDST	Newly developed simulation technology
PSC	Plane Stress Characteristics
RD	Rolling direction
SFS	Stretch forming simulator
SLF	Slip line field

TD	Transverse direction
TS	Tensile strength
TE	Total elongation
TRIP	Transformation Induced Plasticity
YS	Yield strength

ACADEMIC ACHIEVEMENT

Four papers have been published:

1. Xiaoming Chen, Ming F. Shi, Xinghai Zhu, Changqing Du, Z. Cedric Xia, Siguang Xu and Chuan-Tao Wang, "Springback Prediction Improvement Using New Simulation Technologies", SAE Technical Paper 2009-01-0981.

2. Xiaoming Chen, Meng Luo, Ming F. Shi, Hua-Chu Shih and Tomasz Wierzbicki, "AHSS Shear Fracture Predictions Based on a Recently Developed Fracture Criterion", SAE technical paper, 2010-01-0988.

3. X. Chen, C.Du, X. Wu, X. Zhu, and S-D. Liu, "Sheet Metal Shearing and Edge Characterization of Dual Phase Sheets", IDDRG International Conference, June 2009.

4. Xiaoming Chen, Ke Chen, Lorenzo Smith, "Pre-Forming Effects on AHSS Edge Cracking ", Proc. of Numisheet 2011, Soul, Korea.

Author's contribution:

Developed new simulation technologies to improve the predictability for AHSS forming. The technologies integrated various aspects of simulation techniques, including development of material models and local formability criteria, calibration of the models with experimental data, optimisation of simulation parameters and validations with test data of both laboratory and full scale parts. These technologies are original work applied to solve the issues of AHSS forming.

CHAPTER 1. INTRODUCTION

Advanced high strength steels (AHSS), usually refer to are implemented extensively in automotive applications. These include dual phase (DP) steels, transformation induced plasticity (TRIP) steels and multi-phase steels. AHSS are capable of combining high strength with good ductility, high work hardening capability and high bake hardenablility. These characteristics permit the fabrication of components with complex geometries and in-panel material strengths far exceeding those of conventional high strength grades of steel. AHSS components provide an opportunity to improve the structural integrity and crashworthiness of an automotive body while reducing the overall weight of the vehicle. Figure 1.1 shows an automotive front end structure. After redesigning with AHSS, 23% weight reduction was achieved with the same performance [1]. As a result, AHSS are currently becoming more popular in the automotive industry to increase fuel economy while maintaining safety requirements. Figure 1.2 shows the trend of AHSS used per vehicle in North America [2]. In 2000, few parts used AHSS. In 2009, approximately 150 lbs. of AHSS were used per vehicle. This number is expected to triple by 2020.

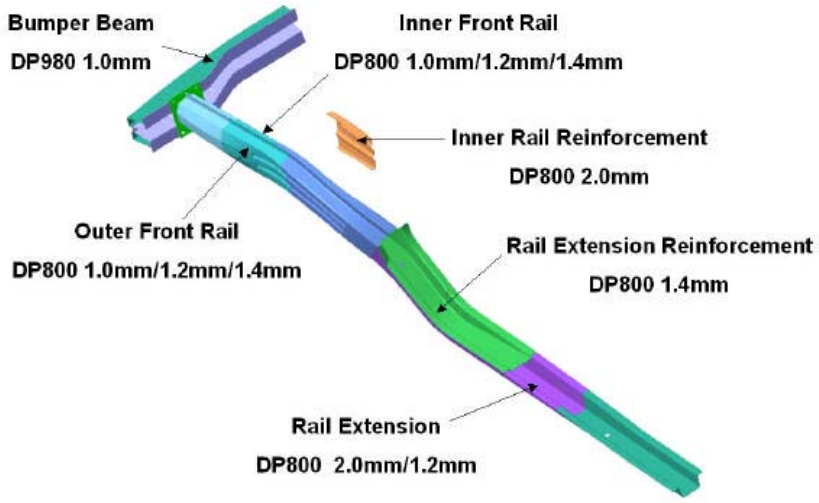

Figure 1.1. Automotive front end structure, 23% weight reduction is achieved after redesigning using AHSS.

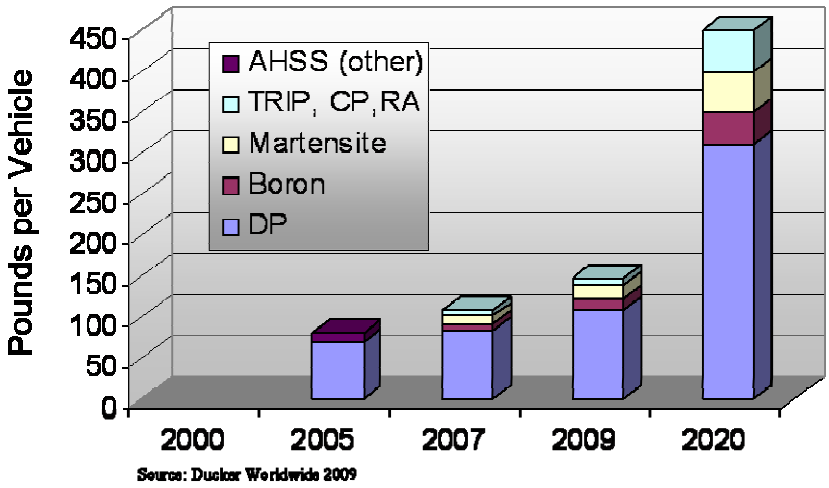

Figure 1.2. The trend of AHSS growth in North American vehicles

Although AHSS have many advantages, several manufacturing issues arise during the stamping process, which include springback, stretch bending fracture in a tight radius (shear fracture), and edge cracking [3]. These issues have become a barrier for further

applications of AHSS. To eliminate these problems, various laboratory experiments and process trials have been conducted to understand and improve the manufacturability of AHSS. However, most of the tryouts involved trial-and-error procedures, which were both costly and time consuming. Therefore, the development of computer simulations to aid in the prediction of AHSS forming was highly demanded.

Computer simulations are widely used to assist in various aspects of product design and manufacturing processes. There are two major applications of these simulations which can be applied to metal forming processes. One application is used in estimation and early process design stage. For this application, the simulations must be easy to use, quick to provide blank geometry, and have the ability to provide approximate information to determine the processes required to fabricate the part. In addition, the simulations can be used to conduct a manufacturing feasibility study and to provide information for structural design analyses. The second application is for a detailed forming analysis, when most of the die and process information is available. A simulation is used at this point for die geometry and process confirmation. It can also be used for process troubleshooting and to solve production problems such as the AHSS forming issues mentioned above.

In this thesis, computer simulation technologies for these two applications have been developed. Experimental data has been generated for material models and failure criteria of AHSS. The material models and failure criteria have been incorporated with finite element methods (FEM) to develop simulation methodologies for AHSS forming analyses. Simplified simulation methods have also been developed which are quick and user-friendly for early stage metal forming analyses and blank development.

Significant savings have been achieved using the simulations to replace trial and error processes. For example, usually the AHSS springback trials require three to four times die re-cutting to make a good part; in some instances, a die might be re-machined up to 10 times. Using simulation technology reduced the re-cut time to one or two times, and for most cases, only one cut was necessary. One die re-cutting process usually costs approximately $5000. Therefore, the savings per part may be $20,000 to 100,000. Another example of the advantages of accurate simulation technology is a stamping line that was shut down due to an edge cracking problem (100% reject rate). Simulations were used to re-design the tools and process, and the edge cracking problem was eliminated by implementing the new designed tools.

CHAPTER 2. REVIEW OF AHSS FORMING

2.1. Overview of AHSS

2.1.1. Microstructure Characteristics

A brief introduction of the micro-structure will help to understand AHSS better because the definition of AHSS is primarily based on their micro-structure [4].

Dual phase (DP) steels

Dual phase steels consist of a soft ferritic matrix containing a hard martensitic second phase in the form of islands. They use composite strengthening to obtain high strength while maintaining substantial ductility, where martensite acts as the strengthener, and ferrite provides the necessary ductility. The martensite islands create a higher initial work hardening rate, which gives DP steels much higher ultimate tensile strengths than conventional steels of similar yield strength. The strength generally increases with increasing volume fraction of hard second phases. Figure 2.1 (a) shows a schematic microstructure of DP steel and (b) an actual DP780 micro-structure. The martensite morphology, as well as volume fraction can vary widely depending on processing [4]. The shape, size and distribution of the martensite islands influence the behavior of deformation such as directional property and fracture mechanism.

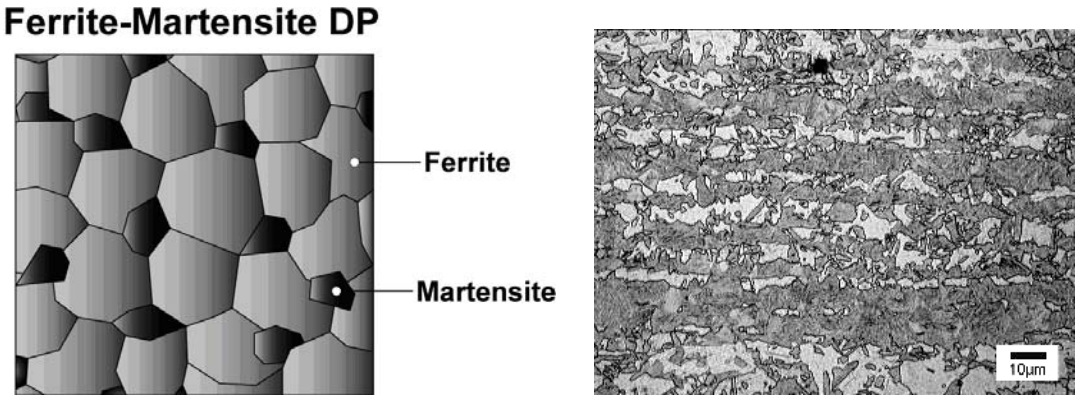

(a) (b)

Figure 2.1. (a) Schematic microstructure of DP steel (b) Micro-structure of DP780.

Transformation Induced Plasticity (TRIP) steels

The microstructure of TRIP steels consists of retained austenite embedded in a primary matrix of ferrite. In addition to retained austenite, hard phases such as martensite and bainite are present in varying amounts. The retained austenite progressively transforms to martensite with increasing strain, thereby increasing the work hardening rate at higher strain levels. A schematic TRIP steel microstructure is shown in Figure 2.2 (a) and an actual micro-structure of TRIP780 in (b).

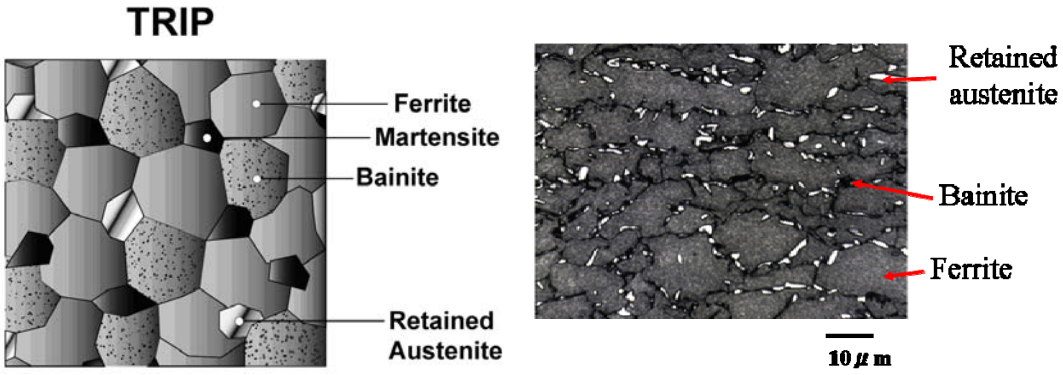

(a) (b)

Figure 2.2. (a) Schematic microstructure of TRIP steel (b) Micro-structure of TRIP780.

Complex Phase (CP) Steels.

The microstructure of CP steels consists of a fine ferrite matrix which contains a high volume fraction of hard phases and is further strengthened by fine precipitates. Complex phase steels typify the transition to steel with very high ultimate tensile strengths.

Martensitic (Mart) Steels

Martensitic steels are processed when the existing austenite present during hot rolling or annealing is transformed entirely to martensite during cooling. This structure can also be developed with post-forming heat treatment. Martensitic steels have the highest strengths with ultimate tensile strengths of up to 1700 MPa.

2.1.2. Mechanical Characteristics

The AHSS most used in automotive applications are the DP and TRIP steels. Figure 2.3 shows the engineering stress-strain curves of various DP and TRIP steels [3]. The tensile strength increases as the volume fraction of hard phases increases. To compare the work hardening behavior, Figure 2.4 shows the stress-strain curves of HSLA (high strength low alloy) steel, DP and TRIP steels with similar yield strengths. In general, the DP steels have a substantially higher initial work hardening rate. TRIP steel has a lower initial work hardening rate than DP steel. However, the hardening rate persists at higher strains; where the work hardening of the DP steel begins to diminish. The overall work hardening rates of TRIP and DP steels are substantially higher than that of conventional high strength steels (HSS), and as a result, these steels have significantly higher ultimate tensile strengths. The TRIP steel also has a higher total elongation, which results in better ductility during plastic forming. The area under the stress-strain curve represents

the strain energy absorbed during a tensile test. The areas under the curves for the DP and TRIP steels are much larger than that of HSLA. Therefore, components made by DP and TRIP steels absorb much more energy during a crash event [5,6].

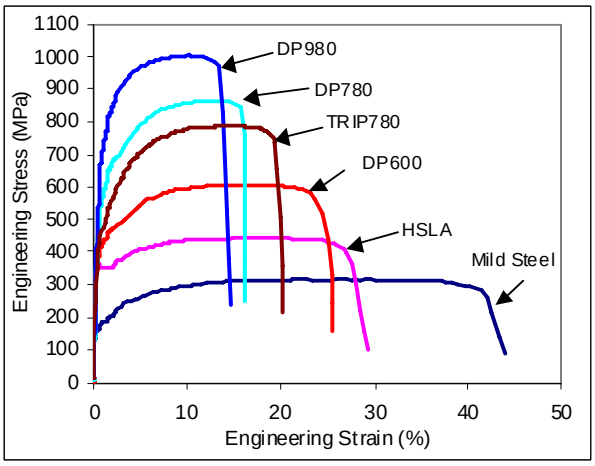

Figure 2.3. Engineering stress-strain curves of various DP and TRIP steels.

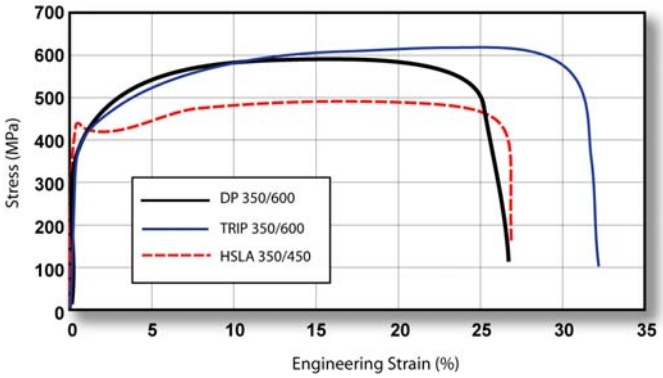

2.4. Stress-strain curves of HSLA, DP and TRIP steels with similar yield strengths.

AHSS have a much better combination of strength and ductility compared to conventional HSS as shown in the elongation-strength diagram (Figure 2.5) [4]. For the same magnitude of elongation, the strength of AHSS is much higher. In addition, AHSS

have higher bake hardenability than conventional HSS. The bake hardening effect is the increase in yield strength resulting from aging at elevated temperatures after prestraining. The extent of the bake hardening effect in AHSS depends on the specific chemistry and thermal histories of the steels. A formed AHSS panel can gain more than 40 MPa in strength after baking in a painting oven [7], therefore its dent resistance can be improved.

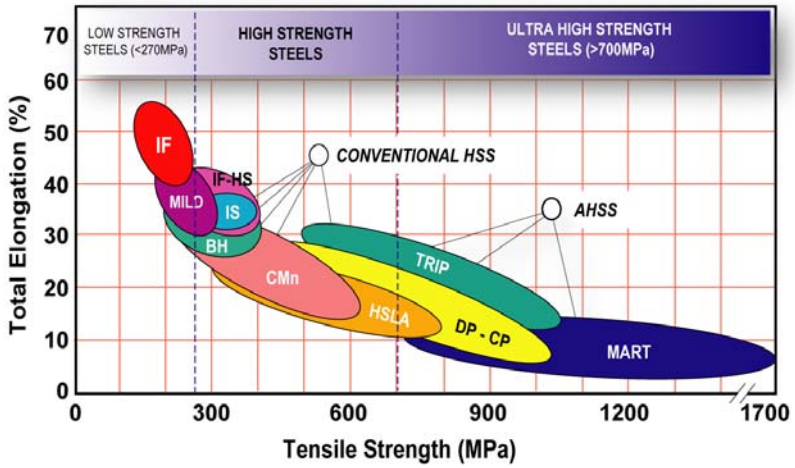

Figure 2.5. Strength and elongation diagram.

2.1.3. Fracture and Formability

Figure 2.6 (a) shows scanning electron microscope (SEM) images of a fractured automotive part composed of DP steel [8]. The image shows a dimple structure with a number of pores. The pores are a result of micro-void nucleation and coalescence. Figure 2.6 (b) shows the initiation of fracture during a tensile test of DP980 steel. Diffuse necking is observed. This indicates that the fracture is a ductile rupture which is similar to the ductile fracture of conventional steel. As a result, the conventional forming limit curve (FLC) can be used for general formability prediction of AHSS. This has been supported by dome test experiments for FLC measurement [9]. The

experimental data is very close to values calculated by Keeler/Brazier empirical equations [10]. A simulation study to verify the usability of FLC to AHSS is presented in [11].

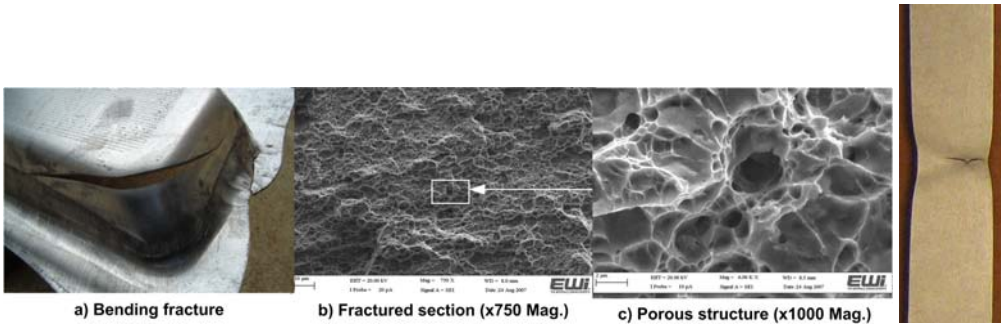

(a) (b)

Figure 2.6. (a) SEM images of a fractured automotive part of DP steel (b) Necking is observed in fracture initiation of a DP980 tensile test [8].

2.1.4. AHSS Forming Issues

Although the empirical FLC can be used to predict the general forming failure of AHSS, it fails to predict local formability. In the case of local formability such as edge cracking and shear fractures, the fracture mechanisms are very different and the failure strains are much lower than predicted by FLC. In sheared edge stretch, the sheared edge was damaged in the previous shear operation. In shear fracture, the deformation gradient changes rapidly from the inner to outer surface. The interface between the islands of hard martensite and the soft matrix of ferrite are potential sites for void nucleation and early fracture. This early fracture can affect hole expansion, edge stretch, bending and other highly localized modes of forming [4]. Since edge cracking and shear fracture cannot be predicted using conventional FLC, the initial design of tools and processes may not be reliable for stamping production. Issues have been raised in many stamping cases.

Another forming issue of AHSS is springback, which is also difficult to predict accurately using the conventional simulation technology. To reduce the cost and time, further investigation is required to improve the predictability of AHSS forming. More detailed review will be given in the following sections for these three major AHSS forming issues:

- Springback
- Shear fracture
- Edge cracking

2.2. AHSS Springback

2.2.1. Springback Experiments and Trials

Springback is the geometric change of a formed part after release from the stamping die. AHSS parts usually undergo more springback than conventional high strength and mild steels. Figure 2.7 shows the springback of an automotive load beam made with various AHSS. It can be seen that the degree of springback increases as the material strength increases [12, 13]. Keeping the springback under control during forming is crucial for minimizing dimensional problems in assembly. Various laboratory experiments and production trials have been conducted to investigate the tooling and process effects on springback. Some successful cases have been reported using in-process control methods such as optimizing die gaps, using variable blank holding forces, floating draw bead by increasing the part stretch at the last drawing stroke, using a step flange to increase side wall stretch, and adding product features and stiffening beads, etc.

[12-15]. The objectives of these approaches are to increase panel stretch, to obtain a more uniform forming stress distribution through the sheet thickness or to increase the panel stiffness [16, 17]. In an L-bend springback analysis, Kadkhodayan et al. [18] showed that a higher amount of equivalent plastic strain causes a smaller amount of springback at the end of the process. These experiments and trials provided useful information for springback control. However, most of the tests involved trial-and-error procedures. To increase the efficiency of these approaches, understanding the root cause of springback is critical. Accurate prediction using computer simulation is very important to assist solving springback issues in a time and cost effective manner.

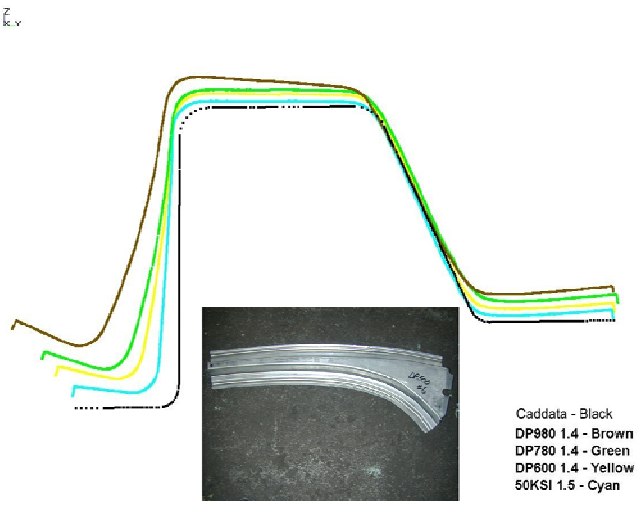

Figure 2.7. Springback of an automotive load beam, springback increases as the material strength increases.

2.2.2. Modeling Springback

Although a high level of confidence has been built in predicting formability and wrinkling in metal forming processes, it remains a challenging task to accurately predict springback, particularly for those parts with twist and sidewall curl. Springback

simulation is a complicated process, since it involves large and non-uniform deformation in different forming stages followed by elastic unloading to obtain a correct residual stress distribution. Many studies have shown that the prediction accuracy was case-dependent, as it can be satisfactory for some cases, but highly inaccurate for others. For example, 40% prediction error was reported for a channel type analysis when using a DP980 steel [13]. An underestimate of the experimental data was usually reported when using an isotropic or kinematic hardening model [19]. One major reason for poor springback prediction is due to the complexity of the stress state before springback takes place. Springback is caused by different membrane stresses in flanges and bending stresses transversally through the sheet thickness. Shape deviations due to different membrane stresses can be calculated correctly, however, shape deviations caused by bending stresses across the sheet thickness are harder to predict [20, 21].

Great effort has been made to improve the prediction accuracy of springback for more than a decade. Numerous studies have been carried out to understand root causes and improve the simulation technology [22-30]. Bui et al. [22] utilized the enhanced strain control technique for locking removal in numerical simulation of springback. Papeleux and Ponthot [23] discussed numerically the effect of blank holding force, friction, spatial integration, etc. on the forming response. Chou and Hung [24] carried out FEA to simulate several springback reduction techniques used in "U" channel bending. These include over-bending, stretching, arc bottoming, die pinching, spanking and movement (double bend) methods. Effects of the die radius, die clearance and material type on springback have also been investigated [13, 18]. A global co-operation effort to

improve the prediction capability can be seen in the Numisheet Conferences. In every conference, benchmark samples for springback experiments and simulation correlations were published [31-36]. Many researchers worldwide participated in the benchmark activities. This great effort of research has led to a steady improvement in simulation technology. The key variables which are important to springback simulations are reviewed below.

2.2.3. Parametric Study

A forming simulation is conducted before the springback effect is analyzed. A dynamic explicit method is usually used where original parameters are selected for crash simulations. This parameter setting usually produces a reasonably good strain distribution for formability predictions, but does not provide sufficiently accurate stress results for the subsequent springback simulations. The predicted accuracy is very sensitive to the parameters selected, therefore, parameter optimization is required for more accurate springback predictions [13, 17, 30, 39, 40]. Many sensitivity studies were previously conducted which explored parameters such as the mesh size, number of integration points through thickness, simulation speed, contact penalty factor, etc. [37,46].

Wagoner et al. [37] indicated that more than 30 integration points were needed to obtain an accurate through-thickness stress distribution. Other studies showed that significantly fewer integration points were required to model the bending/unbending accurately in comparison with the analytical solution [38]. In cases of large scale part

analysis, fewer than 10 points were typically used to reduce the computational cost. The accuracy was sufficient in most cases [39, 17, 30].

Springback simulation results are sensitive to the element used and therefore element formulation, type, size and adaptive meshing were analyzed in many publications [17, 39, 40]. The publications reported that fully integrated shell elements need to be used. Furthermore, the element size should be adequate and the cover angle of one element should not exceed 15 degrees in the bending radius region [17, 39]. Ma et al. [41] verified that both solid and shell elements provided good results in simulations of two Numisheet benchmark samples.

The contact method used in the forming simulation is another important factor which affects the accuracy of springback prediction. In the conventional approach, the contact force is very sensitive to the contact parameter selection and tool mesh size. These are often sources of computational errors and produce user-dependent springback predictions. To overcome this problem, a better contact approach needs to be developed [30, 40]. Simulation speed also influences the accuracy when using a dynamic explicit code for forming simulations[19, 30, 40]. Higher speeds will reduce computational time, but will introduce a dynamic effect and thus increase the probability of error in stress calculations. A balance value is obtained by experience. Young's modulus (E) is also an important parameter because springback is a process in which there is a release of elastic stress. Some studies showed that the modulus is not constant during unloading, therefore a non-linear modulus may need to be considered in springback computations [45, 46].

2.2.4. Material Model Study

The accuracy of sheet metal forming and springback simulations depends not only on the forming conditions (friction, tool and binder geometry etc.), but is also affected by material properties (YS, TS and work hardening), anisotropy, and cyclic hardening characteristics [19, 30, 40, 47]. Experimental data show that higher tensile strength steel will yield higher springback [15, 17]. The material constitutive law plays an important role in describing the mechanical behavior of sheet metals. Therefore the relation among the material parameters must be determined with high precision, since it is essential to obtain an accurate stress distribution in a formed part to predict springback In a deep drawing process, the material undergoes bending, unbending, stretching, and compression, often resulting in a load reversal. After a load reversal, a so-called "Bauschinger effect" can occur. The "Bauschinger effect" is described by a reduction of the yield stress when the loading direction is reversed [20]. AHSS exhibited non-linear unloading and a more severe Bauschinger effect than conventional high strength steels and mild steels. The conventional isotropic hardening model cannot accurately describe these behaviors, especially when the material is subjected to bending and unbending during forming [30]. A more advanced material model such as nonlinear isotropic/kinematic hardening material model must be incorporated in AHSS springback simulations [40, 47, 56].

A great deal of research has been dedicated to develop new constitutive models aiming at better springback prediction [47-57]. Li et al. [49] examined the effects of the modulus of material hardening in 'V' bending simulations. They showed that the

material-hardening model directly affects the springback simulation accuracy. The two most popular kinematic hardening models are Chaboche [50], and Yoshida-Uemori [47, 48]. The later one gives a more detailed description of the AHSS material behavior. Yoshida and Uemori developed a constitutive model of large-strain cyclic plasticity that describes the transient Bauschinger effect as well as the work hardening stagnation which appears when deformation is reversed. This model can be used with any type of anisotropic yield function, such as those by Hill (1948 [58], 1990 [59]) and Gotoh [60]. It is also able to simulate stress-strain responses in biaxial deformations with stress path changes [51]. Several simulations using the Yoshida material model showed a significant improvement in prediction accuracy [30, 41, 56].

2.2.5. Springback Compensation

Springback can be compensated by die design techniques such as over-crowning, under-crowning, over-bending, or under-bending. After many years of study, the simulation technology and prediction accuracy have improved steadily. Accurate prediction makes it possible to design compensated tools and processes virtually in a computer. Many compensation examples have been tried and favorable results have been obtained [26, 41, 51, 61].

2.2.6. Summary of Springback Review

A great deal of research has focused on improving springback predictions. As a result, simulation capability and accuracy have made steady improvements. Key

simulation variables have been identified. These parameters include element type, size and formulation, simulation speed and contact approach. Parameter optimization must be carried out for AHSS application. In addition, the material model is an important factor for springback prediction. A kinematic hardening model must be considered for AHSS springback simulation.

2.3. Shear Fracture

Stretch bending failure (commonly known as shear fracture) refers to fracture in the bending radius region as the material is subjected to stretch bending over a sharp radius. Comparing to conventional steels, AHSS shear fracture occurs in a larger ratio of die radius to thickness (R/t). Insignificant material thinning is often observed with this type of fracture. The forming strain limit may be overestimated by the conventional forming limit curve (FLC). Figure 2.8 shows the stretch bending failure of an automotive underbody structural part made of DP780 steel. Fracture was not predicted by the simulation using the FLC [62] although the FLC has been used successfully for conventional steel failure predictions. Therefore an alternative prediction approach is required.

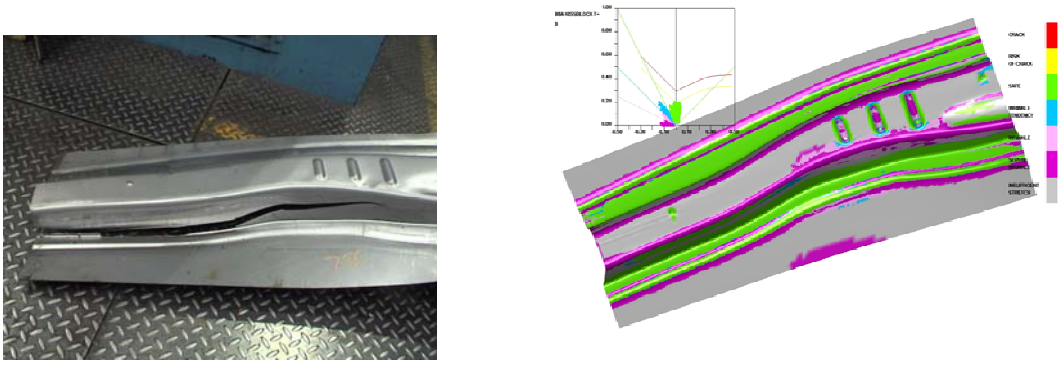

(a) (b)

Figure 2.8. (a) An example of stretch bending fracture, (b) It is not predicted by FLC.

2.3.1. Experimental Work

To find an alternative failure criterion for AHSS, various types of experiments have been conducted. The bending under tension test (BUT) was used in several shear failure studies [63, 8, 64], as shown in Figure 2.9. In this test, tension is directly imposed to a sheet which is pulled over a pin. The tension level can be adjusted and the pin radius is systematically altered to obtain a change in fracture mode. The effects of unbending and friction are incorporated, which simulates industrial stamping operations more accurately. Figure 2.10 shows selected BUT specimens from a study by Shih and Shi [63]. As the die radius increases, the fracture mode changes from shear fracture to tension-type fracture.

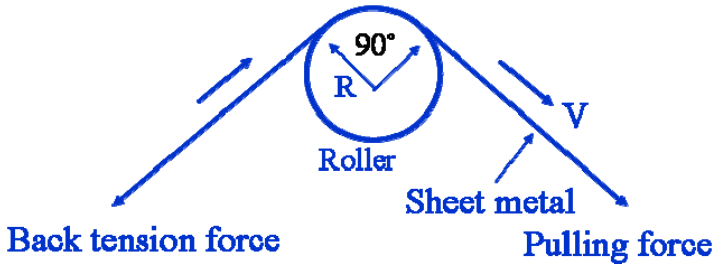

Figure 2.9. Schematic of BUT test.

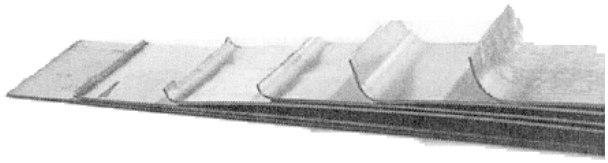

Figure 2.10. Experimental DP780 specimens from BUT tests. The fracture mode change when increasing die radius [63].

A sheet thickness-normalized die radius (R/t), can be used as a measure of BUT formability results. They are typically plotted as an engineering stress value (pulling force at failure divided by original cross sectional area) versus R/t. The trend shows an increase at low radii (greater slope), which saturates at large radii. This trend is shown in Figure 2.11 for a DP780 steel. Similar trends were found for other AHSS including a TRIP780 and a DP980 material. The transition point is the boundary of shear fracture. Shear fracture occurs on the left side of the transition point. The figure also shows that higher strength materials tend to fail at higher stresses given a fixed radius, but show a significantly greater drop in failure stress compared to the tensile strength of the material at low radii. Kim et al. [8] reported that the pulling speed had an effect on shear fracture. Plotting the results as the sliding distance vs R/t shows the shear fracture transition more

clearly. It was also reported that the temperature increased higher for the DP steel during BUT testing, which reduces the formability in stretch bending [65]. Hudgins et al. [64] studied the microstructure and mechanical properties related to shear fracture. The results suggested that little correlation was observed between martensite morphology and critical R/t values, but that increasing yield strength resulted in a material less susceptible to shear fracture. In an earlier study, Walp et al. [66], used a modified Duncan Shabel tester, to examine DP600, CP800, TRIP800, and DP800. Similar results were found and are shown in Figure 2.12.

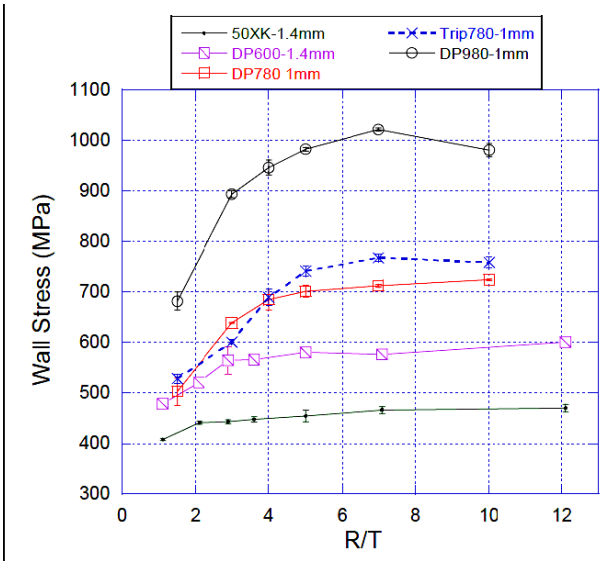

Figure 2.11. Result plot of BUT tests for various AHSS [63].

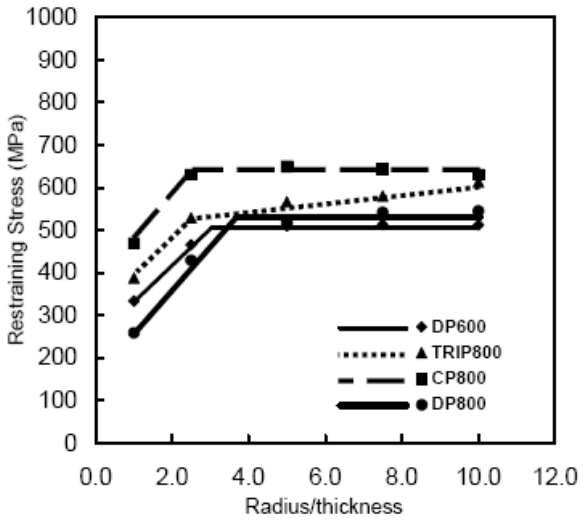

Figure 2.12. Result plot using modified Duncan Shabel tester [66].

Stretch forming tests are also used to investigate shear fractures [67-71]. Sriram et al. [67] conducted stretch forming tests for various conventional steels and AHSS. The test consists of a cylindrical punch with a specified radius which thrusts into a sheet fixed between lock beads. The punch radius is systematically changed to obtain various fracture modes in the tested sheets. Generally, a transition from sidewall failure to failure at the punch radius is observed with decreasing die radius. R/t can be used to measure the formability. It was found that as the strength level increased, formability decreased, as shown by the increasing critical R/t value (Figure 2.13). This finding is consistent with the results of other studies using BUT tests. These experimental studies indicate that high strength steels are more susceptible to shear failures. Micro-structural variations also appear to affect formability as well. The results from [64, 66] suggest that lower hardness ratios of micro-structural constituents and improved micro-structural homogeneity are beneficial for reducing shear fracture.

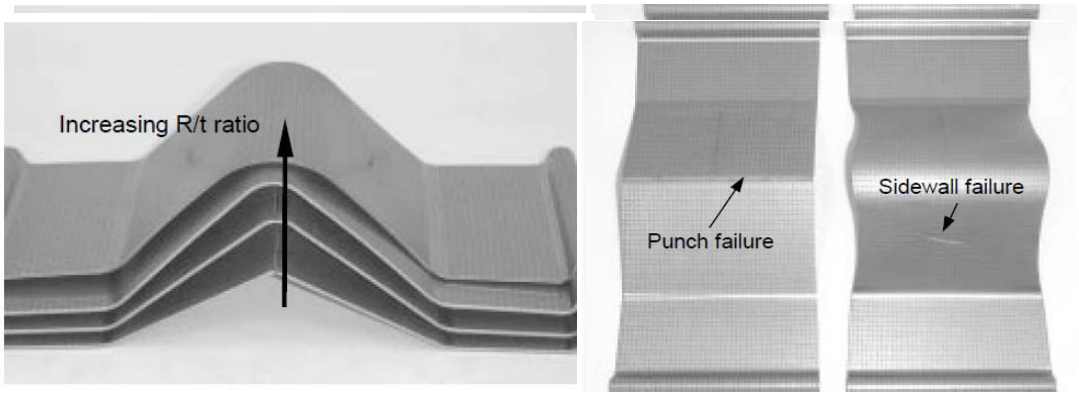

(a) (b)

Figure 2.13. Experimental stretch forming work performed by Sriram et al. on various high strength grades (a) at a range of radii (b) resulting in two types of fracture [67].

2.3.2. Modeling Work

Empirical Modeling

Several empirical models have been proposed for predicting failure at die radii [67, 72, 73] by processing and fitting the experimental data. Sriram et al.[67] utilized a strain ratio termed the stretch bendability index: the actual true major strain to failure over the predicted true major strain to failure, according to the FLC. This index was plotted as a function of R/t to compare with the tested data. Using the same data, Levy and Van Tyne [73] used a similar ratio translated into stress space to develop empirical relationships which could be used to predict fracture in the regions of die radii. Empirical equations were generated for each type of steel which predicted a linear function of stress ratio with R/t and promising correlations were observed. Huang *et al.* [69] proposed a general, empirically based failure criteria for all materials which utilized the FLCo term as a limiting thinning strain for different R/t ranges, but little experimental evidence was

provided for verification. Shih et al. [63] developed empirical criteria by fitting the tested data for various AHSS.

Besides using the test based empirical models, some studies tried FEA with modification of the FLC to predict shear fractures. The FLC is generated based on the instability theory and is suitable for forming failures with significant necking and thinning. Several researchers [75-76] have modified it to estimate failure limits in stretch bending processes. Wu et al. [77] proposed to use FLC by introducing a modified index for predicting shear fracture. Kim et al. [65] have considered temperature and strain rate in a constitutive model. In this model, a thermo-mechanical model is used to predict actual material behavior. The results were more accurate than the isothermal condition in comparison with the data obtained in BUT tests. Stoughton and his co-workers have identified differences in the onset of necking with consideration of high normal stresses through the thickness [75, 76]. These studies have illustrated that the through-thickness stress and strain gradients are important, and cannot be ignored in predicting stretch bending limits. The above methods modified the instability based FLC and improved the prediction accuracy. However, the predictability is case dependent.

Damage Model

Since the instability theory has limitations in shear fracture prediction other researchers investigated the problem using damage accumulation models. There are many damage models used in prediction of conventional steels. For example models proposed by Cockcroft and Latham [78], Rice and Tracey [79] and Gurson [80] are

commonly accepted. These models assume that failure will occur when the amount of plastic deformation accumulates to a critical level. The Cockcroft and Latham model expresses the critical damage parameter D as:

$$\int_0^{\bar{\varepsilon}_f} \frac{\sigma^*}{\bar{\sigma}} d\bar{\varepsilon} = D \qquad (2\text{-}1)$$

where, σ^* is the maximum principal tensile stress and $\bar{\sigma}$ and $\bar{\varepsilon}$ are the effective stress and strain respectively. Other investigations found that hydrostatic stress has a significant effect on fracture and must be considered in the damage model. Usually the hydrostatic stress σ_m is normalized (divided by equivalent stress $\bar{\sigma}$) and expressed as triaxiality. The damage parameter of Rice and Tracey is expressed as:

$$\int_0^{\varepsilon} \frac{\sigma_m}{\bar{\sigma}} d\bar{\varepsilon} = D \qquad (2\text{-}2)$$

Kim et al. [81] used the Cockcroft and Latham model to simulate shear fracture for draw bend tests. The critical damage value (CDV) in the model was calibrated from simulation of a tensile test. Simulation results showed good agreement with experiments in terms of fracture locations. The prediction was improved compared to the simulation without a damage model. However, it underestimated the displacement of the front grip at fracture compared to the experimental displacement value. It was suggested that the model could be improved by considering thermal effect [65]. They also demonstrated the feasibility to simulate shear fracture with the micro-void based Gurson-Tvergaard-Needleman model [80]. The fracture locations were predicted correctly. The above models are based on the fracture mechanism of void initiation, growth and coalescence which develops from

ductile fracture of conventional steel bulk forming. When applied to AHSS sheet forming, over-prediction of local deformation (higher thinning) was observed.

A study by Bao and Wierzbicki [82] concluded that none of the investigated ductile fracture criteria provided accurate representation of failures in the full range of stress states. An independent shear fracture study by Bai and Wierzbicki modified the Mohr-Coulomb (MMC) ductile fracture criteria [83]. Fracture occurs when the maximum combination of shear and normal stresses reaches a critical value. The fracture limit curve is generated by a variety of tests which cover the full range of stress states. The MMC model in this work appeared to show promising results with selected fracture analyses [62, 84]. Dunand and Mohr [85] compared the fracture prediction of the shear-modified Gurson model by Nielsen-Tvergaard [86] and the phenomenological MMC fracture criterion in various stress states. The MMC model can predict the onset of fracture with great accuracy while the Nielsen-Tvergaard model is less accurate.

2.3.3. Summary of Shear Fracture Review

Several laboratory tests and models have attempted to predict shear fracture. They were shown to be useful for particular case predictions, but very few validations exist for general cases. Various instability and damage models were tested for shear fracture predictions. Most models predicted higher local deformation because these models were developed for lower strength conventional steels. The MMC model considers a wide range of stress states including normal and shear stresses. It has great potential to provide satisfactory results for AHSS shear fracture analysis.

2.4. AHSS Edge Cracking

2.4.1. Introduction

Edge stretching, which includes stretch flanging and hole expansion, is one of the major deformation modes in metal forming processes. During the forming of conventional steels, the edge failure can be predicted using FLC with the consideration of the safety margin. However, this failure prediction cannot be applied to AHSS edge stretch in many cases because the edge failure strain is far below that predicted by FLC. Thus, edge cracking has become a serious manufacturing issue in stamping processes of AHSS. Figure 2.14 shows an automotive part made with DP600 steel. The overall formability was predicted as acceptable using the conventional FLC. However, severe edge cracks occurred in the stretch flanging region of the stamped part. One of the reasons for the failure to predict the edge cracking behavior is that the damage in the sheared blank deteriorates the forming limit at the edges and this factor is not considered in the forming prediction. Due to the high strength and the presence of hard phases in the microstructure of AHSS, it can be difficult to get a good edge from regular die punching/shearing compared to conventional high strength steels. Therefore, AHSS can be more prone to edge cracking, leading to additional challenges in the development of failure criteria for AHSS edge cracking [3, 87].

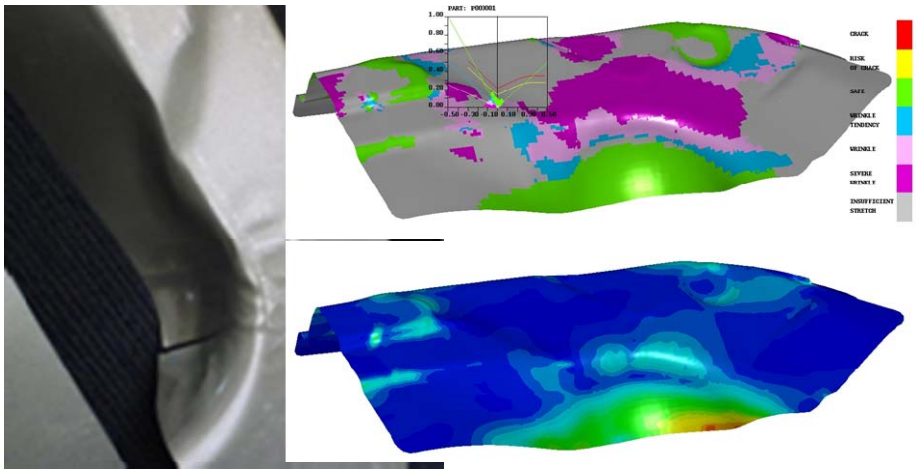

Figure 2.14. FEA failed to predict edge cracks of a DP600 component, (a) Actual stamping with edge cracks (b) FEA predicted strains in safe zone.

For simplification in the later text, shearing is used as a general term which includes piercing, blanking, trimming and cutting operations. To study sheared edge stretchability, hole expansion is a commonly used experiment. As shown in Figure 2.15, a standard hole expansion test is available from the ISO Standard [96]. The test uses a conical punch and an original hole diameter of 10 mm. The hole is punched with a clearance between the punch and die of approximately 10%. The hole expansion ratio (HER) is defined as

$$HER = \frac{D_f - D_0}{D_0} X 100 \qquad (2\text{-}3)$$

where D_0 is the original hole diameter and D_f is the hole diameter when the first through-thickness crack is observed.

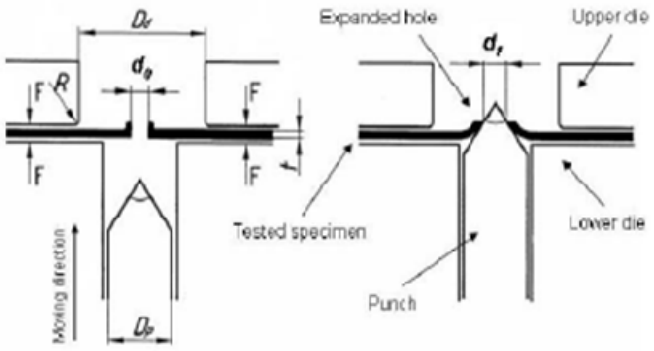

Figure 2.15. Standard hole expansion test from ISO Standard.

2.4.2. Experimental Studies

Effect of Process and Tooling

Sheared edge stretching processes and failure for conventional steels have been well studied and numerous publications have been dedicated to investigate various aspects of shearing processes and sheared edge stretchability [87-95]. An earlier review in metal piercing/hole-flanging was provided by Johnson et al. [88]. The study showed that the edge-stretch limit depends on both the shearing processes and material properties. The quality of a sheared edge is an important factor that affects the subsequent edge stretching or flanging behaviors. Severe deformation occurs in the shearing process. The deformation deteriorates the quality of a sheared edge and reduces the edge stretchability [87,89].

For conventional materials, sheared edges are composed of a regular shape characterized by four zones [97]; the roll over, burnish, fracture and burr zones. These are shown in Figure 2.16. A number of studies have shown that the edge quality can be

measured by the edge geometric features such as burr height. Keeler [98] showed that as the height of a sheared burr increases, the edge strain at failure decreases. Sriram and Chintamani [91,92] demonstrated the relationship among piercing clearance, rollover and burr height. The rollover and burr height increase with an increase of the die clearance, while the HER decreases for several conventional steels. Konieczny [89] showed that a similar relationship exists between the burr height and the die clearance for a high strength low alloy HSLA 50ksi steel. However, the burr height tends to saturate as the die clearance increases for the AHSS. It was found that a larger die clearance of approximately 20% yields the optimal HER for both the high strength low alloy and the advanced high strength steels.

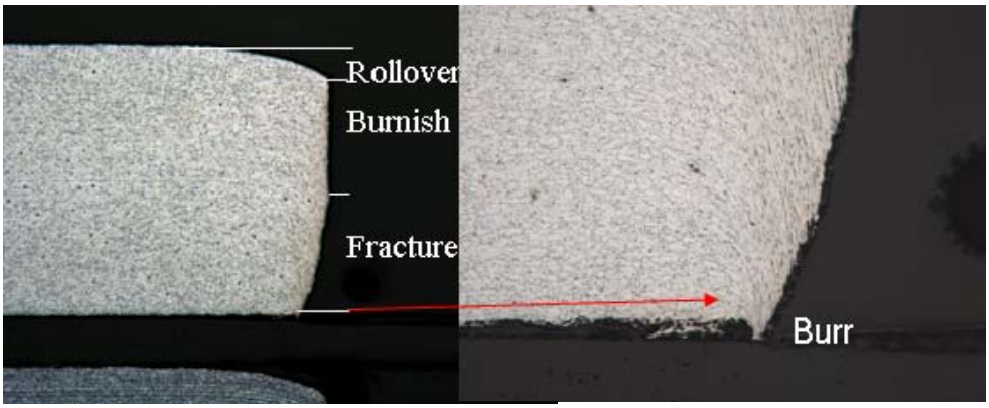

Figure 2.16. Four zones of sheared edges.

Karelova and Krempaszky [95] investigated sheared edges with different punching clearance values. Micro cracks were found in sheared edges for AHSS and the results showed that a better edge stretchability is directly associated with a better shear process. Other studies compared the HER under various hole shearing processes

including punched, laser cut and milled hole edges [89, 92]. The results showed that laser cut edges performed better than punched hole edges. The milled hole provided the highest HER because the milling operation produced little damage at the hole edge. Further evidence of the effect of edge condition can be found in a flat top punch hole expansion test with milled hole edge, crack initiated inward from hole edge [99]. The crack initiated location was in a plane-strain state and this failure mode can be predicted by FLC.

Some researchers studied the deformation and work hardening in the sheared edge and shear affected zone (SAZ), which is the deformed region behind the sheared edge. Levy and Van Tyne [100] processed the data of hole expansion and extrusion tests for 15 different grades of steel. They indicated that the strain path of SAZ must be considered when evaluating the failure strain in a sheared edge stretching. Another study measured the deformation that occurred at the shear edge and at the SAZ and found that the deformation along the hole edge is not uniform, which includes strain partitioning, strain localization and plastic instability [101].

Effect of Material and Metallurgy

Material property effects on stretchability have been investigated. Adamczyk et al. [93] found that high tensile strength was a detriment to expansion performance. Steels with higher elongation and higher planar anisotropy performed better. Comstock et al. [94] extended the work of Adamczyk et al. [93] and showed that the difference of HER in sheared-edge and milled-edge holes depended on the work-hardening exponent, n of the material. Higher work-hardening rates would result in higher strength material at the

sheared edge. This trend leads to a larger difference in the performance between sheared-edge and milled-edge because strength is inversely proportional to hole-expansion performance [102].

The failure mechanism related to the micro-structure of steel was also investigated. The study by Fang et al.[103] attributed the hole expansion (HE) performance directly to the microstructure or chemical composition of the material. Some recent studies were focused on the mechanism of the fracture initiation and propagation of the material at the hole edge, or the fracture toughness. The results suggested that fracture toughness was the dominant factor in the performance of stretching edges [104]. Hasegawa et al. [105] indicated that if micro-cracks propagated mostly along the phase interface in DP steels, edge stretchability would be poor, but if cracks propagated through ferrite and martensite phases, the stretchability would be higher. The difference in hardness of different phases is the dominant factor affecting the crack path and stretchability. Chiriac [99] found similar results by studying microstructures, micro-hardness and grain orientations. He also observed that the strain distribution along the hole edge was not uniform due to anisotropy. Similar findings were presented in other studies [106,107]. Dalloz et al. [90] performed experiments to evaluate the impact of shearing processes on the mechanical properties of DP steels. At the micro-structural level, observations revealed the decohesion of ferrite and martensite phases to be the original cause of damage.

Besides the hole expansion test, the uniaxial tension test is also used to investigate edge stretchability because it is easy to implement and can simulate the edge stretch

deformations where the strain state is in an uniaxial mode at the edge. Wang et. al. [108] tested six AHSS and proved that the sheared edge tension limit has a linear relationship with the HER. Chen et. al. [109] performed the tension test to study the edge pre-form effect on edge stretchability, and found that bending/unbending in pre-forming decreased the edge stretch limit for some AHSS.

Some industrial experiments were also performed on edge stretchability. Wu et. al. [110] performed experiments on large parts made of three DP steels with piercing and flanging of round-hole and multi-shaped holes. They characterized the shear-affected zone by measuring the shear angle and obtained the strain distribution. They also applied a replica method to obtain the geometrical information on the sheared edges including the heights of all four sheared edge zones, and found that the four zones are not regular for AHSS. Zhou et al. [111] tested the thinning distribution in full scale automotive parts. They showed that the thinning strain limit was suitable for evaluating failure of sheared edge stretching of automotive body panels with interior cutouts.

2.4.3. Simulation Studies

Empirical Model and Modified FLC

The above review focuses on the experimental activity, however, most studies involve analysis and modeling. The modeling work can be divided into three main types: empirical, analyses with modification FLC as the failure criteria, and ductile fracture FEA.

Wang and Wenner [112] provided a closed-form solution to calculate the maximum tension strain on the stretch flange edge. Wang et al. [113] presented an analytical model for both stretch and shrink flanges. Though these models can be effectively used to analyze simpler flanging processes, they are not ideal for more complicated industrial components.

FEA is used for more complicated analysis. Several studies used FLC as a failure criteria, but modified it using hole expansion test data [100,114,115]. McEwan et al. [114] proposed to combine HER and FLC for general forming limit to predict forming failure. Levy et al. [100] indicated that by considering the strain path in SAZ, the FLC could be modified to determine the hole expansion failure. Some studies proposed to use tested HER as the failure limit in simulation to predict the edge failure. It needs only to compare the HER with the edge major strain to be analyzed because the edge is in uniaxial deformation mode [87,116]. Shi and Chen [3] validated this approach in both laboratory and full scale parts under edge stretch and showed favorable results. Zeng et al. [115] used a simplified 2D approach to simulate flanging process in complex geometries.

Damage Approach for Ductile Fracture

Many simulation studies can be found based on the theory of ductile fracture, especially for shearing process simulation. Various material models and failure criteria have been developed to analyze void initiation, growth and coalescence [117-126]. A short overview of the ductile fracture criteria is given in [117]. Growth and coalescence

of voids are driven by plastic deformation. Consequently, in the modeling of fracture initiation, the deformation history is required. Goijaerts et al. [118] described the general form as an integral over equivalent plastic strain ($\bar{\varepsilon}_p$) up to fracture of a certain function of the actual stress state reaching a critical value C.

$$\int f(\sigma) d\bar{\varepsilon}_p = C \qquad (2\text{-}4)$$

$f(\sigma)$ is a function of the stress tensor. The formulations are different for different fracture criteria, but the parameters that influence ductile fracture are included such as plastic strain and triaxiality. Triaxiality describes the effect of hydrostatic stress on void initiation and void growth. If the integral on the left-hand side reaches the critical value C during the process, ductile fracture initiates. Element deletion techniques with very fine meshing were used to capture the edge shape after shearing separation. The critical value is generally regarded as a material constant and can be calibrated by experiments. Goijaerts et al. [119] compared the calibrated values when using experiments of shearing and tension test. Very good agreement was achieved using a shearing test for calibration. When using a tension test for calibration, the error was less than 6%, which is acceptable in industrial applications.

Many others investigated the shearing processes using FEA with ductile fracture mechanics which included the effects of tooling geometry, clearances, sheared edge geometries, material properties and process parameters such as shear force and friction. Wiedenmann et al. [125] simulated shearing processes and evaluated eight different fracture criteria. The critical value was calibrated using the experiment in Ref. [89]. The

eight fracture criteria are listed in Table 2.1. It was found that adapted Rice and Tracy's [79] criterion was the best for modeling of the shearing processes.

Table 2.1. Various ductile fracture criteria

Fracture criterion	Formulation	Nomenclature
Normalized Cockroft & Latham	$\int_0^{\bar{\varepsilon}} \frac{\sigma^*}{\bar{\sigma}} d\bar{\varepsilon}=C$	$\bar{\sigma}$: effective stress, $\bar{\varepsilon}$: effective strain, C: calculated damage value, σ^*: maximum principal stress, σ_m: hydrostatic stress (mean stress), n: strain hardening coefficient, σ_a: principal stress in the direction of the greatest void deformation, σ_b: principal stress normal to σ_a, α_0: Oyane constant, α: Rice & Tracey constant.
McClintock	$\int_0^{\bar{\varepsilon}} \left(\frac{\sqrt{3}}{2(1-n)} \sinh\left(\frac{\sqrt{3(1-n)}}{2} \frac{\sigma_3+\sigma_b}{\bar{\sigma}} \right) + \frac{3}{4} \frac{\sigma_3-\sigma_b}{\sigma} \right) d\bar{\varepsilon}=C$	
Oyane et al.	$\int_0^{\bar{\varepsilon}} \left(1+\frac{\sigma_m}{\alpha_0 \bar{\sigma}}\right) d\bar{\varepsilon}=C$	
Adapted Oyane [11]	$\int_0^{\bar{\varepsilon}} \left(1+\frac{\sigma_m}{3.9\bar{\sigma}}\right) d\bar{\varepsilon}=C$	
Ayada	$\int_0^{\bar{\varepsilon}} \frac{\sigma_m}{\bar{\sigma}} d\bar{\varepsilon}=C$	
Rice & Tracey	$\int_0^{\bar{\varepsilon}} \exp\left(\frac{\alpha\sigma_m}{\bar{\sigma}}\right) d\bar{\varepsilon}=C$	
Adapted Rice&Tracey [11]	$\int_0^{\bar{\varepsilon}} \exp\left(2.9\frac{\sigma_m}{\bar{\sigma}}\right) d\bar{\varepsilon}=C$	
Goijaerts [11]	$\int_0^{\bar{\varepsilon}} \left(1+3.9\frac{\sigma_m}{\bar{\sigma}}\right) \varepsilon^{0.63} d\bar{\varepsilon}=C$	

2.4.4. Fracture Mechanism and Micro-mechanics model

Much research has been conducted on AHSS fracture mechanisms at the microstructural level because of the multi-phase nature of AHSS [126-128]. However few publications can be found for simulations of AHSS shearing fractures including the effects of steel micro-structure and phases. AHSS fractures generally exhibit ductile dimpled structures by micro-void coalescence. Void initiation mechanisms include ferrite-martensite boundary de-cohesion, martensite fracture, martensite plasticity, and martensite packet separation. The dominant mechanism depends on the martensite morphology, distribution and hardness.

Cleavage in ferrite was also reported by Kim and Thomas [129], in a study of quasi-static tensile properties of relatively coarse microstructure dual phase steel. The cleavage was attributed to a high localized stress concentration due to constraining effects from surrounding martensite [129]. Similar results were reported by Kim and Lee [130]. In this study, the refined microstructure, both equiaxed and fibrous, exhibited micro-void coalescence. The refined microstructures showed voids which initiated from ferrite - martensite interfaces, and propagated into ferrite regions. Crack propagation into martensite was found to occur last.

Since the micro-structure plays an important role in AHSS fracture, several studies analyzed AHSS fracture using micro-mechanical based finite element models [131-136]. The micro-structure was modeled using the representative volume element (RVE) model. The FE meshes are created either from scanning electron microscope images [134,136] or statistically generated microstructures [131-133,135]. Material properties were assigned to different phases. AHSS deformation at the microstructural level can be analyzed by combining the RVE model with continuum mechanics. Several studies used ductile fracture criteria to assess the formability [131-134], while others [135,136] predicted the failure as the natural outcome of the deformation between the hard martensite phases and the soft ferrite phase. Though there are no sufficient experiments to verify the simulation results, the micro-mechanics approach can be used to analyze the AHSS deformation and failure considering the microstructure effects such as phase strengths, inhomogeneity, and distribution. This provides a great potential for numerical assistance in material grade designs.

2.4.5. Summary of Edge Cracking Review

Edge shearing and stretchability can be studied using hole expansion tests. The sheared edge has a regular shape of four zones. For lower strength steels, the edge quality can be measured with the edge geometry. Various modeling methods can be used to predict edge stretch including empirical, FEA with modified failure criteria and ductile fracture analysis. Most of these methods are well established for conventional steels and soft metals but may not be applied to AHSS. For AHSS steels, microstructure plays an important role in the sheared edge quality due to the high volume fractions of hard phases. The difference in phase strengths is the dominant factor affecting the crack path and edge stretchability. The "four zone" edge feature is not consistently observed on the sheared edges of the AHSS. This suggests that measuring the geometric features of an edge is not sufficient to determine the AHSS edge quality and further investigations are necessary to characterize the AHSS sheared edge. Severe deformation occurs at sheared edges and deteriorates the edge formability of AHSS. It is necessary to incorporate the deformation history of a sheared edge into the subsequent forming simulations. Material models and failure criteria need to be validated and their parameters need to be experimentally determined.

2.5. Simplified Methods

The most favoured numerical technique for metal forming simulation is the finite element method. It has the capability of handling very general geometries, different deformation models and material behaviours. One disadvantage of the finite element method

is that solutions can be extensively time consuming. In addition, the predictive capability is affected by the input conditions, such as friction, contact between the tools and the blank and the way the blank is constrained. These variables are not known in many cases. For some specific analyses, simplified approaches may be more advantageous [137]. One example is the benchmark 1 of Numisheet2011, which is for analysis of earing evolution during the drawing and ironing processes. 10 participants contributed predictions of this benchmark. Hans Mulder [138] used an analytical method and outperformed the other nine participants in both computation time and accuracy. The other nine solutions used FEA [139]. Some of the simplified methods are less rigorous than FEM's and do not attempt to model the entire deformation process. The goal is to concentrate on specific regions within the component, with the objective to provide insight into the forming process. The flange region during the deep drawing of prismatic cups has been analysed using several different techniques such as finite difference methods [140,141], upper bound solutions [142] and slip line field analysis [143,144]. A review of the various modelling methods is provided in a paper by Sowerby [145].

A study of the deformation within the flange can assist with the development of optimum blank shapes [146,147]. Jimma [148] and Gloeckl and Lange [149] utilized this technique to produce various blank shapes. Computer programs have been developed to produce optimal blank designs for a given process at high computational speeds [146,149]. The method of slip line field analysis is under the condition of plane strain deformation, which is suitable for some sheet forming processes, but plane stress condition is suitable for most of the sheet forming processes. Therefore, plane stress method is more useful for sheet forming and plane stress characteristics (PSC) have been developed for this type of analysis. The formulations and various applications can be found in the books of Hill and Szczepinski [144, 150]. Vogel and Lee [151] used the PSC method to analyse the deep drawing of

circular, square and rectangular cups. Chen and Sowerby [152] used PSC to develop optimal blank geometries to analyse the flange deformations. Anisotropy is an important property of sheet steel affecting forming results, and thus should be incorporated in analyses. Chen and Sowerby [152,153] developed the PSC formulation of planar anisotropy by including the r value, and established that the characteristics of stress and velocity coincided. An application was also used to show the earing development for the entire process of circular cup drawing. These applications demonstrated the efficiency of using simplified methods to analyse the problems in sheet metal forming.

2.6. Summary of AHSS Forming Review

Advantages of AHSS include high strength and good general formability. It is for these reasons that AHSS have been adapted for automotive applications increasingly. However, forming issues such as springback, shear fracture and edge cracking are barriers to further applications. Many of these problems cannot be predicted using conventional simulation methods. The design and development of tools and processes still involves significant trial and error processes. Therefore new simulation technology needs to be developed for AHSS forming. The technologies include optimisation of simulation parameters, development of material models, establishment of local formability criteria and the integration of these approaches to forming simulations and validations. These simulation technologies will be presented in the following chapters:

Chapter 3. AHSS springback Simulation

Chapter 4. Simulation for AHSS shear fracture

Chapter 5. Simulation for AHSS edge shear and edge cracking

Chapter 6. Simplified simulation method for AHSS forming

CHAPTER 3. SPRINGBACK SIMULATION

3.1 INTRODUCTION

Springback introduces dimensional deviation in a finished part which will cause problems in the subsequent manufacturing processes. AHSS parts usually undergo more springback than conventional high strength and mild steels. Figure 3.1 is an example showing that the degree of springback increases as the material strength increases [155]. A hat channel draw bending is tested with steel tensile strength (TS) from 300 to 1020 MPa. Three values of the die shoulder radius (rd) were considered. The channel opening "W" is used as an index to measure the level of springback. It is seen that the "W" has a strong correlation with TS.

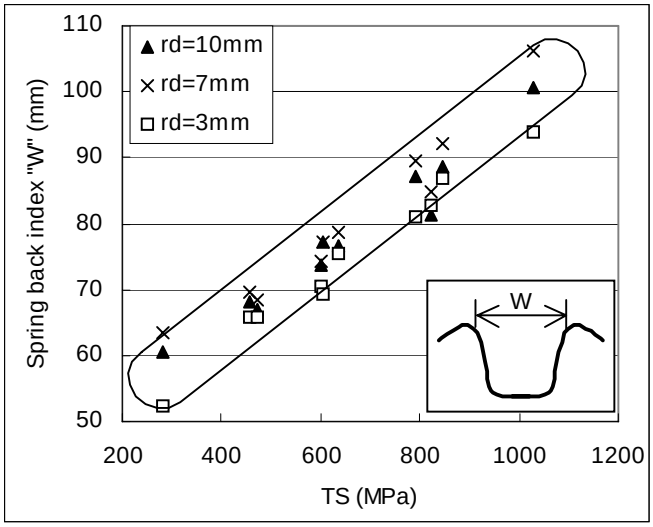

Figure 3.1. Relationship between spring back index "W" and TS.

For better understanding and controlling of springback, various laboratory tests and full scale part tests have been carried out. Some process control techniques have been successfully developed to control and minimize springback. Figure 3.2 shows one technique of increasing the sidewall stiffness. By adding vertical beads on the sidewall, stiffness is much higher and springback is significantly lower on the left sidewall. Figure 3.3 shows another example using a floating draw bead to reduce the springback. The drawbead provides higher sidewall stretch in the last forming step and reduces springback. It is observed from various tests that increasing of sidewall strain in the last forming stage creates more uniform forming stress distribution through the sheet thickness and lower tendency of springback. These experiments and trials provided very useful information for springback control. However, it is very difficult to analyze the springback accurately because the sidewall stresses are very difficult to measure. Accurate computer simulation technology will be very beneficial for springback control.

Figure 3.2. Vertical bead reduces springback

Figure 3.3. Floating bead controls springback

Accurate prediction of springback is a challenging task though forming simulations have been very successful to predict strain distributions. Springback simulation is a complicated process, since it involves large and non-uniform deformation in different forming stages and follows with elastic unloading to obtain a correct residual stress distribution. Figure 3.4 shows a fender loadbeam springback prediction using the traditional simulation method. A large deviation is seen in comparison with the experimental result. The simulation under-predicts springback in most of the cases. Two FEA solvers are usually used for metal forming simulations, static implicit and dynamic explicit. Metal forming is a static process and static implicit method should be used. However, divergence problems often occur when analyzing large model with a large number of elements. To avoid this problem, dynamic explicit method is usually used for forming simulations, which provides accurate strain results but often introduces dynamic effect and causes errors in stress computations. The other error sources in AHSS springback simulation are identified from inadequate material model and contact approach.

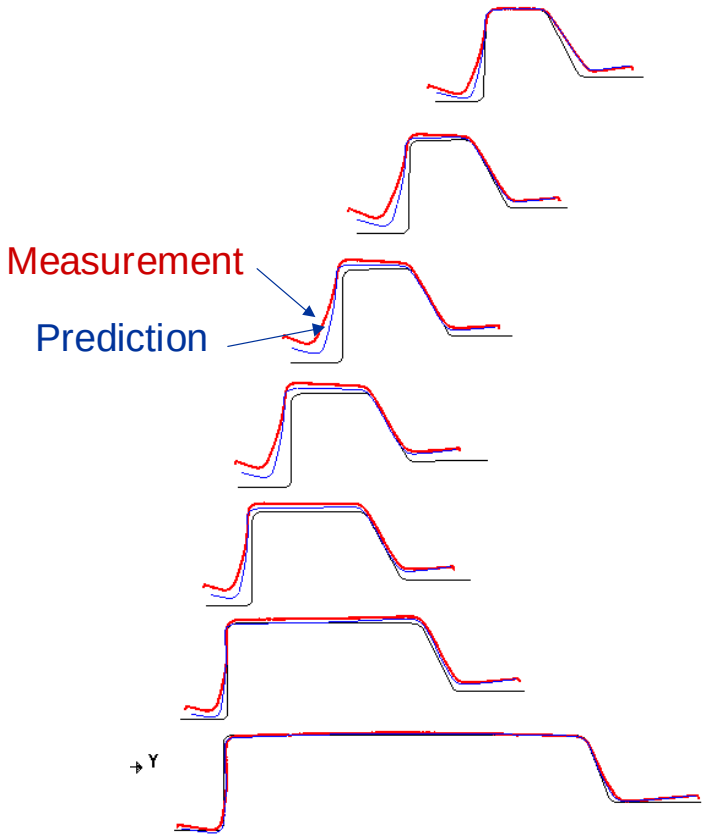

Figure 3.4. Simulation predicts lower springback than measured data.

In this chapter, detailed studies are carried out to investigate the most important aspects of numerical simulations that affect springback predictions. Systematic parametric studies are conducted to identify the key simulation variables and their optimal values for minimizing prediction errors. Smooth contact and selective mass scaling are used in forming simulations which leads to great improvement in robustness and accuracy of stress calculations [40]. A nonlinear isotropic/kinematic hardening material model is applied for simulating AHSS deformation. Several case studies using laboratory and industrial parts are conducted. Experimental data are used for correlations

of simulation results. Springback prediction is significantly improved with the use of these latest simulation technologies.

3.2. MATERIALS

Eight different automotive sheet metals were selected for the study, with one DQSK mild steel, one bake hardenable (BH) medium strength steel, a conventional high strength (HSS), a high-strength low-alloy (HSLA) steel, three dual-phase (DP600, DP780, DP980) steels, one transformation induced plasticity (TRIP) steel and one aluminium alloy (6022-T4). The tensile properties of these materials were tested along three orientations, namely the rolling direction (0^0), the diagonal direction (45^0), and the transverse direction (90^0). They are listed in Table 3.1. The stress – plastic strain curves in the rolling direction are plotted in Figure 3.5. The curves are extended after uniform elongation with the power law for simulation purpose. It can be seen that DP and TRIP steels have much higher tensile strength. This capability makes them better in crashworthiness and structural performance, but also causes higher springback after forming.

Table 3.1. Mechanical Properties

Steel Grades	Yield (MPa)	UTS (MPa)	TE %	n value	R 0	R 45	R 90	R bar
DQSK	153	307	45.6	0.25	1.734	1.515	2.085	1.712
BH210	248	370	37.3	0.195	1.48	1.349	2.173	1.588
HSS	277	397	32.0	0.196	1.66			1.66
HSLA340	411	496	28.0	0.146	0.907	1.064	0.68	0.929
DP600	403	654	23.0	0.159	0.843	0.912	1.018	0.921
DP780	462	831	18.0	0.140	0.819	0.911	0.925	0.976
DP980	573	1003	15.1	0.116	0.77	0.88	0.86	0.85

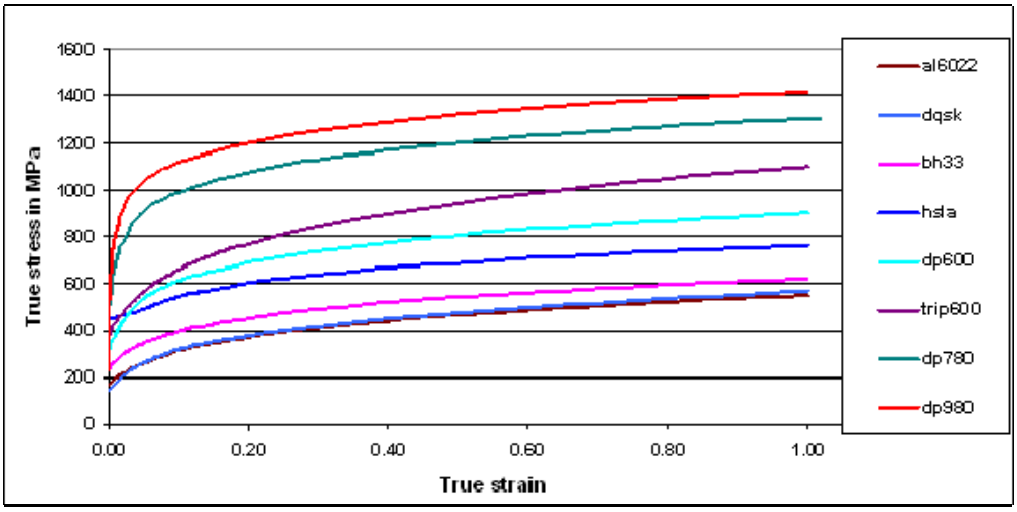

Figure 3.5. Stress-strain curves for tested materials

3.3. SIMULATION PARAMETER STUDY

When using a dynamic explicit method for forming simulations the default parameters are chosen for crash simulations. This does not provide sufficient accurate stress calculations for springback predictions. Although many previous parameter studies were conducted and some successful cases were obtained for springback predictions of conventional steels, further parameter sensitivity studies are necessary for AHSS due to their different behaviors of higher springback and twist. From the literature review and previous simulation experience [13, 17, 30, 39, 40], a general guideline can be used for setting up the initial values for sensitivity study and it is described as follows:

Element Type: A fully integrated shell element with four integration points in the plane is more accurate to describe the stress distribution.

Element Size: The element size is important for accurate springback predictions. Mesh that is too coarse may result in an under-predicted springback, or in some occasions, it may even result in springback prediction in the wrong direction. If the element size is too small, it will not only increase computational time but also introduce higher truncation error. Element size that is too small does not necessarily increase the prediction accuracy. It is found that about 5~6 elements are needed to cover a 90º bending region.

Adaptive Mesh Level: To reduce computation cost, coarse meshes are often used in the beginning of a forming simulation and the mesh adaptivity is used to refine the elements in the regions with curvatures. The adaptive level is related to the initial element size and the curvature of the geometry. Proper adaptive mesh level ensures that the final elements satisfy the above-mentioned element size requirement.

Number of Integration Points (NIP) through Shell Thickness: Although some other studies showed that more than 30 points were necessary for shell element [37], in most cases, the stable range was found when NIP was greater than seven, In the current study, less than seven integration points were used for large industrial parts and nine integration points for small laboratory models.

3.3.1 Validation Study using Slit-Ring Test

Experiment Set up

To verify the parameter selection, a laboratory test sample "Deep Draw Cup and Slit Ring Test" is used [16]. The experiments were conducted consisting of four steps:

(a) Deep draw a cylindrical cup from a circular blank with a constant blank holder force; (b) Cut a circular ring from the mid-section of the drawn cup; (c) Slit the ring along certain direction to release residual stresses introduced from drawing operation, and (d) Measure the opening of the ring (springback). The experimental setup and tool dimensions for the cup drawing are shown in Figure 3.6. The blank holder force used was 88.9 KN and the maximum punch travel was set at 56 mm. An oil lubricant is applied to both sides of blanks, and dry film is also applied to the die side of blank to further reduce friction. The illustration of a drawn cup and slit-ring is shown in Figure 3.7. The final cup diameter is 110 mm with 56 mm height, drawn from a circular blank of 195 mm in diameter. A circular ring of 15 mm width is cut from the formed cup as shown in Figure 3.7 (a). Then the ring is slit for springback measurements as shown in Figure 3.7 (b).

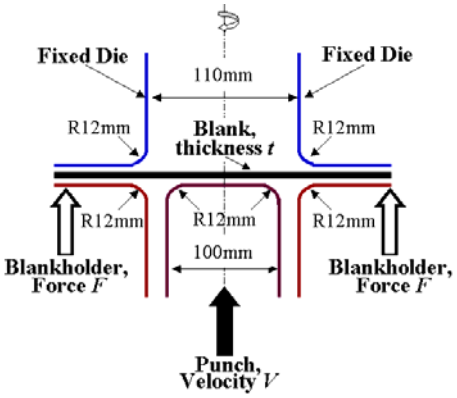

Figure 3.6. Experimental Setup for Cup Drawing.

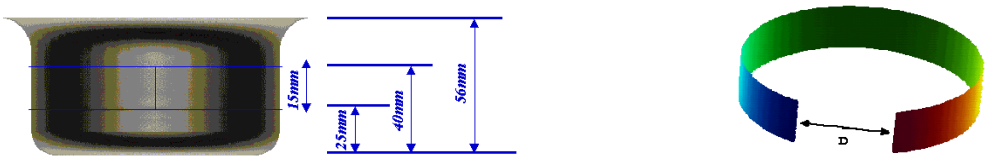

(a) (b)

Figure 3.7. Drawn cup and ring cutting.

Simulation Set up

The FEA simulations consisted of cup drawing, ring trimming and springback simulation after the ring slitting [17]. The FEA package of LS-DYNA was used for the simulations. A dynamic explicit method was used for cup drawing and a static implicit one was used for springback simulations.

Figure 3.8 depicts the FEA model during cup drawing. Due to the symmetry of the part, the half model was used in this study and the full model was used only for verification purposes. The slit ring model and its rigid body motion constraints for springback simulations are illustrated in Figure 3.9. A set of baseline parameters was selected and is summarized as follows:

1. Punch speed: 2500 mm/sec
2. Element size: 1.25 mm without adaptive mesh
3. Material model: Transversely anisotropic elastic-plastic model
4. Element: Fully integrated shell element
5. Integration points through thickness: 7
6. Friction Blank – Blank holder, Punch: 0.10
7. Friction Blank - die: 0.05
8. Blank holder Pressure: 88.9 kN
9. Contact penalty factor: 0.1
10. Hold time after the bottom of stroke: 0.0

In the parametric sensitivity study, six variables were selected: mesh size/adaptive level, model size (half and full), number of integration points through thickness, contact penalty factor, simulation speed and hold time (settle down time). In each case study,

only one parameter was changed while the others remained the same as the baseline values.

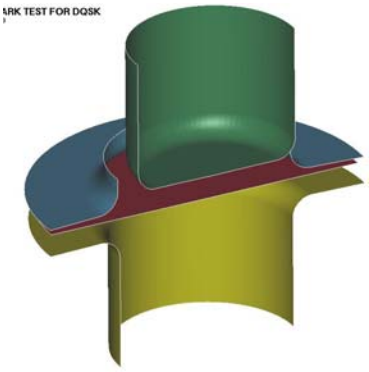

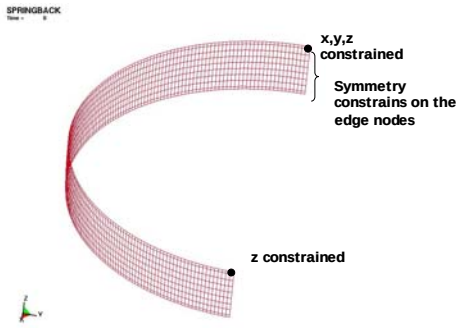

Figure 3.8. Deep Draw Cup Forming Model. Figure 3.9. Slit Ring Springback model.

Results and Comparisons

Forming

The drawn cups from the experiment are shown in Figure 3.10 for all six materials. The peripheries of the cup flanges were also measured and are presented in Figure 3.11. These data are used to check the accuracy of forming simulations. Circular cup drawing is a well-studied case in metal forming analysis. The simulation result can be verified by strain distribution and final blank diameter comparisons. Figure 3.12 depicts the strain distribution pattern (signature) of DQSK steel, which shows a typical shape of circular cup drawing. All other materials have a similar strain signature, which indicates that the simulation results are valid. The comparison of final blank diameters also indicates a good correlation as shown in Figure 3.13. The maximum deviation between simulations and tests is less than 5%.

Figure 3.10. Deep Drawn Cups

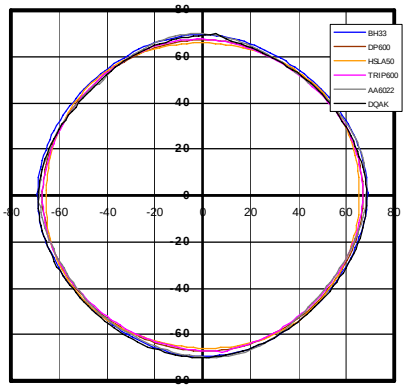

Figure 3.11. Measured Peripheries of Cup Flanges

Parameter Sensitivity Study

The sensitivity study was performed on forming simulation and the variables have less effect on forming results (measured by strains). However, they affect more significantly on the consequent results of springback simulations. The simulation matrix of the six parameters selected is listed in Table 3.2. The DQSK material is selected for this sensitivity study.

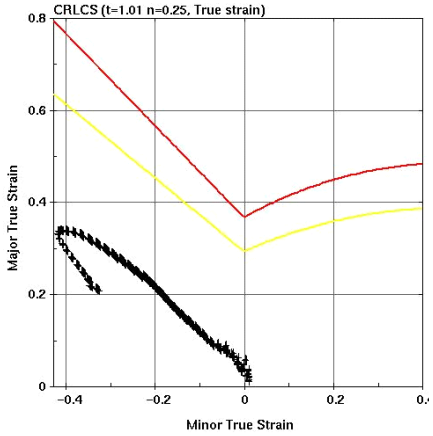

Figure 3.12. Strain signatures of the deep drawn cup.

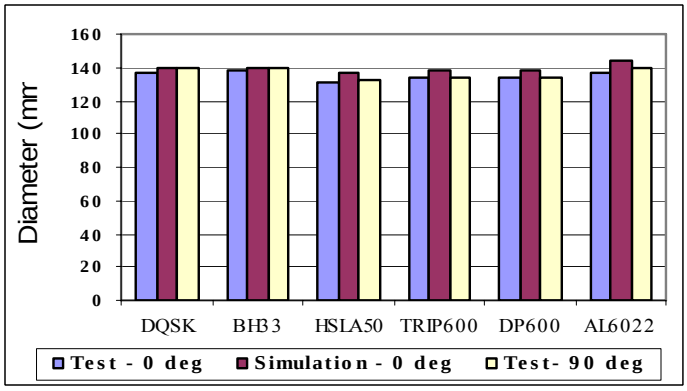

Figure 3.13. Comparison in Flange Diameters

Figure 3.14. depicts results of all the simulation cases based on the matrix in Table 3.2. The simulation predictions are also compared to the experimental results. Three horizontal lines are shown in the figure in which the center one is the average value from experiments, and the upper and lower ones are ±10% from the average experimental data. Looking at the simulation results only, the variation of results is within 10%, which indicates that the simulation results are reasonably stable within the variable ranges selected. When compared to the experimental results, the predicted springback results are higher, but the deviations for most cases are less than 10%, which is considered to be satisfactory for springback simulation.

Table 3.2. Simulation Parameter Sensitivity Study Matrix

	Mesh				**Model**		**Integration Points #**			**Contact**			**Acceleration**			**Settle Down Time**	
	Uniform	*Adaptive & Initial size*								*Penalty*		*Soft Contact*	*w/o Mass Accel.*		*Mass Scale -1.00E-06*		
	1.25mm	*5 mm 3 Level*	*10 mm 4 Level*	*20 mm 5 Level*	*Half*	*Full*	*5*	*7*	*9*	*0.1*	*0.01*		*2.5m/s*	*5m/s*	*2.5m/s*	*5ms*	*0*
1	X				X			X		X					X		X
2		X			X			X		X					X		X
3			X		X			X		X					X		X
4				X	X			X		X					X		X
5	X					X		X		X					X		X
6				X		X		X		X					X		X
7	X				X		X			X					X		X
8	X				X				X	X					X		X
9	X				X			X			X				X		X
10	X				X			X				X			X		X
11	X				X			X		X			X				X
12	X				X			X		X				X			X
13	X				X			X		X					X	X	

Some sensitivity trends can be seen from Figure 3.14. Reducing the number of integration points through the thickness increases the springback slightly. The predicted springback increases as the simulation speed decreases. However, the settle down time has little effect on the springback prediction results, which indicates that the dynamic

effect is insignificant for the simulation speed used. Contact penalty factors have minor effect on the results. It can be also seen that the simulated results are not affected when the initial element size is 2.5 mm or smaller. The simulation results are similar between the full model and the half model.

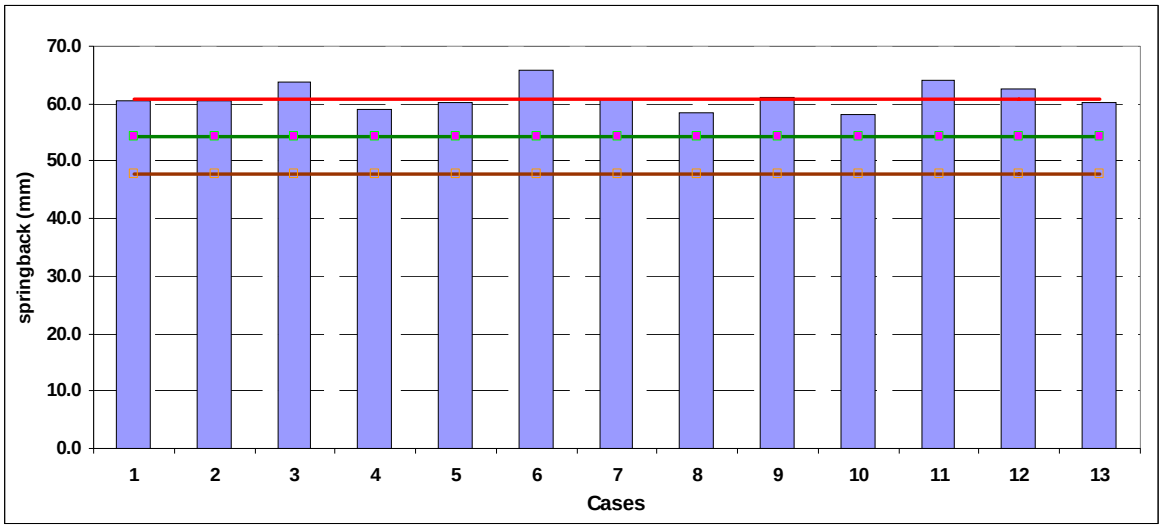

Figure 3.14. Springback Simulation Results from Parameters Set up Matrix

Springback Prediction

As shown in the parameter sensitivity study, the parameters listed in the base line set up resulted in a satisfactory result for DQSK steel. Therefore, these parameters were used in the simulation for all other five materials. The summary of simulation results along with experimental data is shown in Figure 3.15 for six materials listed in Table 3.1. Again, the three data points from the experimental measurements are given for all materials, i.e., the average value and 10% above and below the average value. It is shown from the Figure 3.15 that the simulation under-predicts springback for all

materials except for the DQSK which is about 10% over predicted. A result for BH33 is about 5% under-prediction and that for HSLA and DP600 are 10% under-predicted. For TRIP600, the prediction is about 12% lower than the mean experimental value. For AA6022, the prediction is 9.6% lower than the measured mean value. All AHSS under predict springback due to the isotropic hardening model used which does not adequately describe the Bauschinger effect of AHSS.

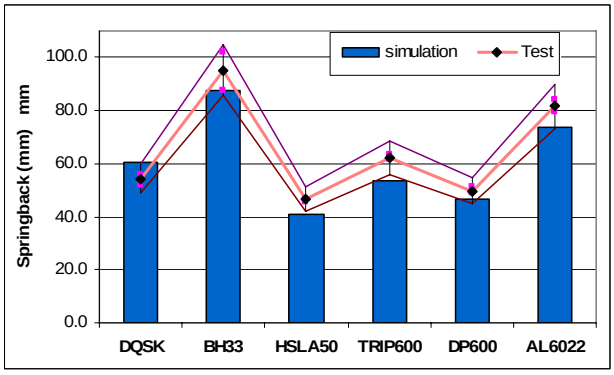

Figure 3.15. Predicted springback results vs. experimental data for six materials.

3.3.2. Mass Scaling Effect

When using a dynamic explicit code in forming simulations, the material density and the minimum element size determine the time step. A finer mesh reduces the time step and thus increases the computational time. Mass scaling is often used to artificially increase the material density which forces a larger time step. However, it generates an additional inertial force and induces errors in stress computations which have a significant effect on springback prediction robustness. The dynamic effect is not

significant in the slit-ring test example, but may not the case for other part geometry. To analyze the MS effect, the Numisheet 93 benchmark sample is used as shown in Figure 3.16.

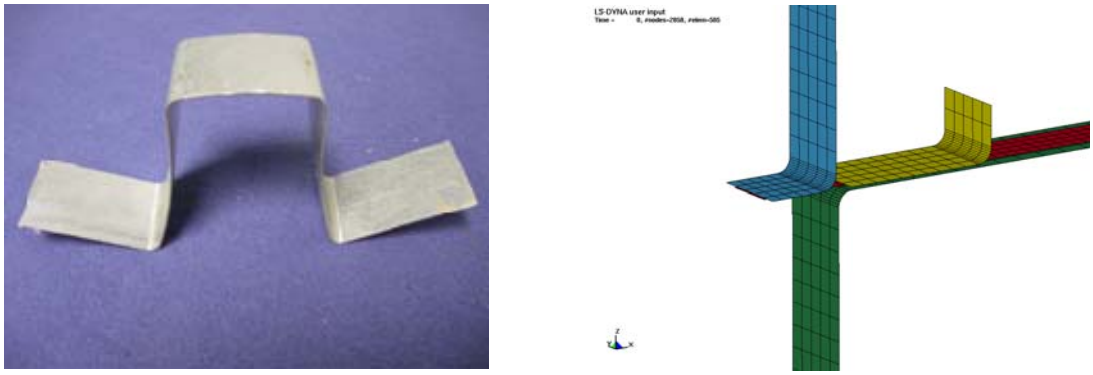

Figure 3.16. Numisheet '93 benchmark and FE model (half).

Figure 3.17 shows springback simulation results on the Numisheet 93 benchmark sample with the HSS material. To test the sensitivity of springback prediction accuracy with respect to different time steps, three MS factors is used, i.e. $4x10^{-6}$, $2x10^{-6}$ and $1x10^{-6}$ seconds. In the figure, sections of corresponding springback profiles are plotted to compare simulation results with experimental data. It is seen that the springback profiles are scattered. This means the simulation results are very sensitive to the MS. The springback results of all three cases are lower than the experimental data (under prediction). The flange opening angles are also measured and shown in Figure 3.17. To reduce the sensitivity to MS, the selective mass scaling (SMS) approach is used, which increases the material density by considering the neighboring element information. Using this new feature in simulations, the sensitivity of springback prediction to different

MS factors is significantly reduced. As shown in Figure 3.17, the two section profiles corresponding to MS factors of $2x10^{-6}$ and $1x10^{-6}$ are very close. The similar trend is observed in the flange opening angle, as shown in Figure 3.18. Therefore, the use of the SMS improved the prediction consistency as well as accuracy but still under-predicted the springback.

3.3.3. Effect of Contact Approach

The contact approach, used to treat sliding and impact along interfaces between the sheet metal and forming tool surfaces, is also an important factor affecting springback prediction, especially for a large model. Various contact algorithms can be used to describe interface surfaces. In the conventional contact approach, the interface condition is determined based on the triangle or quad element patches, rather than on the smooth surface. The non-smooth surface based method may introduce large errors in normal and node penetration calculations, and therefore cause severe slave node penetration. These errors introduce incorrect contact force calculations and then affect the stress results. As a consequence, springback prediction results are very sensitive to the contact parameter of the penalty scale factor (contact stiffness). Previous studies showed that reducing the penalty scale factor improved the prediction, but the sensitivity was still high and became more severe for AHSS. To solve this problem, a new contact approach, smooth contact (SC), has been implemented [40]. In this new approach, the contact elements are fitted by smooth B-spline surfaces instead of element patches. The smooth surface minimizes errors in contact surface normal calculation. During contact searching, a penetrating slave

node can be found in the early stage to prevent a large penetration error. As a result, the prediction results are not only less sensitive to the penalty scale factor but also more accurate. As shown in Figure 3.17, the springback prediction using smooth contact is greatly improved when compared to experimental data. The two predicted profiles which included smooth contact and SMS (SC SMS) fall within the lower and upper bounds of experimental data. Similar result for flange opening angle can be seen in Figure 3.18.

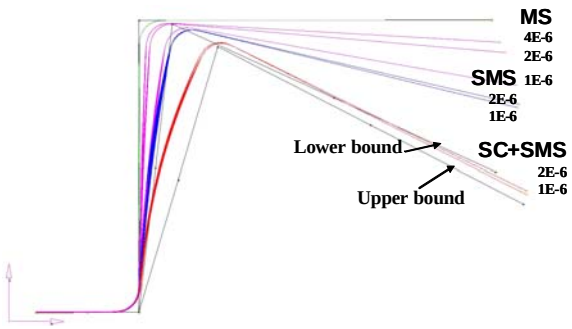

Figure 3.17. Effect of mass scaling and smooth contact on springback.

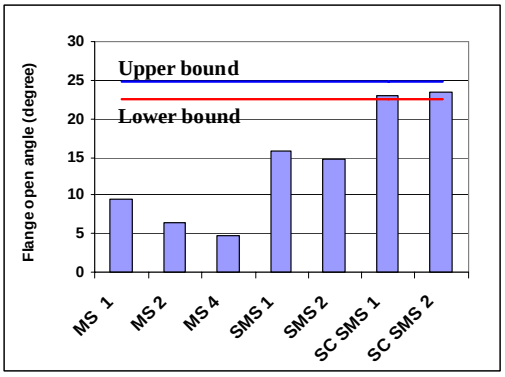

Figure 3.18. Effect of mass scaling and smooth contact on the flange opening.

3.4 Material model

The selection of material models is critical in simulations of forming and springback, especially for AHSS. In most stamping simulation applications, the isotropic hardening model coupled with an anisotropic yield criterion is usually used due to the simplicity. The constitutive parameters can be easily obtained from a uniaxial tension test. In the slit-ring cup springback study in the previous section, various yield criteria were evaluated including von-Mises, Hill's plane stress, and Hill's and Barlat's

anisotropic yield functions, and the corresponding predicted and measured flange diameters for BH210 steel are shown in Figure 3.19, The Lines M0, M45 and M90 are the experimental flange diameters of the drawn cup in 0, 45 and 90 degree, respectively. For each yield criterion, the first, second and third column represent the simulated cup flange diameters at 0, 45 and 90 degrees, respectively. We can see that the forming results correlate reasonably well with experimental data for most of the yield criteria except for the Barlat and Hill's 48 anisotropic models with r values in 0, 45 and 90 degree directions, which slightly over-predict the earrings. Figure 3.20 shows the springback result comparison. The two horizontal lines represent the experimental upper and lower bounds. We can see that the prediction trend in simulation results is not consistent and most of them under-predict the springback. A better material model is needed for springback predictions.

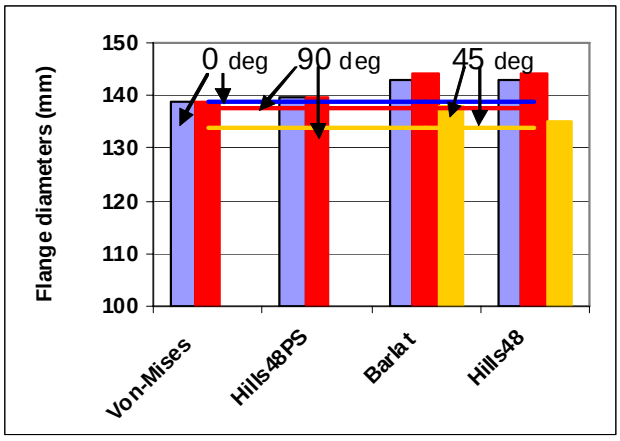

Figure 3.19. 0, 45 and 90 degree flange diameters for different material models.

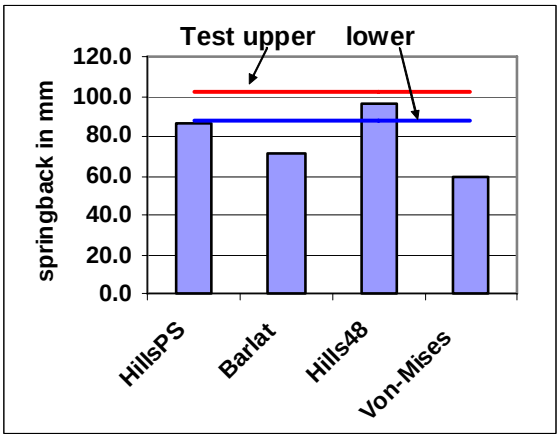

Figure 3.20. Springback results for different material models.

Severe Bauschinger effects were found in various experiments of AHSS [56]. Figure 3.21 shows typical stress and strain data measured in a tension and compression test for DP780. The reverse loading yield stress is significantly lower than the loading yield stress and the isotropic hardening model may introduce a large stress prediction error if a part has a loading and reverse loading deformation such as a bending and unbending deformation when metal flows through a tool radius or draw bead. Therefore, a new material hardening model is needed to describe this Bauschinger effect so that this material behavior can be modeled correctly in sheet metal forming.

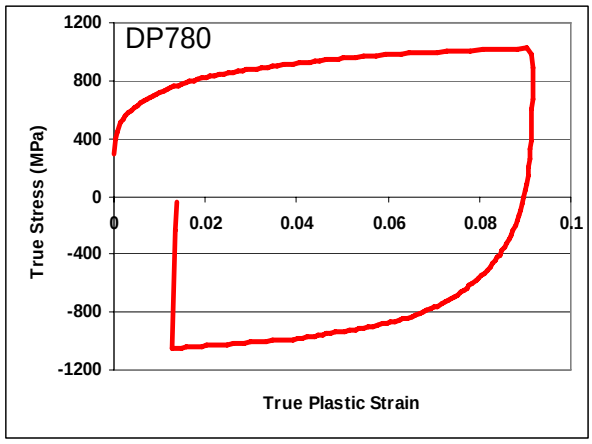

Figure 3.21. Bauschinger effect for DP780.

In this study, Yoshida's combined isotropic/kinematic model [51] was used to describe the deformation behavior of large-strain cyclic plasticity. Its new equation of back stress evolution gives a more accurate description of the transient Bauschinger effect. The model consists of seven constitutive parameters which can be determined using cyclic tests, such as tension and compression, or bending and unbending tests. In

the original Yoshida model, saturation functions were used in the hardening law, which may not be able to accurately represent the stress-strain hardening behavior for AHSS. Figure 3.22 shows the stress strain curve obtained from uniaxial tension test and extrapolated by power law. The curve shows a continuous work hardening behavior at a larger strain greater than 0.2 while the original Yoshida hardening model is not able to model this stress level increase. To resolve the stress saturation problem, a modified hardening law was introduced by changing the equation for evolution of the isotropic hardening of the bounding surface, as described in [56]. With this new hardening law, two more material parameters describing this continuous hardening behavior are introduced. Those two additional parameters, together with the initial seven (7) parameters in the Yoshida model, can be obtained by cyclic tension and compression tests. Figure 3.22 shows the comparisons between the test data and the prediction with the modified material mode for DP780. It is obvious that the new modified hardening model can capture the stress-strain relationships in both a uniaxial tension (Figure 3.22 a) and a cyclic tension and compression tests (Figure 3.22 b). Table3.3. lists the nine parameters which will be used in the case studies in the later section.

Table 3.3. Parameters for the Yoshida model with modified hardening law

Mat	Y MPa	B MPa	C	m	b MPa	h	K MPa	N	eo
DP780	**291.6**	**453.5**	**513.2**	**62.5**	**449.1**	**0.95**	**700.0**	**0.955**	**0.052**
DP980	**399.1**	**822.2**	**275.4**	**44.0**	**405.1**	**0.45**	**0.0**	**0.0**	**0.001**

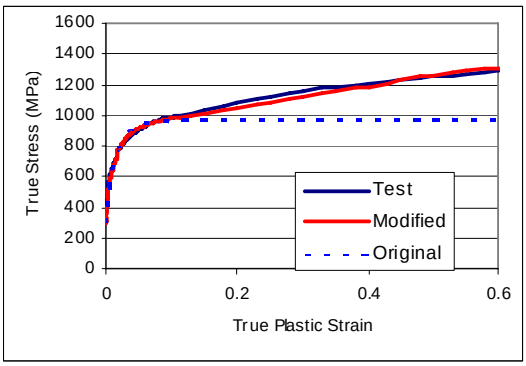

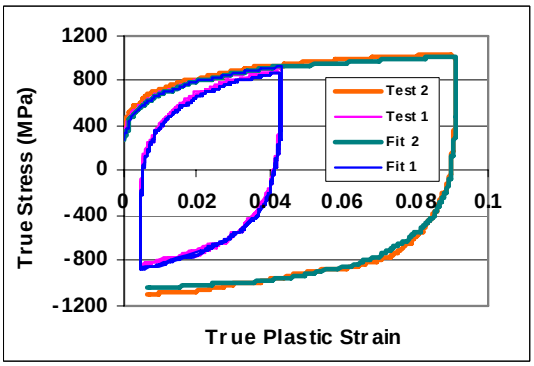

(a) Extended uniaxial tension (b) Cyclic stress-strain response

Figure 3.22. The comparisons between the test data and the predicted stress with the modified Yoshida model

3.5. Case study

Three automotive industrial parts: a fender load beam, a cross member (Numisheet 05 benchmark part) and a rail, as shown in Figure 3.23, Figure 3.24, and Figure 3.25, respectively, were used as full scale component case studies for validation studies. In this study, the major focus is on springback results with new simulation features. Forming simulation will not be presented in detail.

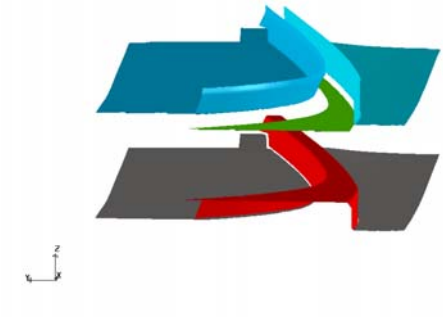

Figure 3.23. FE model of fender load beam.

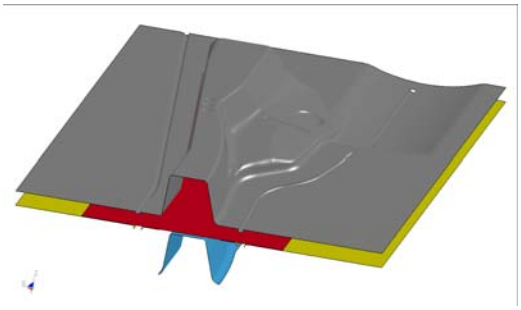

Figure 3.24. FE model of cross member.

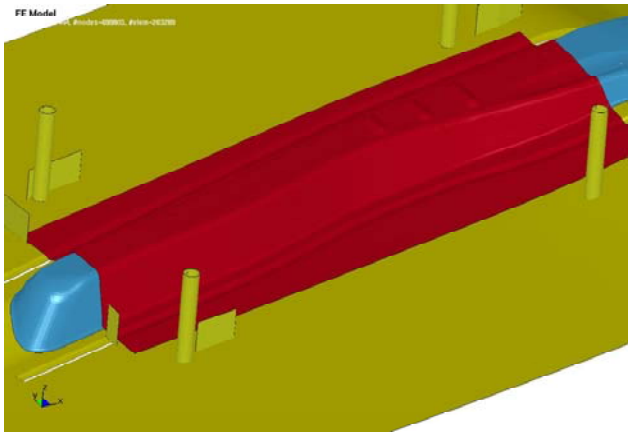

Figure 3.25. FE model for automotive rail.

The full scale case-studies were conducted to verify the effectiveness of the newly developed simulation technology (NDST) in springback predictions, which includes selective mass scaling, smooth contact and the Yoshida isotropic/kinematic hardening model with modified hardening law. Simulation results were compared to the experimental data and baseline results. The baseline setup used the conventional contact and mass scaling method with isotropic hardening material model. All other simulation parameters used in the baseline model are the same as those of NDST.

The first case is a fender load beam of DP780 steel as shown in Figure 3.23. The springback (resultant displacement) and forming results are shown in Figure 3.26. Figure 3.27(a) depicts the springback results in various sections while Figure 3.27 (b) shows a larger view of a typical section from the part, where the section lines, from inner to outer, represent the results of: formed part, baseline, smooth contact, modified Yoshida model, NDST and experiment. We can see that the baseline model over-predicts the twist and under-predicts springback (the sidewall and flange opening angles). The use of smooth contact and modified Yoshida Model greatly improves the prediction while the result from the NDST is the best when compared to experimental data. The maximum deviation between predicted data from the baseline model and experimental data is 8.6 mm, while the maximum deviation between predicted data from the NDST and measured data is 2.1 mm. It is obvious that the use of the NDST significantly improves the springback prediction. Similar comparison is found for DP980 steel as shown in Figure 3.28.

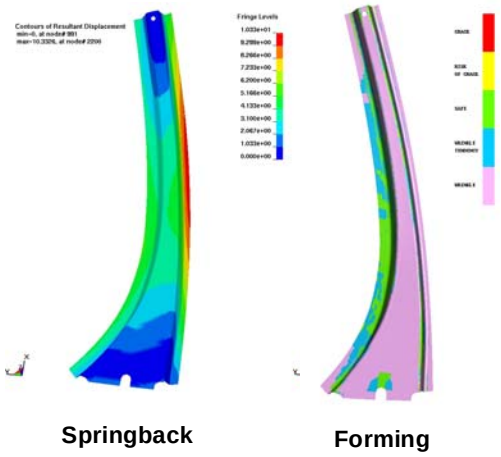

Figure 3.26. General view of Springback and forming results.

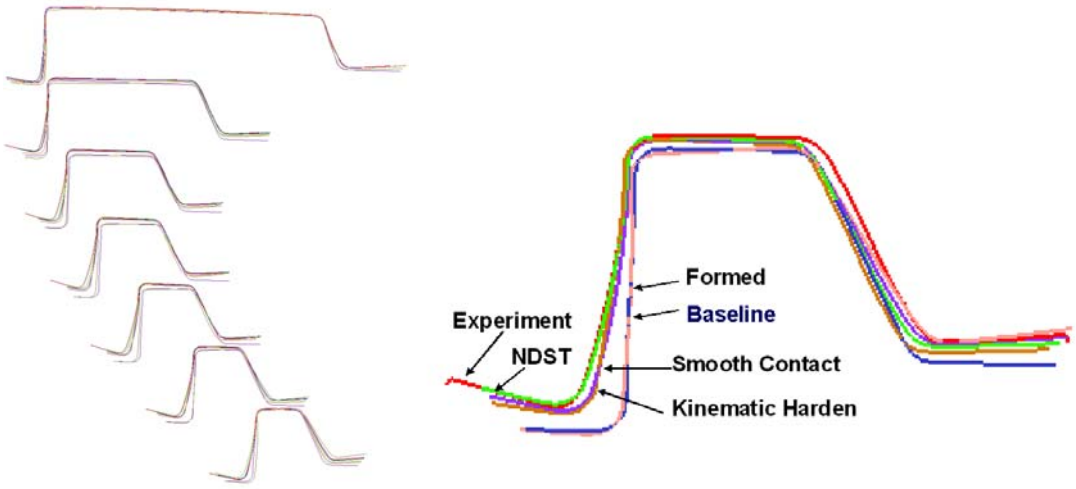

(a) Overall picture of all sections. b) A typical section

Figure 3.27. Springback result comparison for fender load beam (DP780)

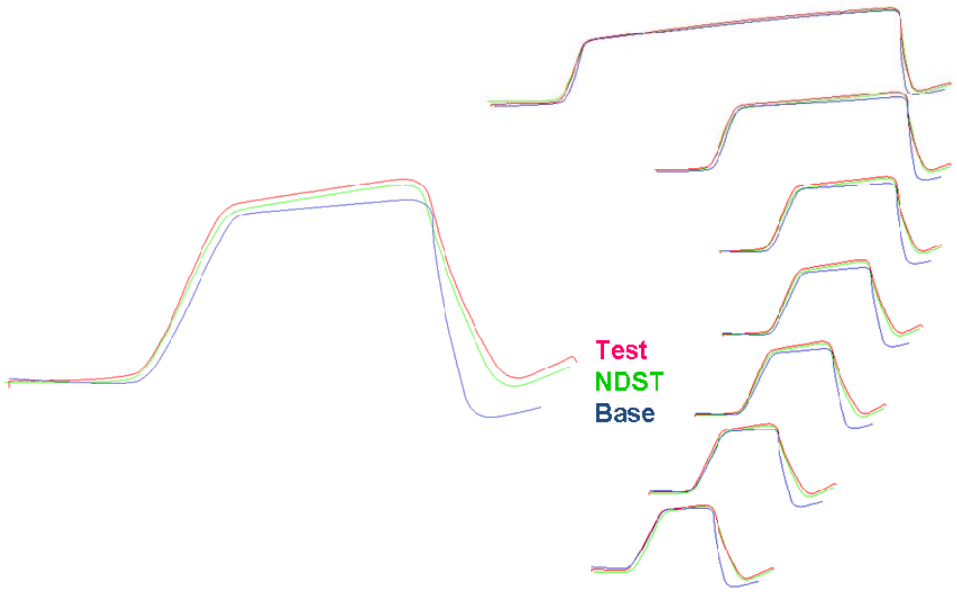

(a) A typical section. b) Overall picture of all sections

Figure 3.28. Springback result comparison for fender load beam (DP980).

The FE model of the second larger-scale case is shown in Figure 3.25. Simulations include forming, trimming, and then springback for both DP600 and DP780, as shown in Figure 3.29. Figure 3.30 shows the springback comparison among the base line model, NDST and experiment for DP600. It is seen that the baseline result over-predicts the twist. The use of the NDST significantly improves the springback prediction and the predicted results agree well with experimental data.

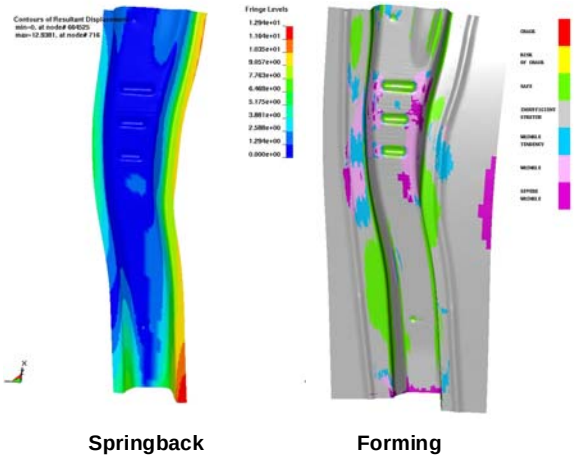

Figure 3.29. Forming and springback results of an automotive rail.

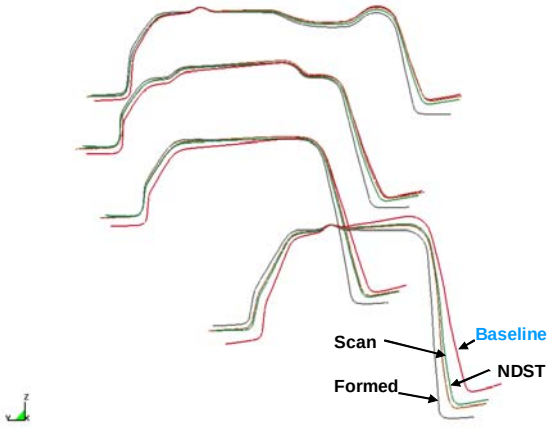

Figure 3.30. Springback comparison of DP600.

The third case is the Numisheet 05 benchmark (a cross member) as shown in Figure 3.24. Figure 3.31 shows the results of forming and springback after trimming for DP780. The section view of the part is shown in Figure 3.32 for the baseline model, the NDST and experiment. The result in this case shows that the side wall curl is well captured using the NDST and the overall springback prediction using the NDST is much better than that using the baseline model.

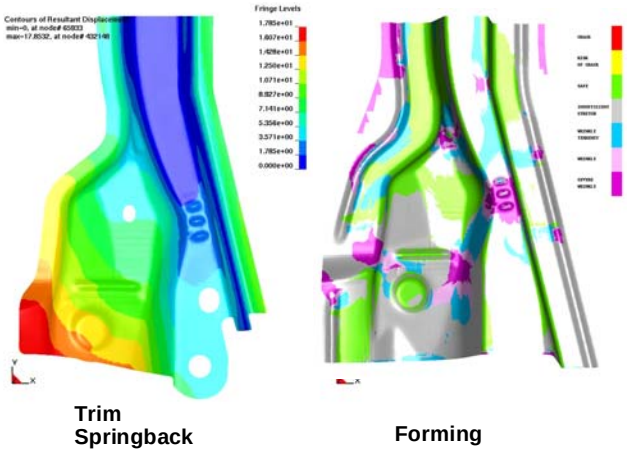

Figure 3.31. Forming and springback results of a cross member.

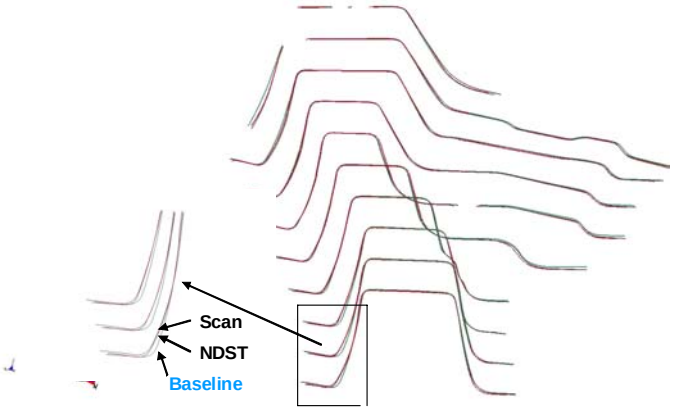

Figure 3.32. Springback comparison of DP780.

3.6. CONCLUSIONS

- Simulation parameter sensitivity study was conducted on a Slit-Ring test. The variation of springback simulation results of DQSK steel is within 10% in the selected parameter ranges.
- Six different materials were simulated and compared to experiments. The maximum deviation of outer diameter from forming predictions is less than 3%. For springback predictions, two mild steel results are close to the experimental data, while the AHSS results are about 10% under-prediction.
- Springback prediction is much more robust and accurate when selective mass scaling is used to reduce the dynamic effect.
- The use of the smooth contact method reduces the contact errors during forming and significantly improves the springback prediction.
- Using modified Yoshida's nonlinear isotropic/kinematic hardening material model can adequately describe AHSS deformation behavior (Bauschinger Effect) and significantly improve the springback prediction.
- The springback prediction can be significantly improved using the newly developed simulation technology (NDST) which includes the use of the smooth contact, selective mass scaling and Yoshida nonlinear isotropic/kinematic hardening models, as demonstrated in the three full scale automotive component case studies.

CHAPTER 4. SHEAR FRACTURE PREDICTION

4.1 INTRODUCTION

Shear fracture is one of AHSS issue encountered in forming processes, which usually occurs on the punch/die radius as the material is stretch bent over a sharp radius. The fracture presents 45^{o} crack through the sheet thickness, and is thus termed 'shear fracture'. Figure 4.1 shows some examples of shear fractures in stamped automotive parts. Insignificant material necking/thinning is observed in this type of fracture, thus, failure is difficult to predict with the conventional FLC, because the FLC is created to predict the initiation of localized necking. Figure 4.2 shows an example of shear fracture for an automotive B-pillar made from a DP980 steel. Fracture occurred on the drawbead area (small radii), and it was not predicted by the simulation using the FLC.

Figure 4.1. Examples of shear fracture in automotive applications.

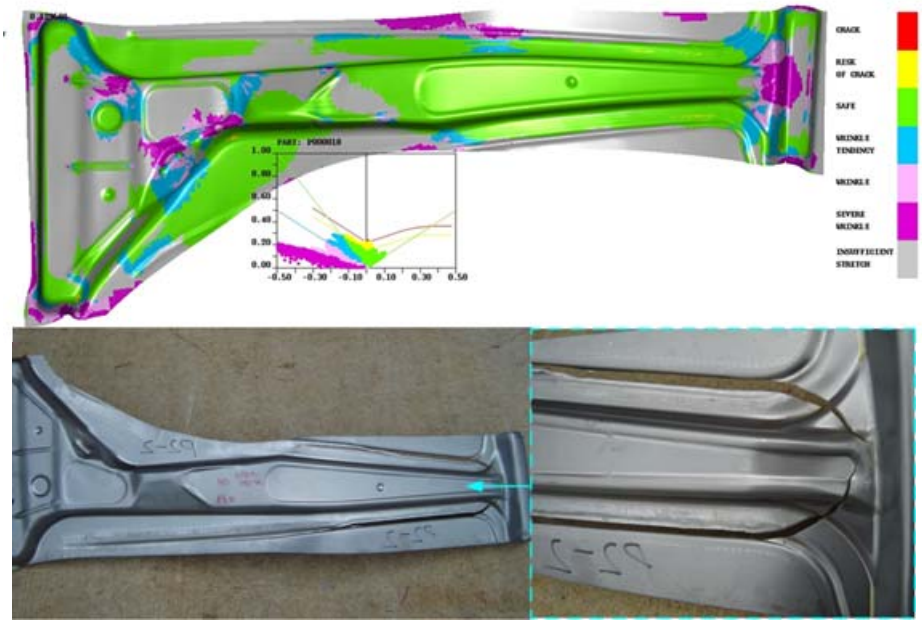

Figure 4.2. Shear fracture for an automotive B-pillar made from a DP980 steel, fracture can not be predicted by FLC.

As shown in Figure 2.6, a dimple structure in the fracture cross-section is observed, indicating that the fracture is ductile rupture which is similar to the fracture of conventional steel. However, when using ductile fracture criteria to analyze the AHSS shear fracture, higher local deformation (thinning) was calculated [8]. This is because these criteria were developed from conventional lower strength steel and can not be applied to AHSS analysis directly. Some empirical failure criteria were developed from laboratory tests [63, 66, 67]. They can be used in the particular case studies to predict shear fracture, but can not be always applied complex geometry and general cases.

During stamping, failures of conventional steels occur either in the side wall or the tangent point off the die radius. The failure mode is mainly a tension type of fracture,

while the shear fracture of AHSS behaves differently and occurs at a die radius. The fracture mode can be a combination of tension, compression and shear stresses. It is better to use a failure criterion including various stress states. The Modified Mohr-Coulomb (MMC) model considers a wide range of stress states combining normal and shear stresses. It is based on the classical Mohr-Coulomb theory, which is an extension of the maximum shear criterion. Hence the MMC criterion is more suitable for shear fracture prediction than the others that do not consider shear stress effects. The MMC criterion is also easier to be calibrated from simple laboratory-based experiments compared to other existing ductile fracture models.

In this study, the SFS and BUT tests are used to validate the MMC fracture criterion. The MMC model parameters are calibrated for a DP780 steel using various laboratory experiments. FEA software packages ABAQUS and LS-DYNA are used in the simulations with implemented user subroutines for the MMC fracture model. A good agreement has been obtained between the simulation results and experimental data.

4.2 MMC FRACTURE CRITERION

The Mohr-Coulomb (M-C) fracture criterion assumes that the fracture occurs when a combination of normal stress σ_n and shear stress τ reaches a critical value and it is expressed as:

$$\tau + C_1 \sigma_n = C_2 \qquad (4\text{-}1)$$

Where C_1, and C_2, are material constants. Bai [83] modified the M-C criterion by transforming it from a stress-based form to a mixed strain-stress space of ($\bar{\varepsilon}_f$, η , $\bar{\theta}$). The modified form of the MMC fracture criterion is expressed as

$$\hat{\varepsilon}_f = \left\{ \frac{A}{c_2} \left[c_3 + \frac{\sqrt{3}}{2-\sqrt{3}} \left(1-c_3\right) \left(\sec\left(\frac{\bar{\theta}\pi}{6} \right) - 1 \right) \right] \left[\sqrt{\frac{1+c_1^2}{3}} \cos\left(\frac{\bar{\theta}\pi}{6} \right) + c_1 \left(\eta + \frac{1}{3} \sin\left(\frac{\bar{\theta}\pi}{6} \right) \right) \right] \right\}^{-\frac{1}{n}} \tag{4-2}$$

Where $\bar{\varepsilon}_f$ is the equivalent strain at fracture, stress triaxiality $\eta = -p/\bar{\sigma}$ is the normalized hydrostatic pressure, p is the hydrostatic pressure and $\bar{\sigma}$ is the effective stress. $\bar{\theta}$ is the normalized lode angle parameter which can be calculated from the invariants of stress deviator J_2, and J_3 as

$$\theta = \frac{1}{3}\cos^{-1}\left(\frac{3\sqrt{3}}{2} \frac{J_3}{J_2^{3/2}} \right), \quad (0 \le \theta \le \frac{\pi}{3}); \;\; \bar{\theta} = 1 - \frac{6\theta}{\pi} \tag{4-3}$$

c_1, c_2 and c_3 are material parameters related to fracture and can be calibrated from tests. A and n are the power law hardening parameter of the material from a stress-strain curve. All the material parameters for DP780 are listed in Table 4.1. The geometric representation of the MMC fracture envelope is 3D half-tube which is asymmetric with respect to $\bar{\theta} = 0$ as shown in Figure 4.3 [83]. In the plane stress case which most sheet forming processes hold, $\bar{\theta}$ can be eliminated and the MMC criterion can be simplified to a function of variable η for a given material. Figure 4.4 shows a typical MMC fracture locus under plane stress conditions [74]. Various experiments can be used to calibrate the material parameters. The typical ones and the corresponding range of triaxiality values are also shown in Figure 4.4.

To determine the fracture limit, a damage parameter, which is proportional to the accumulated equivalent plastic strain, is introduced, as shown in Equation (4-4).

$$D = \int_0^{\bar{\varepsilon}_f} \frac{d\bar{\varepsilon}_p}{\hat{\varepsilon}_f(\eta, \bar{\theta})} \tag{4-4}$$

When a material reaches its limit of ductility, D reaches the critical value Dc, usually taken as unity and the corresponding material element fails and fracture initiates. Then, the neighboring elements experience additional stress due to the stress concentration and the damage in those elements increase as a result, which lead to fracture propagation through and form a crack.

4.3 MATERIAL AND CALIBRATION

The material used is DP780 steel. The material properties obtained from tension tests are listed in Table 4.1. Various tests were performed to calibrate the MMC fracture criterion [74] and its locus in plane stress condition is shown in Figure 4.5. The material constants for MMC are also shown in the table.

Table 4.1. Material Properties and MMC constants

Steel Grades	YS (MPa)	TS (MPa)	TE %	A (MPa)	n value	$\bar{R}$	c_1	c_2	c_3
DP780	596	838	17.1	1233	0.11	0.89	0.123	604.6	0.958

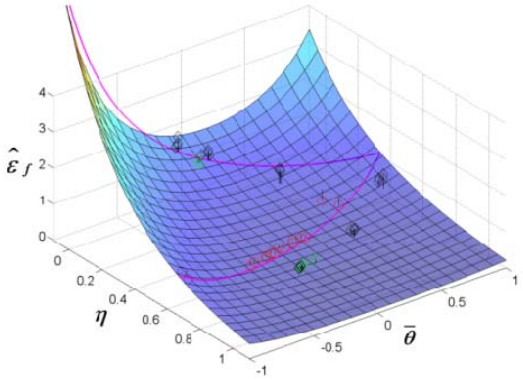

Figure 4.3. The MMC fracture 3D envelopes for DP780 [83].

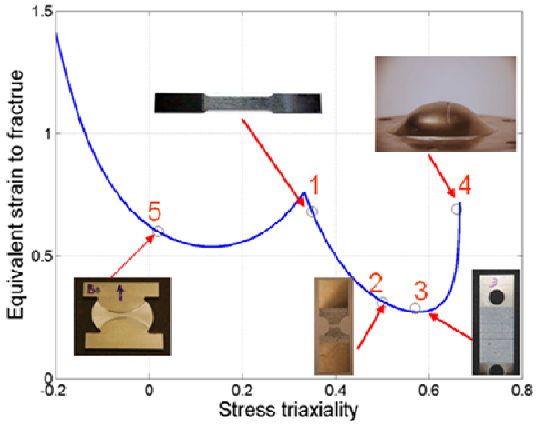

Figure 4.4. Typical MMC fracture locus for plane stress.

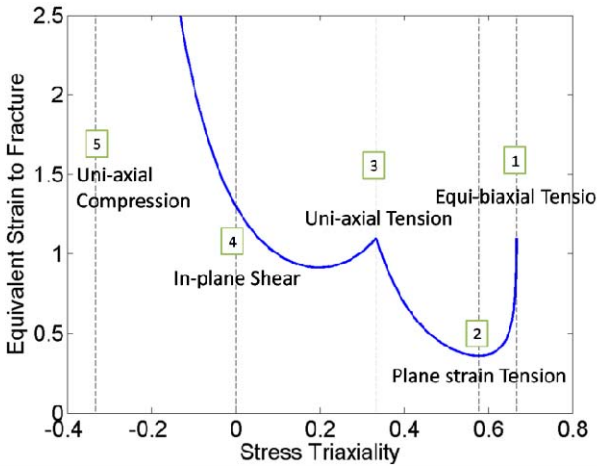

Figure 4.5. MMC fracture criterion locus for DP780 steel [74].

4.4. FINITE ELEMENT SIMULATION

Two different laboratory forming tests were used to validate the MMC criterion. Both laboratory tests can simulate the drawing of a blank over a die radius and produce shear fracture and other types of fracture. For AHSS, three types of specimen failures were observed [71,81]: failure on the radius, failure at the boundary or tangent point

between the radius and the sidewall, and failure in the sidewall (tension failure), as shown in Figure 4.6. Different types of fracture can be obtained in tests by changing the R/t ratio or by adjusting the back tension force in the BUT test. Details of the test are described in [71] and the test data for DP780 steel were used in the validations of finite element simulations.

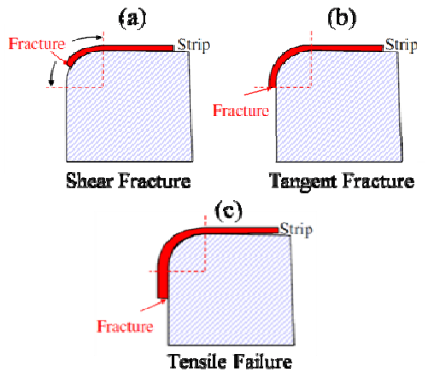

Figure 4.6. Three types of fractures [71].

4.4.1. Laboratory Tests

The two laboratory tests used for this validation are the stretch forming simulator (SFS) and the bending under tension (BUT) [71]. The SFS test is described in Figure 4.7 (a) and the corresponding FE model is shown in Figure 4.7 (b). During the forming process, the steel strip is clamped at both ends, and the upper die moves down and pulls the strip downward until the sheet strip fails. The lower die is fixed with changeable radii to provide various R/t ratios. The tension level in the strip can be controlled by adjusting the clamping distance. There are two load cells in the lower die to record horizontal and vertical reaction forces. In this study, the dimension of the test strip is 50.8mm x 610mm.

Quasi-static SFS tests were performed with a constant upper die speed of 0.25m/min, a fixed clamping distance of 460mm. A Teflon film was used to reduce friction between strips and dies. Four different lower die radii, 1.5mm, 3mm, 5mm, 10mm, were adopted for the testing, and every strip specimen was tested all the way to fracture. Photographs of typical fractured strips for each lower die radius are shown in Figure 4.13. One can see a clear transition of fracture location from sidewall to die radius and the fracture mode from a tensile failure to a shear fracture as the die radius decreases.

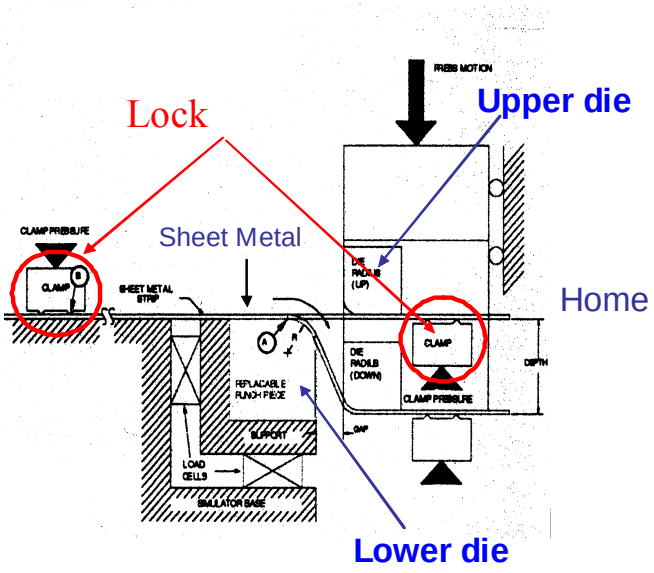

(a)

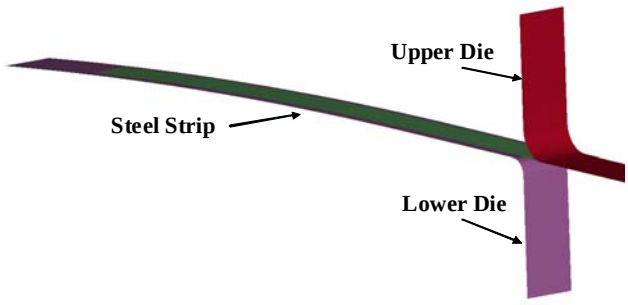

(b)

Figure 4.7. (a) Schematic of SFS test [71], (b) FE model.

The BUT test is described in Figure 4.8(a) and the corresponding FE model is shown in Figure 4.8(b). During the test, steel strip is drawn over a fixed pin (roller) with a pair of independently controlled hydraulic actuators. One actuator provides a constant restraining force (back tension) while the other pulls the strip at a constant speed. Different R/t ratios can be obtained using different pin diameters. Different types fracture can also be obtained by changing the back tension level.

Figure 4.8. (a) BUT test, (b) FE model

4.4.2. Simulation Parameter Sensitivity Study

Validation simulations were conducted using FE software packages of ABAQUS and LS-DYNA with 3D solid and shell elements. The dynamic explicit method was used in this work since it is commonly used for metal forming simulations. Hill's 1948 anisotropic yield criterion with the associated flow rule and the isotropic hardening law were used. To minimize the error from the simulation setup, a parameter sensitivity study was performed to find the optimal values for each model. In this study, the selected parameters for the sensitivity study include the mesh size, the element type and the coefficient of friction [72, 84]. The sensitivity study was conducted using the SFS model.

Element Type: (1) An eight (8) node 3D solid element with five (5) layers of elements through the thickness; (2) A fully integrated shell element with seven (7) integration points through the thickness. The selected element types provide sufficient accuracy for stress distribution.

Mesh Size: Various mesh sizes were evaluated to find the one with a satisfactory accuracy while maintaining the computational efficiency. A simpler approach to minimize the effect of mesh size is to keep a consistent length scale in fracture model parameter calibrations and simulations. Figure 4.9 shows the fracture location comparison for four element sizes, 0.2, 0.33, 0.5 and 1.0 mm. The size that best to matches the fracture location in the experiment is 0.2 mm. Figure 4.10 shows the comparison of forming forces. The predicted forces are slightly lower than the experimental data, but there is low sensitivity to the mesh size. Therefore, 3D elements with edge length of 0.2 mm were used in the simulations to obtain the fracture strain, which is consistent with the length scale adopted in the Digital Image Correlation (DIC) in the MMC model parameters calibrations. Readers can refer to [74] for the detailed information about the fracture model parameters calibrations.

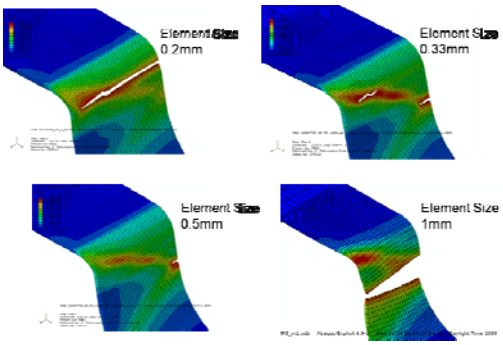

Figure 4.9. Effect of mesh size on fracture location (Solid).

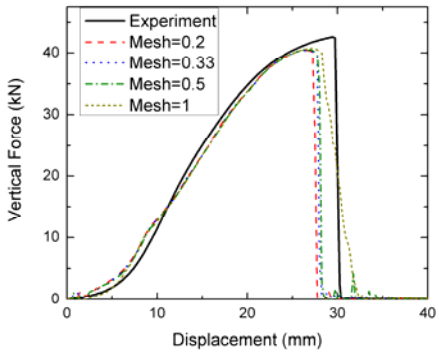

Figure 4.10. Effects of the mesh size on the force-displacement

As for the shell element model, it is better to keep the element edge length larger than the sheet thickness in order to ensure the thin shell assumption. Four different sizes of the shell element of 0.25, 0.5, 1.0 and 2.0 mm were tested. As shown in Figure 4.11, the 1 mm size is sufficient in accuracy to match the experimental result.

Coefficient of Friction: Various coefficients were tried, 0.05, 0.12, 0.15 and 0.2. It is found that the best one to match experimental result falls in between 0.05 to 0.12 as shown in Figure 4.12. The result correlates well with experiment since a thin Teflon film was used between the blank and the die without adding extra lubricant during testing. Therefore, the friction of coefficient of 0.1 is used in the simulation.

The final parameters used in simulations are: solid element size 0.2mm, shell element 1.0 mm and coefficient of friction 0.1.

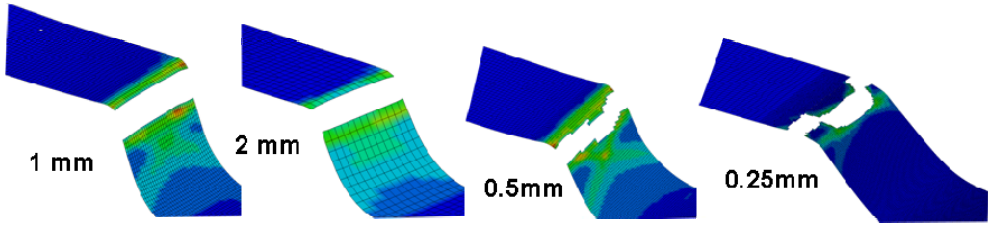

Figure 4.11. Effect of mesh size on fracture location (Shell).

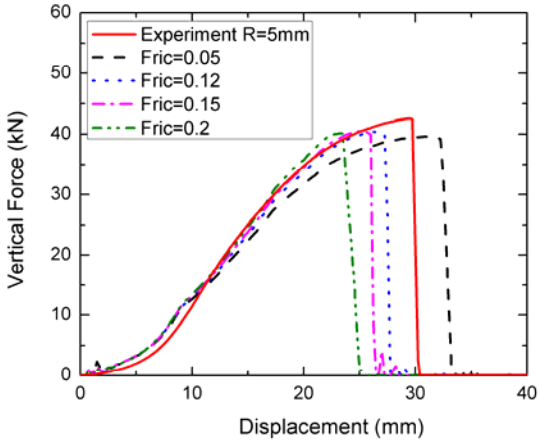

Figure 4.12. Effects of the friction coefficient on the force-displacement.

4.4.3. Results and Comparison

Four different R/t ratios of 1.5, 3, 5 and 10 were simulated in the SFS. Figure4.13 (a) shows the trend of fracture locations. As the die radius increases, the fracture locations transfer from die radius to side wall. Figure 4.13 (b) shows the comparison in fracture locations for the solid element results. It can be seen that the simulation results match the experiment data well. The fracture locations occur on the radius for R/t values of 1.5 and 3.0, at the tangent point for R/t=5 and in the side wall for R/t =10. Figure 4.14

shows the comparison of force-displacement curves. The overall trends and maximum peak forces are also predicted very well.

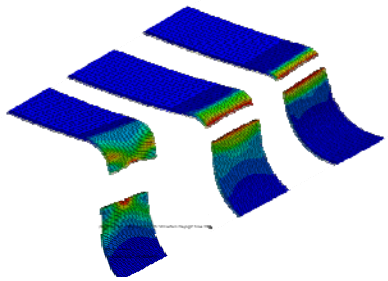

Figure 4.13 (a). Trend of fracture locations

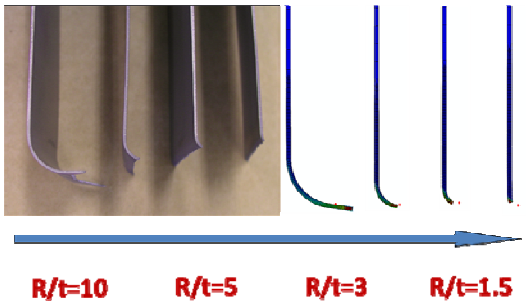

Figure 4.13 (b). Prediction of fracture locations with solid element.

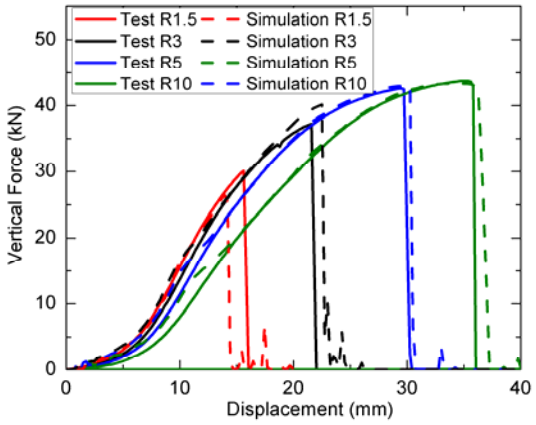

Figure 4.14. Comparisons of force-displacements using solid elements.

The results for shell element comparisons are similar. Simulations capture the fracture locations very well as shown in Figure 4.15. The force predictions are also in a good agreement with the test data overall but with a slightly lower displacement at failure, as shown in Figure 4.16.

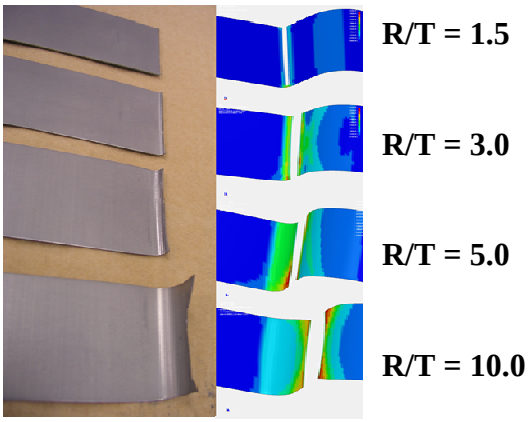

Figure 4.15. Comparisons of fracture locations for shell elements

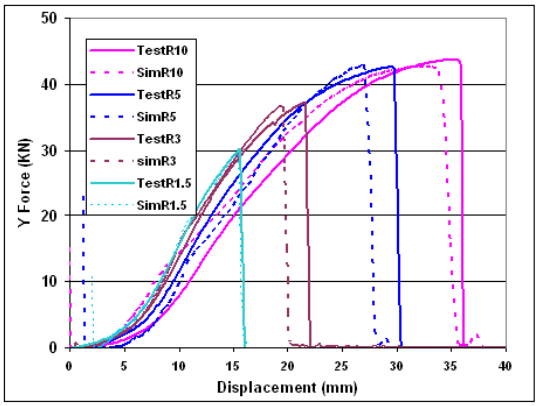

Figure 4.16. Comparisons of force-displacement curves for shell Elements.

For the BUT simulation, the R/t value was kept at 3.0 and various back tension forces were applied to obtain different types of fractures. Figure 4.17 shows the comparison in fracture locations, and the simulation results agree well with the experimental data. Figure 4.18 shows the comparison of force-displacement curves. The maximum forces are well predicted but the overall force is slightly higher in simulations,.

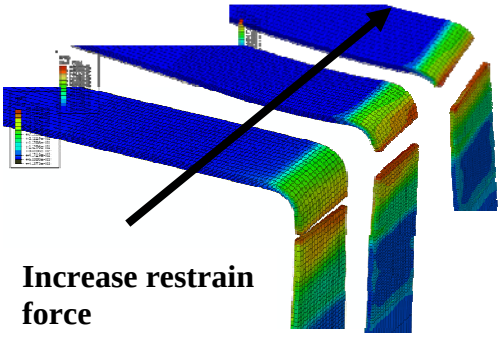

Figure 4.17(a). Predicted fracture locations for the BUT test.

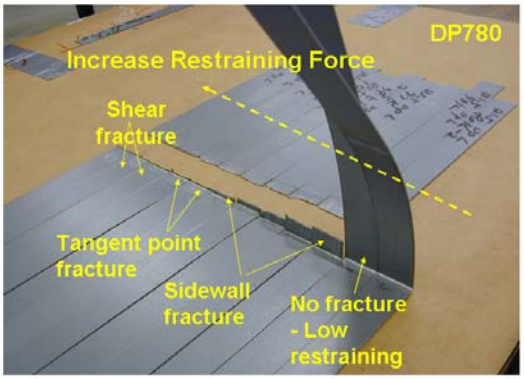

Figure 4.17(b). Three types of fractures in BUT test.

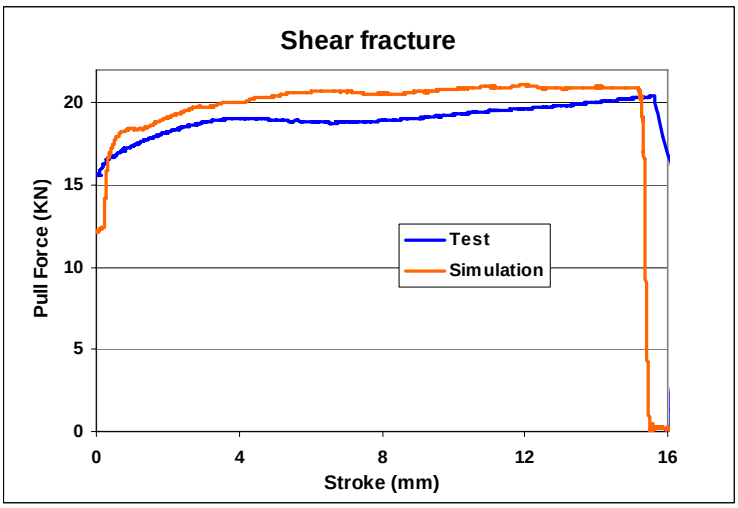

Figure 4.18. Comparisons of force-displacement curves for the BUT.

Figure 4.19 shows the empirical shear fracture limit curve (fracture at tangent) obtained from experiments [71]. Simulations using various R/t ratios and the back tension levels were also performed and the simulation results are also plotted in Figure4.19 with the indication of failure locations. It is observed that the simulations can predict fracture types and fracture locations when the R/t ratio is small. However, when the R/t ratio is larger than 5, simulations predicted a side wall failure while the experiments showed tangent point failure. This indicates that the MMC model is capable of predicting shear fracture but still needs improvement for tensile failure predictions at large R/t ratios. Therefore, in simulations, both the MMC fracture model and the conventional FLC method should be used to predict all failure modes: use the MMC model for shear fracture prediction and the FLC for tensile failure or localized necking prediction.

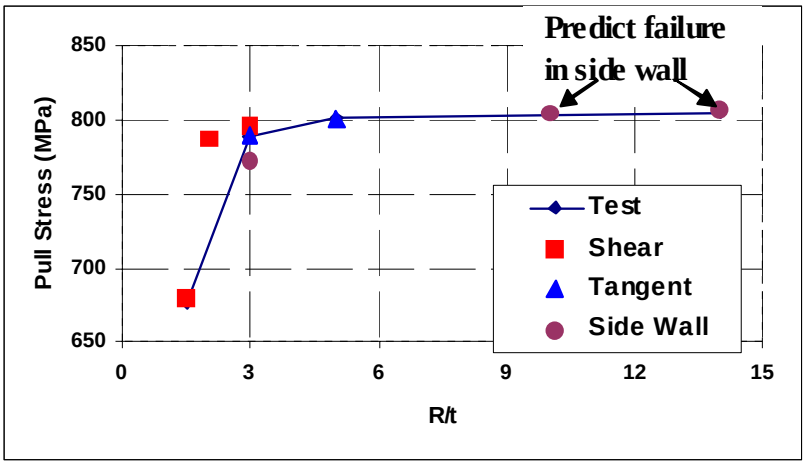

Figure 4.19. Predicted failure types displayed in empirical shear fracture limit curve.

Figure 4.20 shows the distribution of triaxiality around the pin area in the BUT test. It is seen from the figure that the material is not purely subject to the plane stress state and the pin pressure and the unbending process change the stress state from a plane stress state to a more complicated state. Therefore the criteria for tension type of failure may not predict the shear fracture accurately.

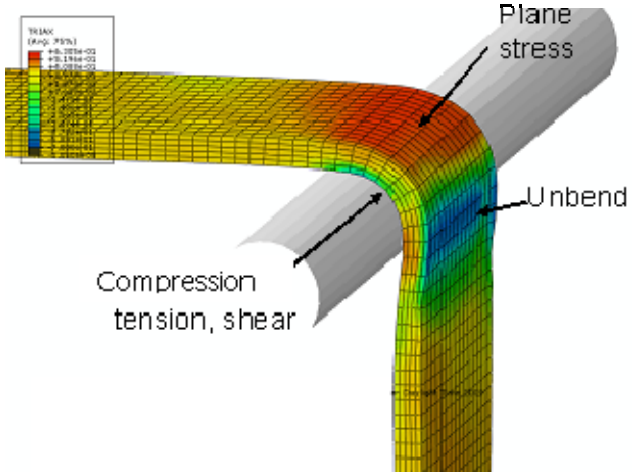

Figure 4.20. Stress states around the pin.

4.5. CASE STUDY

A preliminary study on a large part shown in Figure 4.21 was also performed with the MMC criterion. Figure 4.21 (a) shows that the shear fracture can not be predicted using FLC. When using the MMC model, the improvement of the prediction is observed, and the shear fracture occurring in the sharp radius can be captured as shown in Figure 4.21(b). However, The MMC model also predicted cracks on the corner drawing areas where no cracks occurred in the actual stamping, which is in agreement with the conventional FLC predictions. In this area, material is in a drawing mode which is a combination of tension and compression. For this mode, the calibration of MMC fracture locus is very sensitive to the magnitude of the fracture strain. Further work is needed to reevaluate the fracture locus for more general applications. This analysis suggests that the MMC model predicts shear fracture correctly while the conventional FLC predicts localized necking prior to fracture. Therefore, these two criteria should be used together to predict whichever failure mode will occur first.

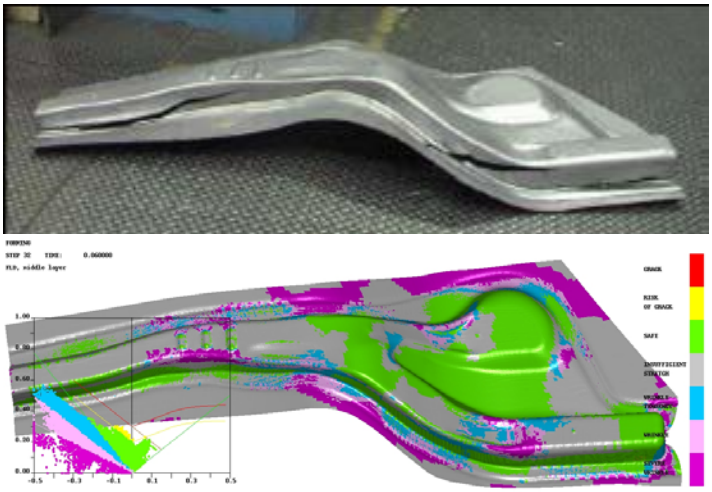

(a)

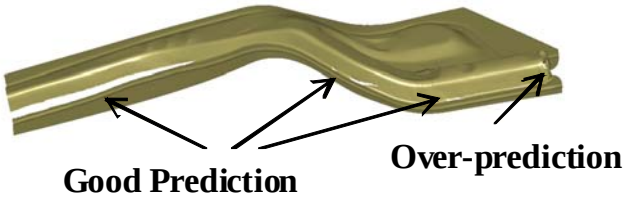

(b)

Figure 4.21. Shear fracture of a front rail using a DP780. (a) Can not be predicted using FLC, (b) Fracture can be predicted using MMC model.

4.6. CONCLUSIONS

- Simulations were conducted on the SFS and BUT tests to validate the MMC fracture criterion with a DP780 steel. The simulations achieved good agreement with the experiments predicting fracture locations for small R/t ratios. The simulations also predicted the force trends reasonably well, although the agreement was better for the SFS test than the BUT test.

- A preliminary study on a larger automotive part shows that using the MMC model improves shear fracture prediction for sharp radii. Therefore, the MMC model should be used for shear fracture predictions in tight radii, while the conventional FLC should be used for other failure predictions in sheet metal forming simulations of AHSS.

CHAPTER 5. EDGE CRACKING PREDICTION

5.1 INTRODUCTION

Stretchability or flangeability is the ability of a material to resist edge cracking during forming and flanging. Edge cracking occurs when the edge stretching reaches the forming limit. The edge stretching limit depends on both the material properties and the sheared edge condition. AHSS are more prone to edge cracking than conventional steels due to their high strength nature and the existence of hard phases in the microstructure. Figure 5.1 shows some examples of automotive parts that have experienced edge cracks. The edge stretchability of AHSS is much lower than that of conventional high strength steel and the failure cannot be predicted using conventional FLC. Figure 5.2 shows an edge cracking prediction for DP780 steel. All calculated forming strains are located below the FLC, so the part is assumed safe. However, the actual formed part experienced edge cracking. Therefore simulation technology is required to improve the accuracy for prediction of AHSS edge cracking.

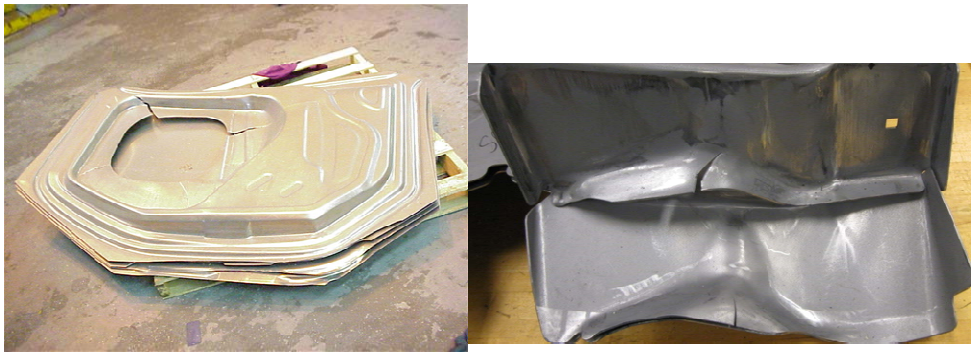

Figure 5.1 Examples of automotive parts experienced edge cracks.

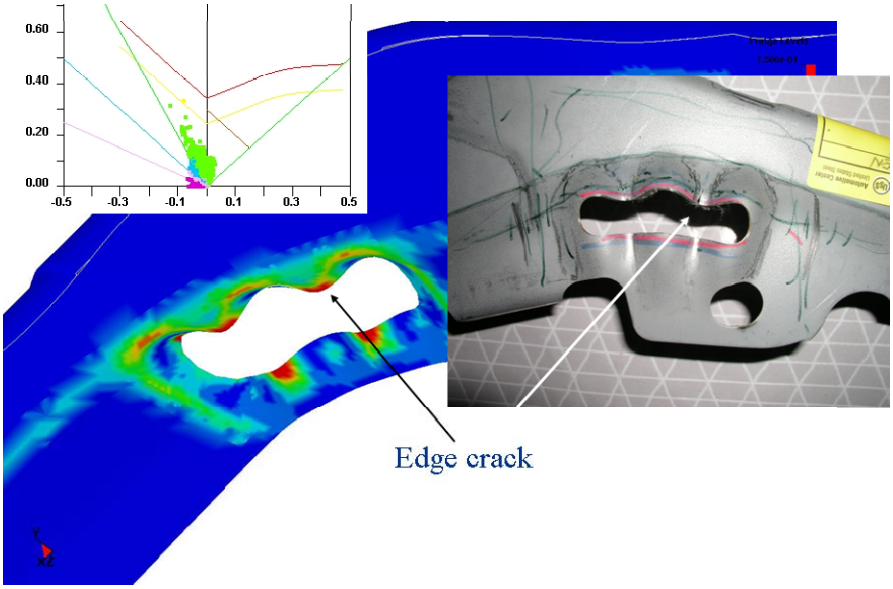

Figure 5.2. AHSS edge crack can not be predicted using conventional FLC.

One of the reasons for failing to predict edge cracking is that the damage at the edge of a sheared blank deteriorates the forming limit at the edges but is not usually considered in the subsequent forming simulation. For conventional steels, sheared edges have a regular shape and the edge quality can be measured the geometric features such as the burr height. For AHSS steels, micro-structural inhomogeneity introduces more damage in the phase boundaries. The difference in phase strengths is the dominant factor affecting the crack path and edge stretchability. Thus, the edge quality measurement approach of conventional steels cannot be used for AHSS in many cases. These findings suggest that further investigations are necessary for the AHSS blank shearing process and its effect on the edge stretching. In modeling of AHSS shearing process, the material models and failure criteria used for conventional steels need to be validated and their parameters need to be experimentally determined. Microstructure characteristics may

need to be considered because of their significant effect on fracture. It is a very challenging task to integrate them into the material models. Another difficulty is to integrate the shearing simulation results into subsequent forming analyses and to develop appropriate failure criteria for edge stretching.

Some pre-forming technologies have been used to improve the edge stretchability. In edge stretching and flanging of conventional steels, an edge usually forms a wave (or scallop) shape in the previous stage to gather material for stretching in the following stage. However, this technique is not always applicable for AHSS forming. Figure 5.2 illustrates an example of pre-forming of DP780 steel using the scallop pre-form technique. The pre-form was intended to improve the edge stretching in the later flanging process. However, the edge cracked in the pre-forming stage and the part could not withstand flanging in the next stage. AHSS pre-forming and stretching are complex forming processes. The edge experiences bending, unbending and stretching deformations. Better understanding of deformation behaviors for these processes is important for proper process design using the assistance of computer simulation.

In this study, the results of AHSS shearing experiments are reported and a new deformation measurement method is introduced. Shearing simulations were conducted and compared with the experimental data. The effect of shearing deformation on a hole expansion process was evaluated. In addition, experimental and simulation studies were conducted on pre-forming and stretching of AHSS. The digital image correlation (DIC) technique was used to measure the deformation history for both forming stages. Various finite element simulation techniques were also conducted to simulate those processes to

find better correlation with experimental data.

5.2. MATERIALS

Materials used in this chapter are HSLA350, 590R, DP600, DP780 and DP980 steels. Their tensile properties in the rolling direction (RD) are listed in Table 5.1. The n-values are calculated from the strain ranges of 5% to 10% or to the uniform elongation, whichever is smaller, and the r-values are the ratios of width to thickness strains in magnitudes, averaged from 0.2% yield point to the end of uniform elongation. HER is the hole expansion ratio obtained using the standard tests.

Table 5.1. Typical mechanical properties.

Grade	*YS (MPa)*	*UTS (MPa)*	*TE (%)*	*n value*	*R value*	*HER (%)*
HSLA350	406	488	26.2	0.159	1.11	61
590R	440	636	22.9	0.134	0.87	32
DP600	367	611	25.3	0.16	1.04	34
DP780	496	830	18.2	0.12	1.07	15
DP980	608	1064	12.5	0.09	1.10	9.0

5.3. SHEARING AND HOLE EXPANSION STUDY

5.3.1. Shearing/Piercing Tests

Shearing/Piercing tests have been performed using both laboratory and large scale tools. Figure 5.3 shows a standard laboratory test of hole expansion. A 10 mm diameter hole is pierced and then expanded using a conical punch. The material edge stretchability

is evaluated by the hole expansion ratio. Figure 5.4 shows the large scale hole expansion tests, which is for more general investigations of AHSS edge stretchability in the production environment.

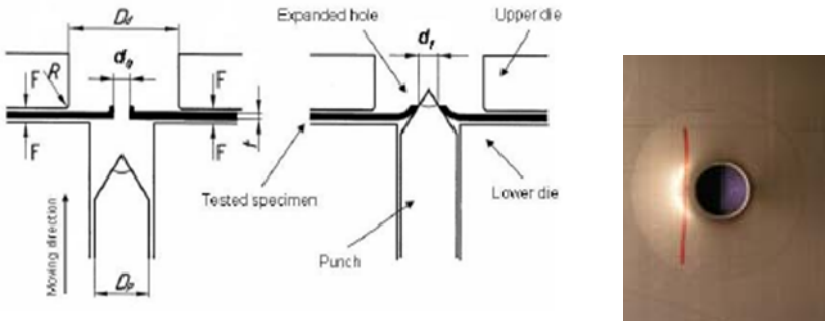

Figure 5.3. The standard laboratory conical punch hole expansion test.

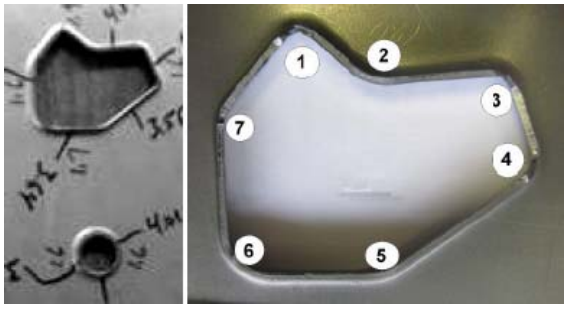

Figure 5.4. Large scale hole piercing and hole expansion tests. The flanged holes contain three features (round hole, multi-shaped hole, and curved flange).

Various AHSS have been tested. Conventional high strength steel (HSLA350) is also tested for comparison. Figure 5.5 shows typical section comparisons of the sheared edges between these types of steels. Figure 5.5 (a) is for HSLA350. The sheared edge is featured by the four zone shape, rollover, burnish, fracture and burr zones. While this feature is not seen clearly for DP780, as shown in Figure 5.5 (b). Another observation

from the figure is the rapid change in the angle of the "grade fiber," which indicates the severe deformation in shearing.

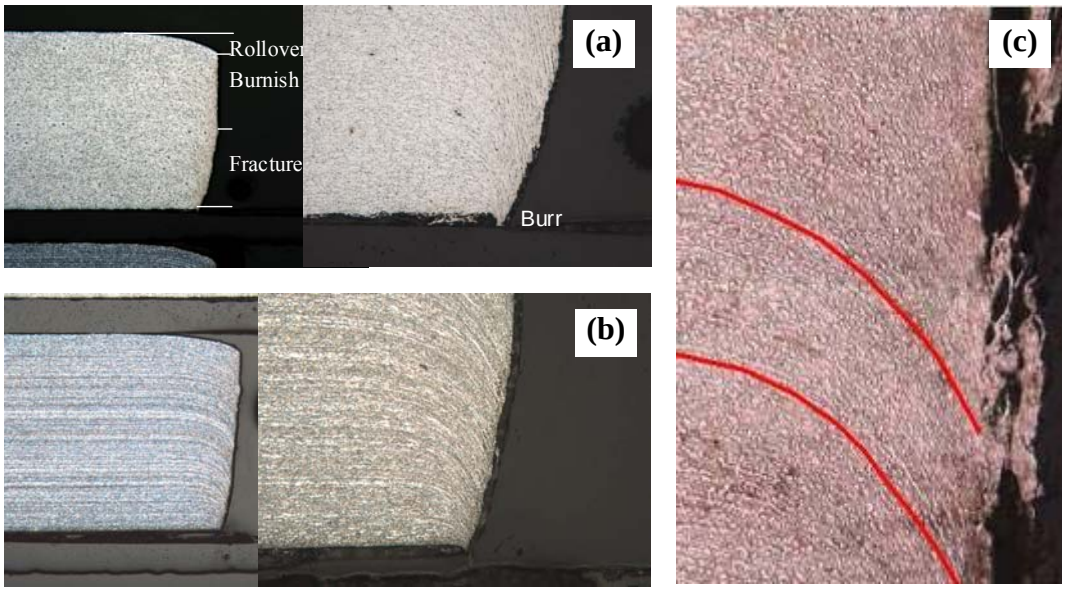

Figure 5.5. Sheared edge shape (a) HSLA 350; (b) DP780; (c) flow lines (grade fiber) in the vicinity of the sheared edge.

Detailed investigations were conducted on sheared edge characterization and flange stretch measurement. Material properties and microstructures were examined. The effects of material orientations, rolling direction (RD) and transverse directions (TD), and various tool conditions (die clearances) were also tested. The detailed results of the sheared edge characterization are recorded in [110] and are summarized in this chapter for validation of computer simulations.

To investigate the characteristics of the AHSS sheared edges, similar to conventional steels, the edge shapes are examined. Figure 5.6 shows several fractured edges of AHSS in sectioned views. Some shear fracture paths pass through the diagonal lines along the

edge corners of upper and lower tools (inclination), while others travel in the vertical direction. Some are showing the four zone edge shape, while others are missing the burr zone. This indicates that for AHSS, the shear fracture shape has a more random nature as compared to the conventional steel edges that have more repeatability and consistency with four zones. Figure 5.7 shows replica images of the fracture surfaces in various shearing conditions. To correlate the geometric feature, heights of the three zones for sectioned edge images were measured and the data are plotted in Figure 5.8 [110]. The burr heights are in much smaller length scale and are not included here. This figure summarizes the dimensions of the three zones in various conditions including steel grades, die clearances and grain directions. The following trends can be observed with the reduced die clearance, increased material strength and cutting line angle to RD:

1. Burr height reduces
2. Burnish zone height increases
3. Fracture zone height decreases
4. Roll-over zone height decreases however less clear

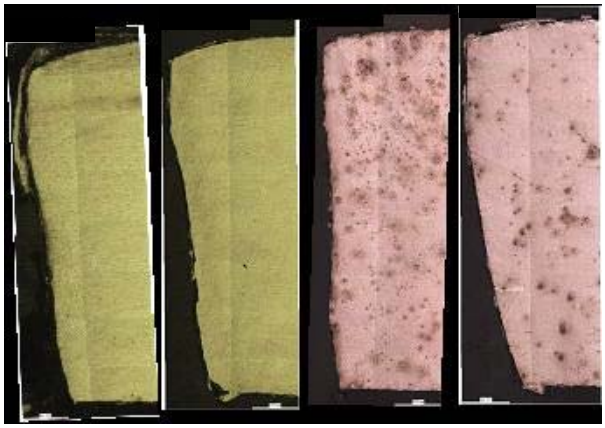

Figure 5.6. Shear fractured edges in sectioned view[110].

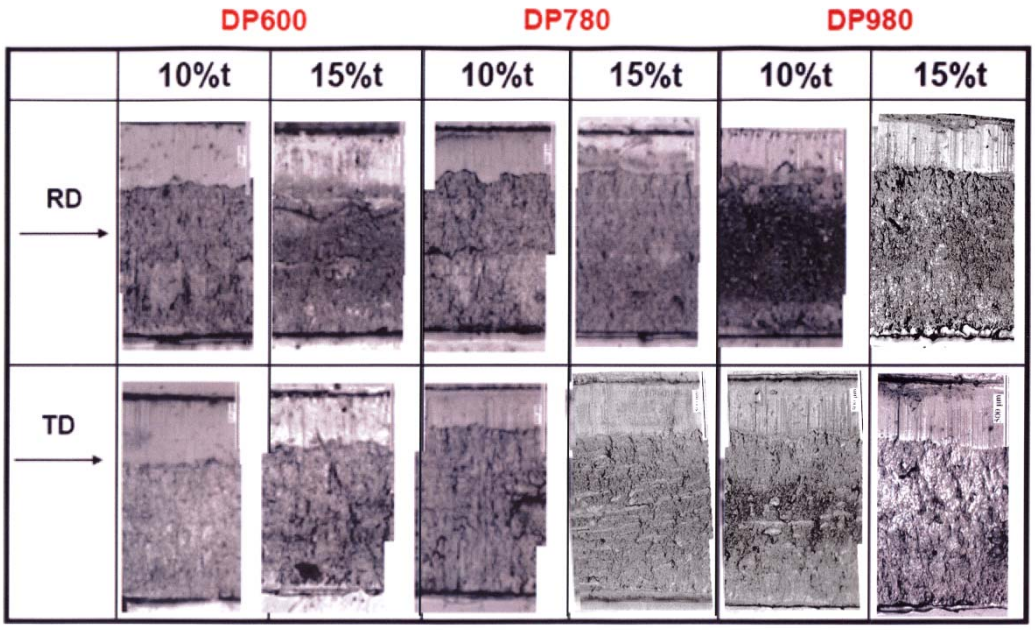

Figure 5.7. Burnish and fractured zones for different materials and blank orientations, and die clearances [110].

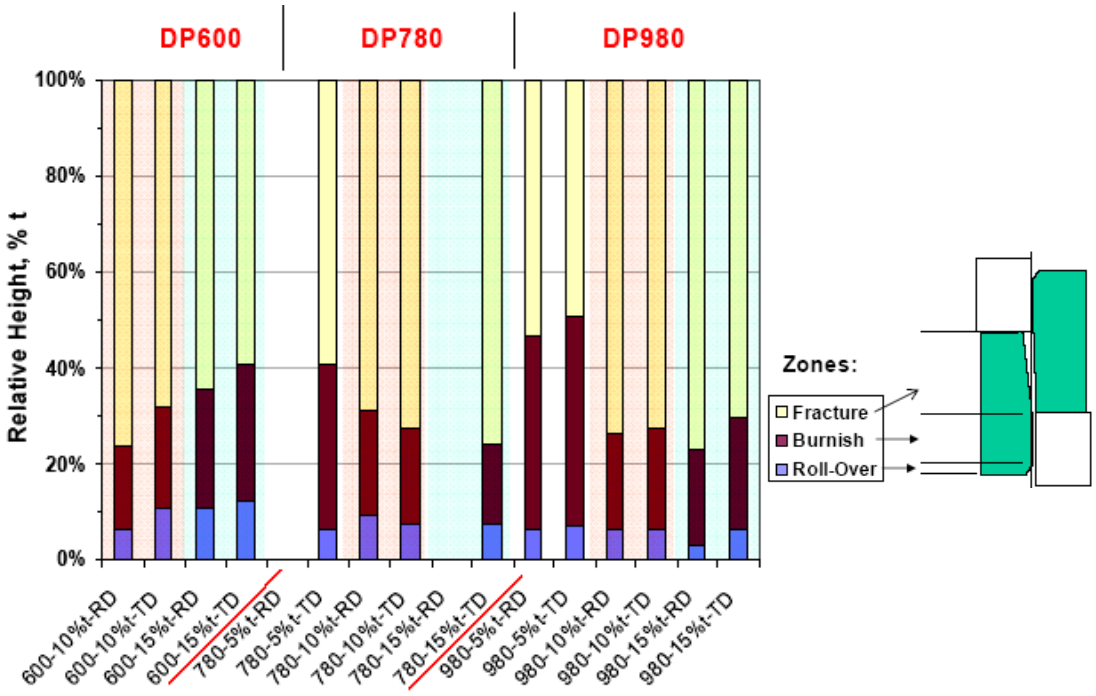

Figure 5.8. Summarized plot of relative heights of roll-over, burnish, and fractured zone for all the experimental conditions[110].

Since the edge shapes are not consistent for AHSS, an alternative method needs to be developed for characterizing the edge work hardening and quality in the shear-affected zone. Micro-hardness measurement can be used to measure the edge work hardening. However, in the current case, the data is very scattered and it is difficult to see a trend, due to the existence of two phases with different properties at a small length scale.

A digital image correlation experiment showed that the deformation in the shear zone is a simple shear dominated condition [120]. Under this condition, the shear strain is proportional to the angle change of an element. The shear deformation can be determined by measuring the angle changes. By properly preparing the samples, metal flow lines from cold rolling (parallel to the sheet surface) and its rotation after shearing can be seen clearly as shown in Figure 5.5 (c). By setting a sample coordinate system, the flow lines can be identified and the line tilting angle away from the original rolling-induced lines in the horizontal direction can be measured at each specified coordinate point. The angle field then represents the shear strain distribution in the shear affected zone.

Figure 5.9 is the plotted angle distributions away from the shear edge and from top to bottom in the thickness direction, for DP600 in RD, TD and for 10%t die clearance. Figure 5.10 shows angle distributions for DP780 and DP980 of 10%t die clearance respectively [110]. It can be seen that the shear strain is the highest at the fractured edge. Away from the edge the strain decreases quickly, and at 300μm, the strain is already very low, and at 500μm, it is zero. From the top to the bottom of the thickness and at the very edge, the highest peak appears close to mid-plane of the thickness. Better 2D flow field

plot are further given later in the simulation section (Figure 5.14-16). These plots provide valuable data for validation of computer simulations.

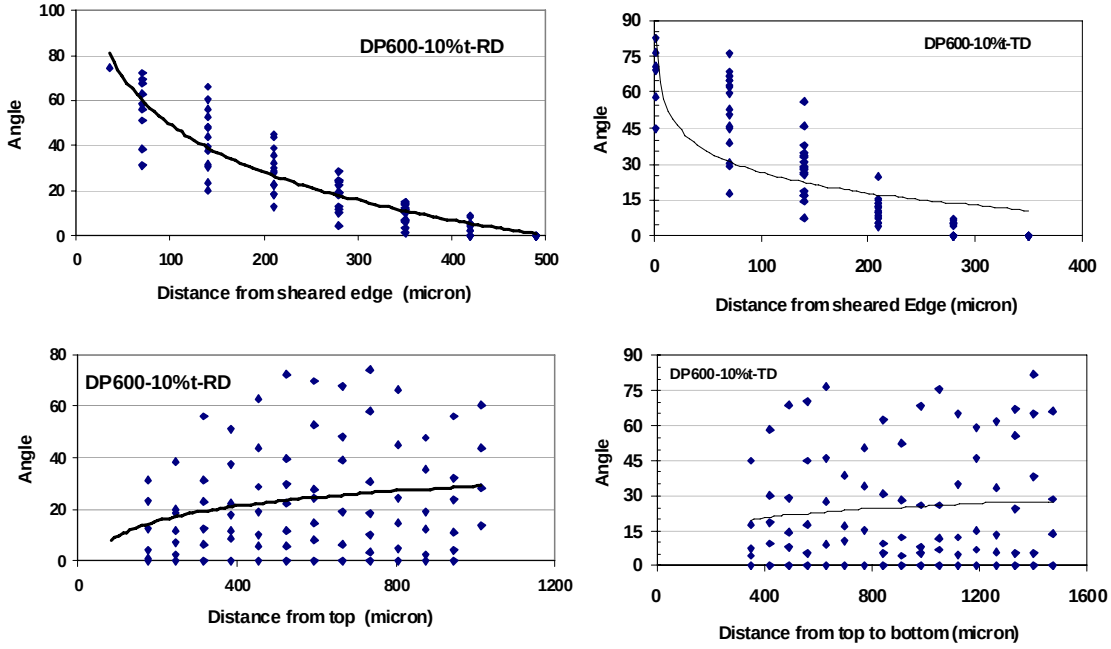

Figure 5.9. DP600, 10%t clearance. Measured angles distribution from edge to interior and from top to bottom of the thickness, in RD and TD sections, respectively[110].

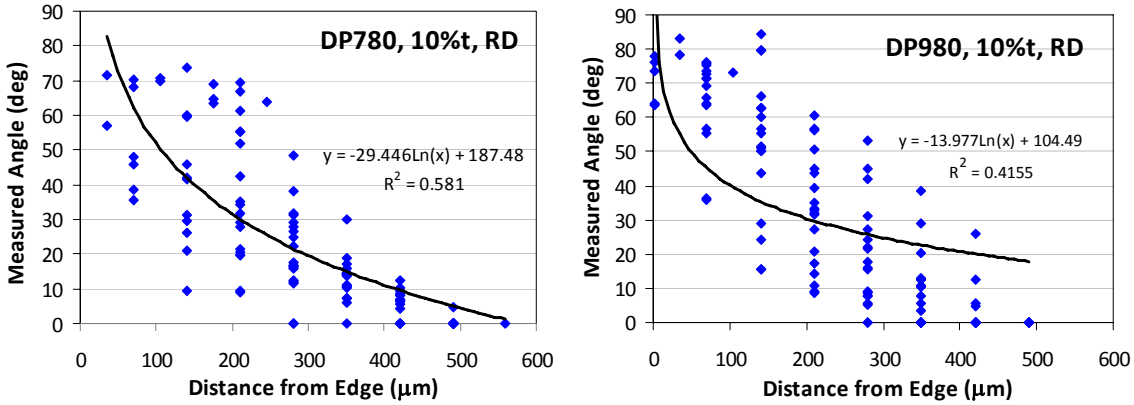

Figure 5.10. Measured angles distribution from edge to interior of DP780 and DP980 in RD, 10%t clearance[110].

5.3.2. Simulations of Shearing and Hole Expansion

In sheet metal forming, material is usually under plane stress deformation and an empirical equation, forming limit curve (FLC), is used as a failure criterion. To perform shearing simulation of AHSS, then carrying the results onto the subsequent forming simulations to predict formability is a very complex analysis task involving multiple loading patches and multiple forming stages. It faces some challenging issues:

(1) Failure criteria. Ductile fracture criteria are usually used for shearing analysis, but their applicability to AHSS needs to be validated. Furthermore, there are no sufficient data of material parameters available for validation of AHSS. The feasibility to incorporate the fracture limit into sheet forming limit criterion needs to be investigated.

(2) In shearing process, the strain state is either plane strain or axisymmetric, while most subsequent forming is in plane stress state. The loading path is also different from shearing to edge stretching. Three-dimensional analyses may be necessary for integrating these two analyses.

5.3.2.1. Failure criteria

Most of the previous simulation studies for shearing processes deal with lower strength metals, and ductile fracture criteria are used. The void initiation, growth and coalescence processes are considered and it is assumed that fracture occurs when the accumulated plastic strain energy reaches a limit C under a certain stress state [118]. The general form can be expressed as:

$$\int f(\sigma) d\varepsilon^p = C \qquad (5\text{-}1)$$

where $f(\sigma)$ is a function of stress tensor σ, and the integration is performed incrementally over plastic strain $d\varepsilon^p$ through the entire deformation history. C is a material constant and can be determined by experiments. Similar to the FLC, a fracture limit curve can be experimentally determined which is usually above the FLC when mapping to the principal strain plane. Tests under various loading conditions are required to create the fracture curve, which involves tremendous effort. Goijaerts [118] tried a simplified method to calibrate the material constant C using a tensile test, and satisfactory results were obtained for shearing simulations.

In current analyses, tensile tests of sheared edge specimens were used to validate and calibrate the fracture criteria for hole expansion because the strain path of edge stretching is similar, in a uniaxial tension mode. The Digital Image Correlation (DIC) technique was used to capture the localized fracture strain in the tensile tests. The measured true strains at fracture for DP780 and 590R steels are 0.16, 0.31 respectively based on the average of three repeated sample tests. Figure 5.11 shows tension test and simulation calibration of DP780 steel. The simulation used half width of the specimen due to symmetry. The simulation results were in good agreement with the test data.

For shearing simulation, MMC fracture criterion is used which was described in Chapter 4. In the calibration of the MMC criteria, a butterfly specimen was used. Various combination loading of normal (tension/compression) and shear force [74]. The tests cover a wide range of shear strain states including those that occurred in the shearing process, therefore this is an ideal test to calibrate the fracture in shearing processes.

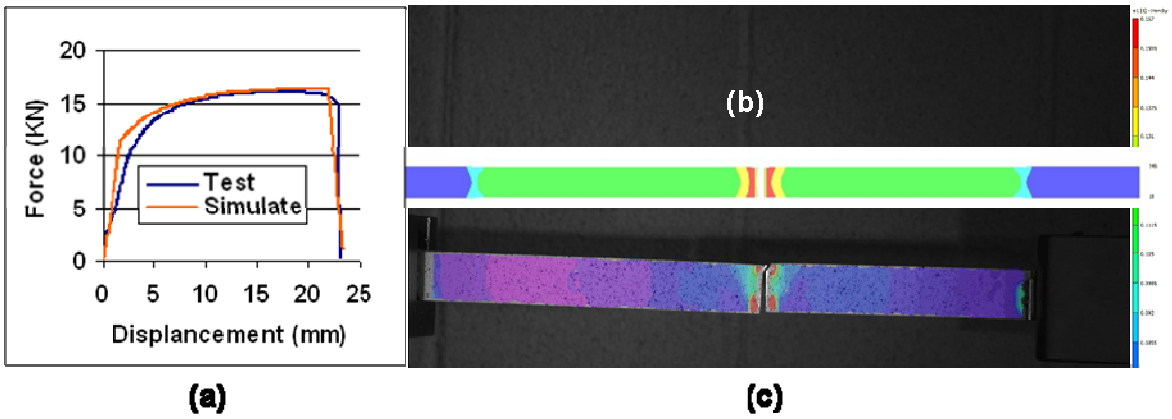

Figure 5.11. Calibration simulation using tensile test. (a) Calibration using tensile curve; (b) Simulated correlation; (c) Strain distribution before fracture measured by DIC.

5.3.2.2. Shearing/Piercing Simulation

Simulation of shearing process was carried out. Hill's 1948 yield criterion is used with an isotropic hardening rule. MMC ductile fracture criterion is used for fracture limit. The FE model is shown in Figure 5.12. Axisymmetric model is used to simulate the circular hole piecing process. Very fine elements (2μm side length) are generated in the shear affected zone and the element deleting technique is applied to simulate the development of fracture.

Figure 5.13 shows the simulation process. At the beginning of the piercing process plastic strain initiates around the tool corners. As the punch moves down, the plastic strain becomes higher and penetrates deeper through thickness direction, eventually fracture grows across the material thickness.

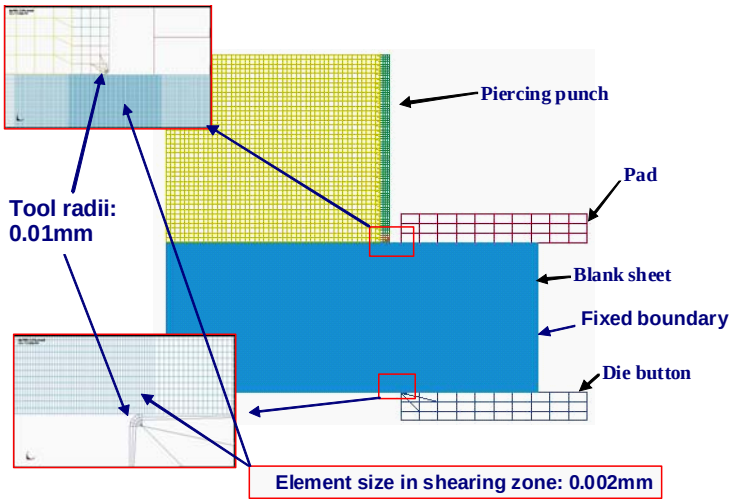

Figure 5.12. Hole piercing simulation model.

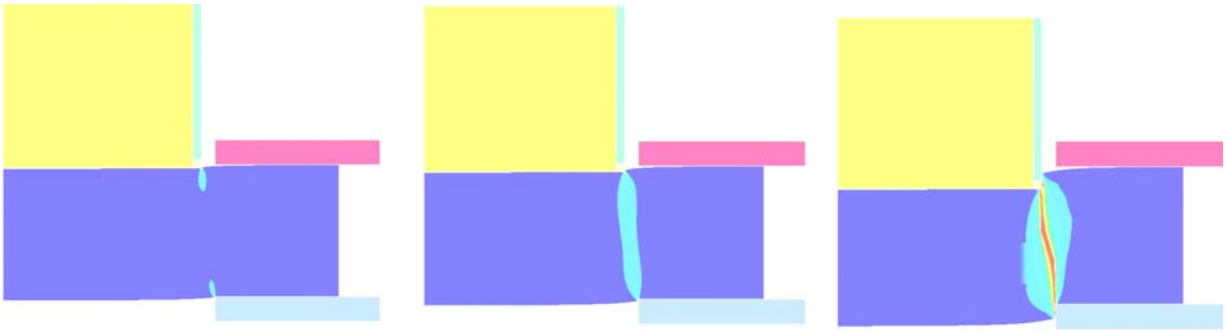

Figure 5.13. Hole piercing process in simulation.

Figure 5.14 shows a visual comparison of sheared edge shapes and tilting angle distributions between the tested sample and the FE simulation for DP600 with 10% die clearance. It is noted that the simulation result has the same trend as the test result. The shear strain decreases rapidly from the edge toward the inner materials. From top to bottom of the thickness, the highest strain peak appears close to mid-plane in the fracture zone, which is in agreement with the experimental result. The material flow angles from the simulation result are similar to the test data in the middle region, but under predicted

at the rollover zone. Similar comparisons for DP780 and DP980 are shown in Figures 5.15 and 5.16. The edge shape comparison has less significant meaning because the AHSS sheared edge shapes are not consistent. The tilting angle (shear strain) comparison provides another measurement of damage at the sheared edge. It is easier to be used in simulation compared to measuring hardness which is usually used in measurement of conventional steels.

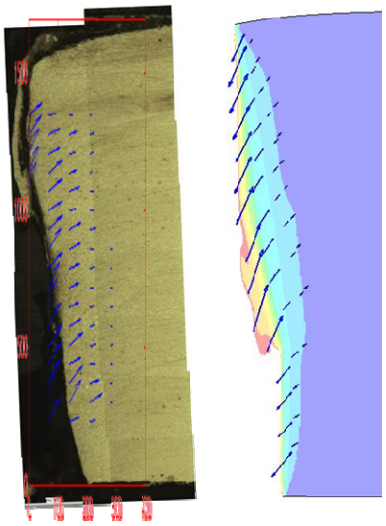

(a) (b)

Figure 5.14. Result comparison between measurement and simulation, for DP600. (a) Measured metal flow field with the arrows representing the measured tilting angle (shear strain); (b) Vector map from simulation.

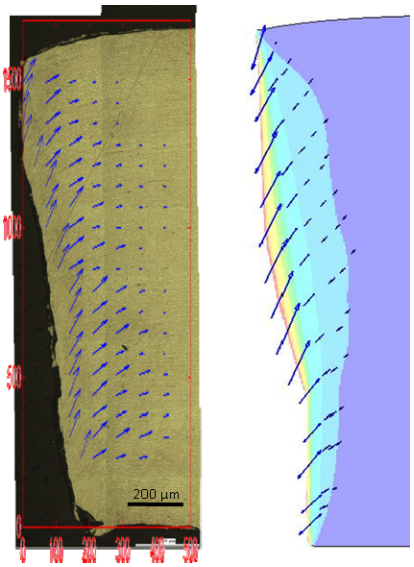

Figure 5.15. Result comparison for DP780

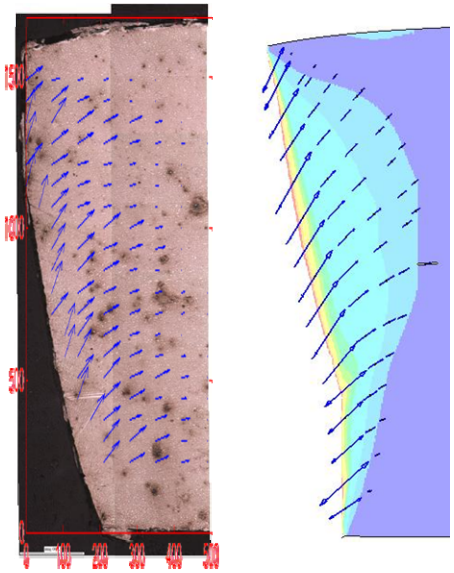

Figure 5.16. Result comparison for DP980

5.3.2.3. Hole Expansion Simulation

It can be seen from the above analysis that severe deformation occurs at the shear affected zone edge by the shearing process. The large plastic strain near the sheared edge due to the piercing process increases the tendency of edge fracture in the subsequent edge stretching process that reflects void growth and coalescence. To demonstrate this effect, a hole expansion simulation was conducted following the piercing process. The hole expansion of the laboratory test (see Figure 5.3) is used with DP780 steel. Figure 5.17 shows the simulation processes using an axisymmetrical model.

Figure 5.17(a) is the piercing simulation described in the previous section. Figure 5.17(b) shows the initial state of hole expansion where the deformation from the piercing process is included and the maximum true shear strain is 0.7. Figure 5.17(c) shows the final stage of hole expansion when the measured hole expansion ratio of 24.8% was used.

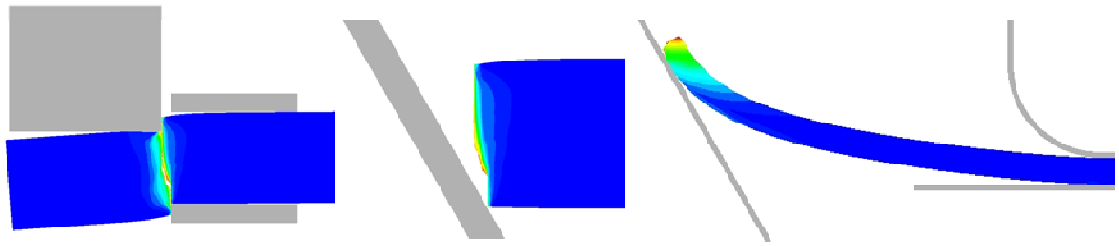

(a) (b) (c)

Figure 5.17. Hole expansion simulation processes (a) Piercing simulation, (b) Initial state of hole expansion, (c) Final stage of hole expansion.

In this example, results of hole expansions are compared between simulations with and without the inclusion of deformation from the piercing simulation. Two points are selected for comparison, one on top and the other is at 0.4 mm from the top (Mid position). Figure 5.18 shows the comparisons for all plastic strain components in the radial, hoop and thickness directions within the (x, y, z) sheet coordinate system, respectively, and for the effective plastic strains E_{eff}. The strains are significantly higher when including the piercing deformation history in the hole expansion simulation. Without piercing pre-strain, the strains of hole expansion start from zero and steadily increase, with the hoop strain (Ey) in tension, thickness strain (Ez) in compression and limited shear strain (Exz). The strain state is similar to that in uniaxial tension along the hoop direction due to its free surface condition in both the radial and thickness directions. Upon fracture, the total edge strains at Top- and Mid-positions are 0.40 and 0.37, respectively, when the total punch travel reaches that in the experiment, at which the first through-thickness was observed. On the other hand, when the pre-strain from piercing is included, the continued strain evolution in hole expansion shows a steady increase in

radial strain (Ex), reduction in thickness strain (Ez), and a complex evolution of shear strain (Exz) that initially increases and then decreases, with the change being more significant for the Top point than for the Mid point, probably due to the roll-over zone effect. In all, this strain evolution reflects changes of strain paths from piercing to hole expansion. Interestingly, the hoop strain, which was almost zero during piercing, increases almost following the same evolution process as that without considering piercing. The effect of shearing can also be reflected by the damage factor. Figure 5.19 shows the damage when using MMC criterion to evaluate fracture. It can be seen that the damage factor D is significantly higher when including piercing effect.

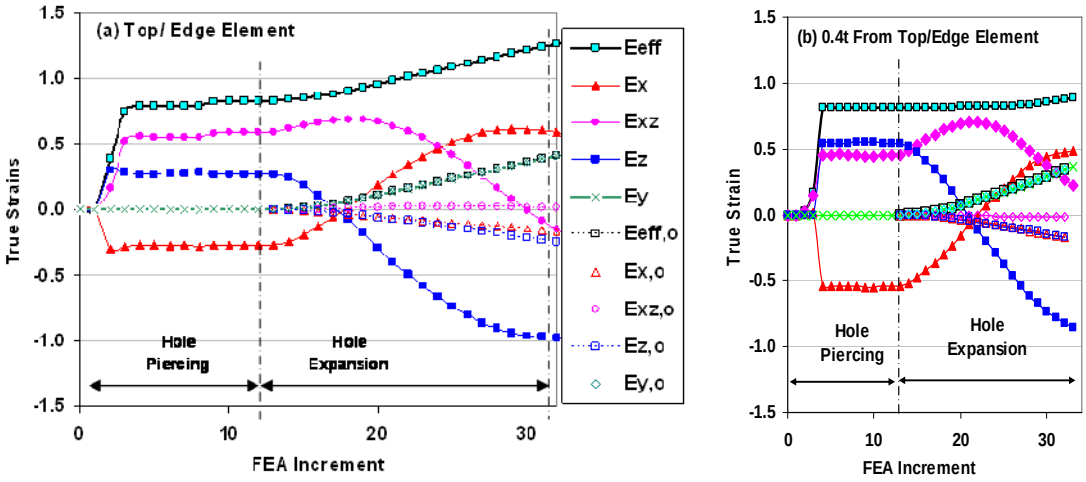

Figure 5.18. Comparison of plastic strain development in hole expansion with and without considering pre-strain from piercing, for two edge height positions at the very top (a) and at 40% thickness from the top (b). (x, y, z) denote radial, hoop and thickness directions in sample coordinate, respectively; E_{eff} is the effective plastic strain, and "o" denotes the hole expansion without pre-strain from piercing.

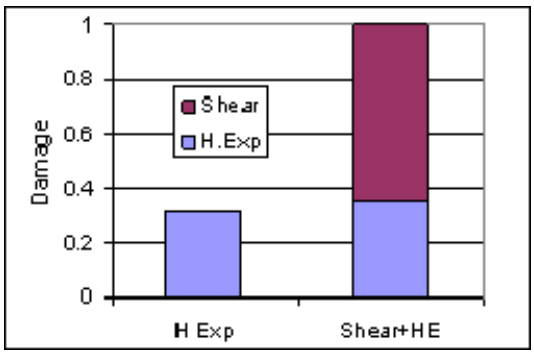

Figure 5.19. The damage factor is significantly higher when including shearing effect.

5.4. PRE-FORMING EFFECT ON AHSS EDGE CRACKING

It is observed in production that pre-forming does not always improve AHSS edge stretchability. To better understand the pre-forming effect, experiments were designed to test the pre-forming and stretching of two AHSS, DP780 and 590R. Their properties are shown in Table 5.1. Simulation technology was also developed to analyze those processes and compare with the experimental data.

5.4.1. Experiments of Pre-forming and Stretching

The strain state of edge stretch is in uniaxial tension state, therefore it can be experimentally simulated by a tensile test. Figure 5.20 shows the tool used for pre-forming. Using this tool, a pre-formed wave can be created from a straight steel strip. Both one and two waves were made. Three different radii and various pre-form depths can be selected. Some pre-form specimens are shown in Figure 5.21.

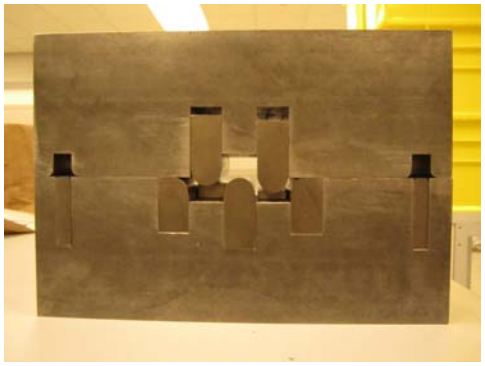

Figure 5.20. Tools for pre-forming

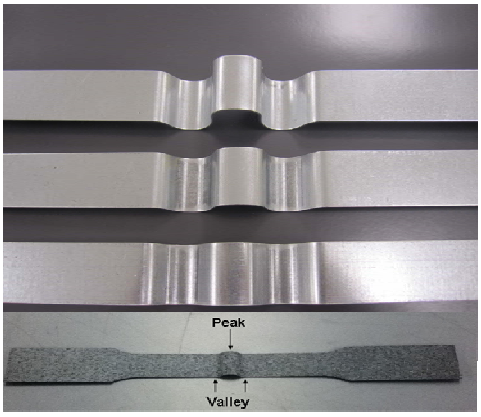

Figure 5.21. Pre-formed strip

A pre-formed strip was then pulled in a tension test machine as shown in Figure 5.22. Pulling stopped when fracture occurred. Figure 5.23 shows a force-displacement curve for DP780 steel. This experiment was designed to use DIC for strain measurement. The steel samples were sprayed with paint to make a speckle surface for DIC strain measurements.

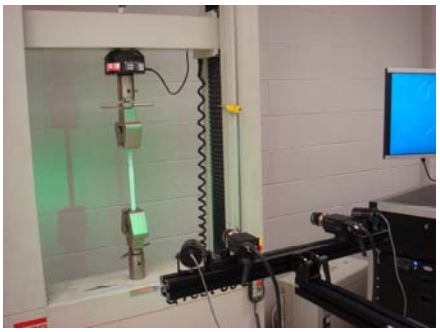

Figure 5.22. Stretching of pre-formed strip.

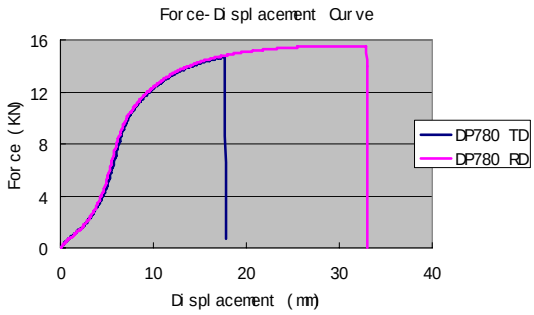

Figure 5.23. Force-displacement curves.

5.4.1.1 Strain Distributions

The strain distributions were measured using DIC technology. Figure 5.24 shows the color maps of true major and minor strain distributions on the top surface of a pre-

formed sample. The maximum strain is about 7% on the peak of the pre-form. Figures 5.25 and 5.26 show the distributions of strains at fracture for DP780 and 590R, respectively. It can be seen that the DIC technique can obtain the strain distributions clearly and capture the strains at fracture.

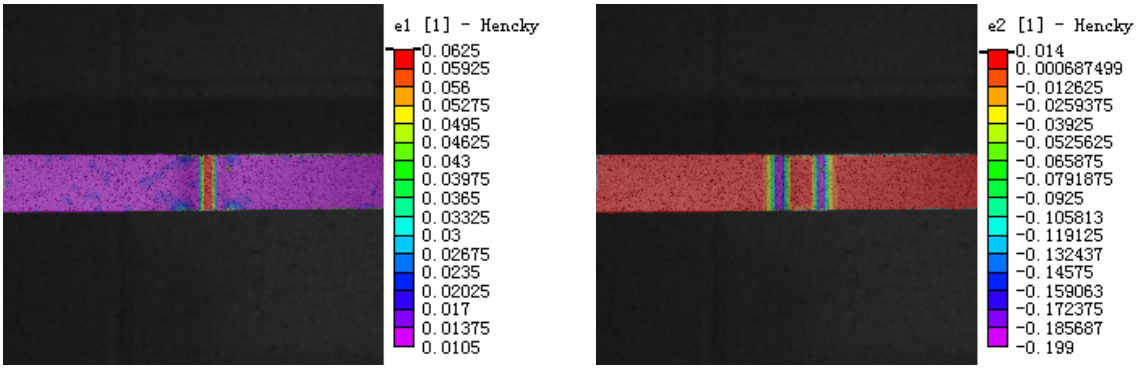

(a) (b)

Figure 5.24. Major (a) and minor (b) strain distributions on a pre-formed sample of DP780.

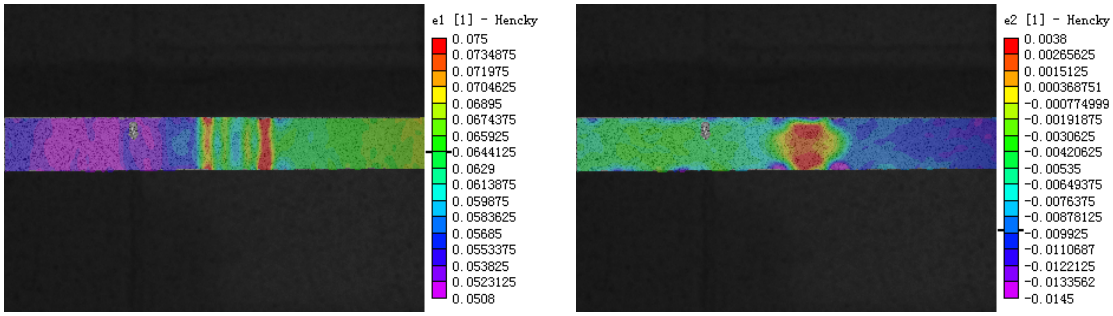

(a) (b)

Figure 5.25. Major (a) and minor (b) strain distributions at fracture (DP780 transverse)

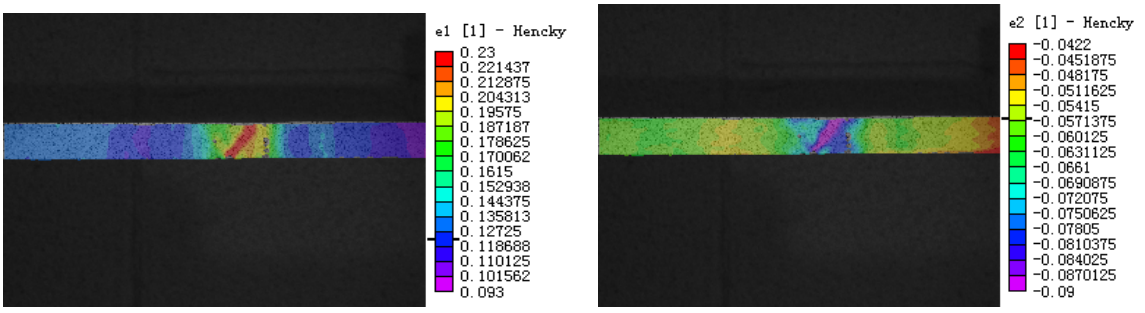

(a) (b)

Figure 5.26. Major (a) and minor (b) strain distributions at fracture (590R transverse)

Another advantage of using DIC is that the deformation history can be recorded, which provides very useful information for multi-stage forming analyses as in the current case. The above strain mapping figures show that the major and minor strain distributions are reasonably uniform along the width of the specimens. Therefore, the deformation history along the width can be represented in one section. Figures 5.27 to 5.30 show the major strains along the longitudinal direction of the specimens. Strains are measured on the top surfaces at various steps. The first step is pre-forming, in which bending is the dominant deformation. Tension is seen at the peak and compression at the valleys near the peak. The specimen is then stretched in the tension machine. As the specimen is stretching, unbending occurs at the pre-formed region and tension strain is increasing along the whole specimen. For the specimens in the transverse direction, strains reach the failure limit and fracture occurs in the pre-formed regions as shown in Figures 5.27 and 5.28 for DP780 and 590R steels, respectively. In the specimens tested in the rolling direction, fracture occurs outside the pre-formed regions and fracture strains are significantly higher as shown in Figures 5.29 and 5.30 for DP780 and 590R steels, respectively.

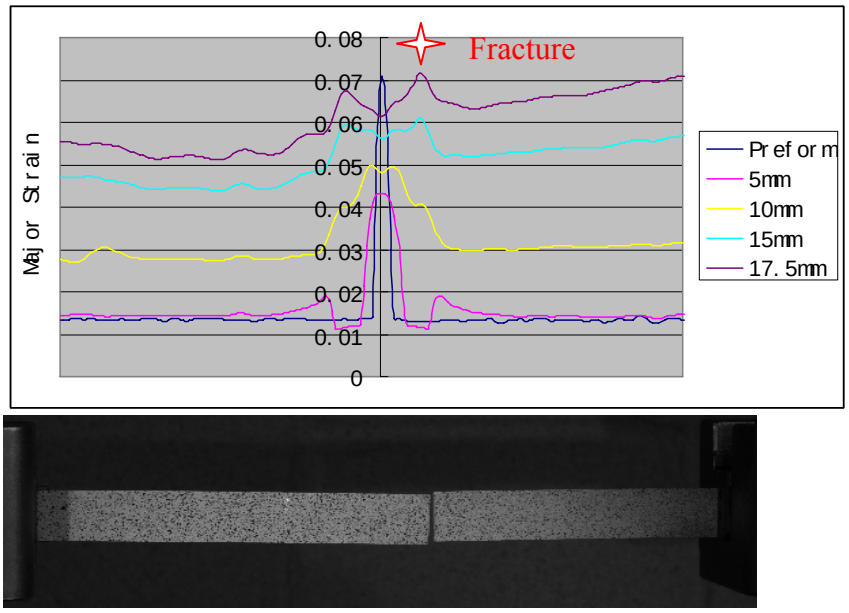

Figure 5.27. Major strain of DP780 along transverse direction.

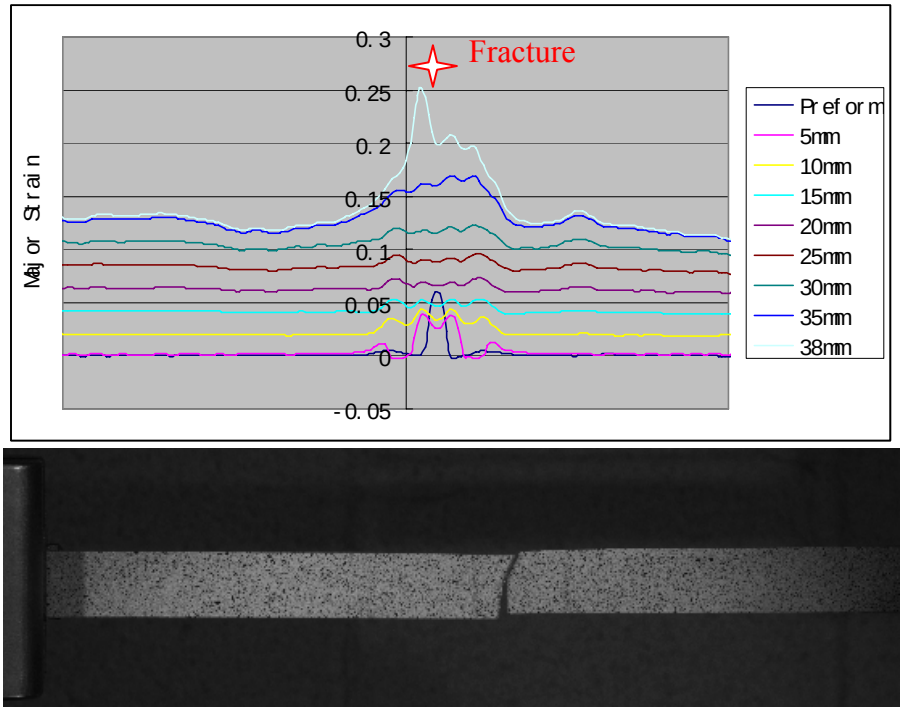

Figure 5.28. Major strain of 590R in transverse direction

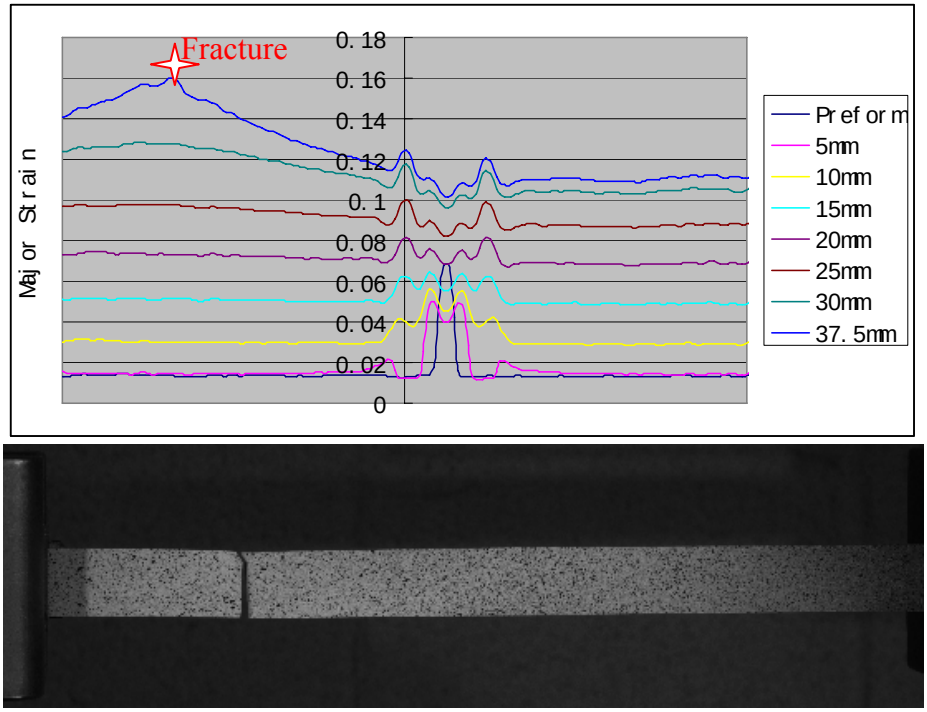

Figure 5.29. Major strain of DP780 in the rolling direction.

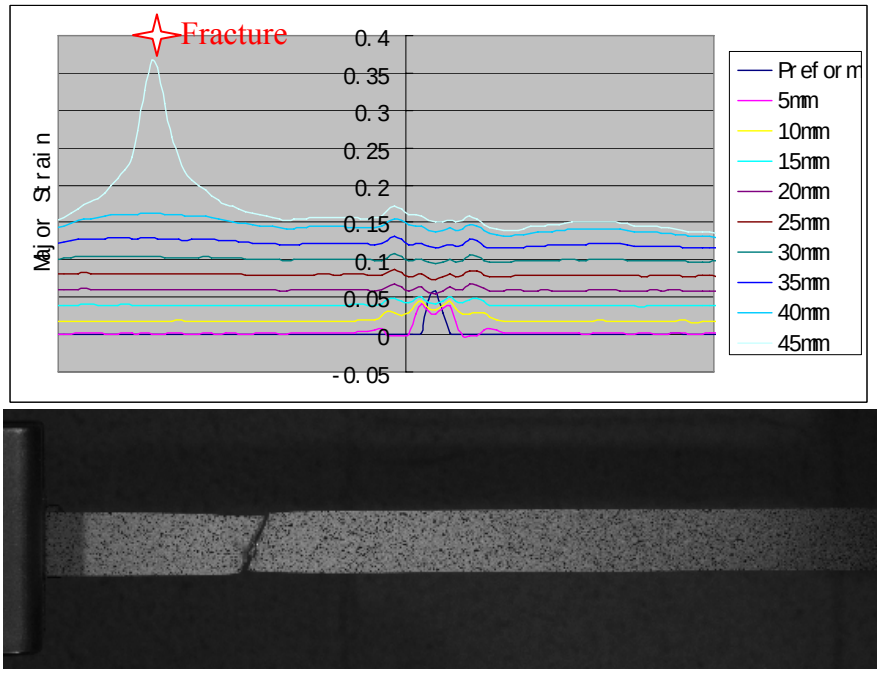

Figure 5.30. Major strain of 590R in the rolling direction.

5.4.1.2. Fracture

Three types of tensile failures were observed in the tests. Figure 5.31 shows those for DP780 steel. Type A is a milled edge without machining damage at the edge. Fracture initiated from the center of a specimen. Thinning and necking are observed. Type B is a sheared edge. Minor necking and thinning are observed around the fracture. In Type C, a sheared edge specimen is pre-formed then pulled. Fracture occurs at the pre-formed region. Fracture initiates at the edge and shear fracture is observed with minimum thinning and necking. Figure 5.32 is the comparison of the fracture strains for the three types. There is a critical strain value for sheared edge pre-forming and stretching. If a material does not fracture at this value, failure will occur outside the pre-formed region, and the failure strain will be significantly higher. This critical strain value depends on the pre-forming geometry, edge damage severity, steel grade and material orientation.

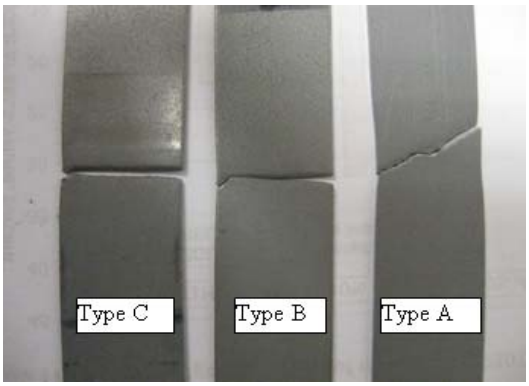

Figure 5.31. Three types of fractures of DP780.

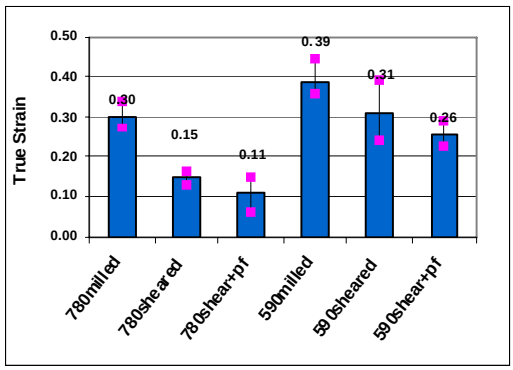

Figure 5.32. Comparison of the fracture strain for three types.

5.4.2. Simulation

5.4.2.1. Simulation Model and Setup

Finite element analyses were conducted to simulate the pre-forming and stretching tests. Figure 5.33 shows the model. Full integration shell elements and solid elements were respectively used and run on Software packages of LS-Dyna and ABAQUS. Only half of the blank width was used due to the symmetry. An initial simulation using conventional setup for forming simulation was conducted. The result does not agree well with the testing data. Therefore, a systematic simulation study was conducted with various simulation variables, including three yield criteria (von Mises, Hill's 1948 and Barlat), isotropic and isotropic/kinematic hardening rules, implicit and explicit solvers.

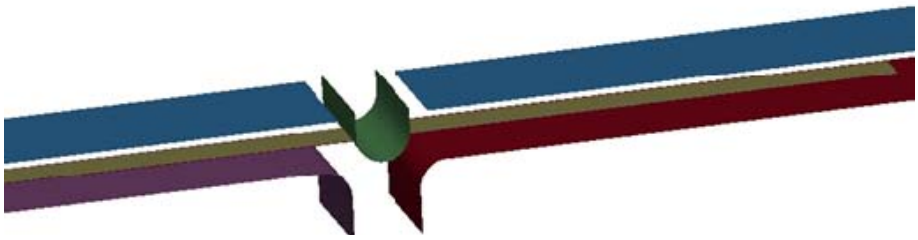

Figure 5.33. Finite element model for simulation

5.4.2.2. Variable Study and Results Comparison

Strain distribution is usually used to evaluate the forming process, therefore strain history is used for result comparison in this study. Strain along the longitudinal direction

(Exx) is used for result comparison. There is no significant difference in the results when using various yield criteria. Therefore, only Hill's yield criterion was used in the later simulation.

Figure 5.34 shows the Exx of pre-forming for simulation of various combinations of simulation variables. It can be seen that there is no significant difference for all the results. Figure 5.35 shows the Exx history of pre-forming and stretching using isotropic hardening and explicit solver. The X axis is the length in the longitudinal direction of specimen and Y axis is Exx in different time step. From bottom to top, the first line is Exx for pre-forming, 2^{nd} to 4^{th} lines are Exx corresponding to 3%, 6%, 9% and 12% stretch respectively. We can see that as the specimen is stretching, unbending occurs at the pre-formed region and tension strain is increasing. However, in the pre-form region, the maximum Exx reaches about 0.08 and does not increase further even when the pulling force increases. The high strains spread out of the pre-form region. The 0.8 maximum strain is lower than the fracture strain measured in the experiment and the simulation can not predict the fracture in this case. Figure 5.36 shows the Exx history of pre-forming and stretching using isotropic hardening and implicit solver. Figure 5.37 shows the Exx history using isotropic/kinematic hardening and explicit solver. Similarly these two combinations also under predict the strains in the pre-formed region.

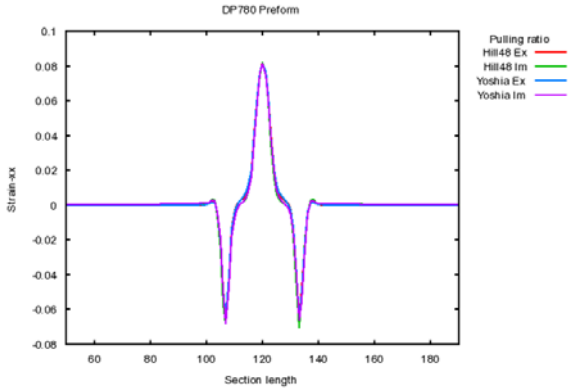

Figure 5.34. Exx of pre-forming for various simulation combinations.

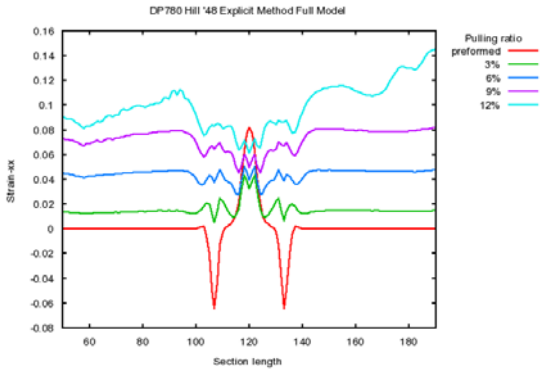

Figure 5.35. Exx history using isotropic hardening and explicit solver

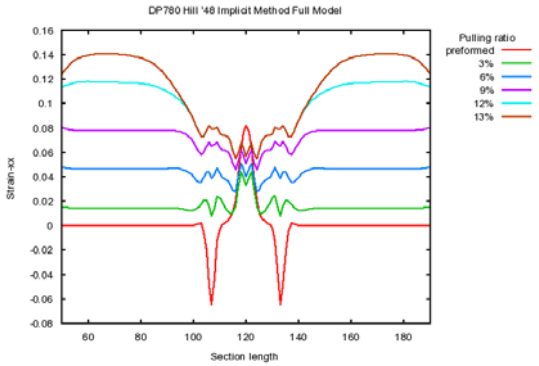

Figure 5.36. Exx history using isotropic hardening and implicit solver

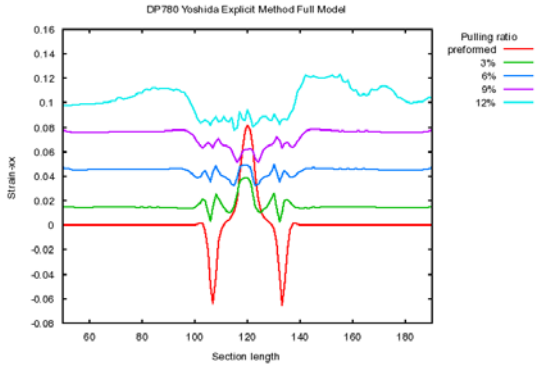

Figure 5.37. Exx history using kinematic hardening and explicit solver

Figure 5.38 shows the Exx history of pre-forming and stretching using isotropic/kinematic hardening and implicit solver. This is the only combination which can predict the fracture strain in the pre-formed region. When using the implicit for this analysis, the selection of incremental time step is important. Time steps that are too small induce a high cost in computational time. Time steps that are too large may cause the computation to miss some critical deformation points and the will under-predict the

bending/unbending strains. Figure 5.39 and Figure 5.40 shows the Exx comparison of simulation with experimental results for DP780 and 590R, respectively. The simulations used isotropic/kinematic hardening and implicit solver.

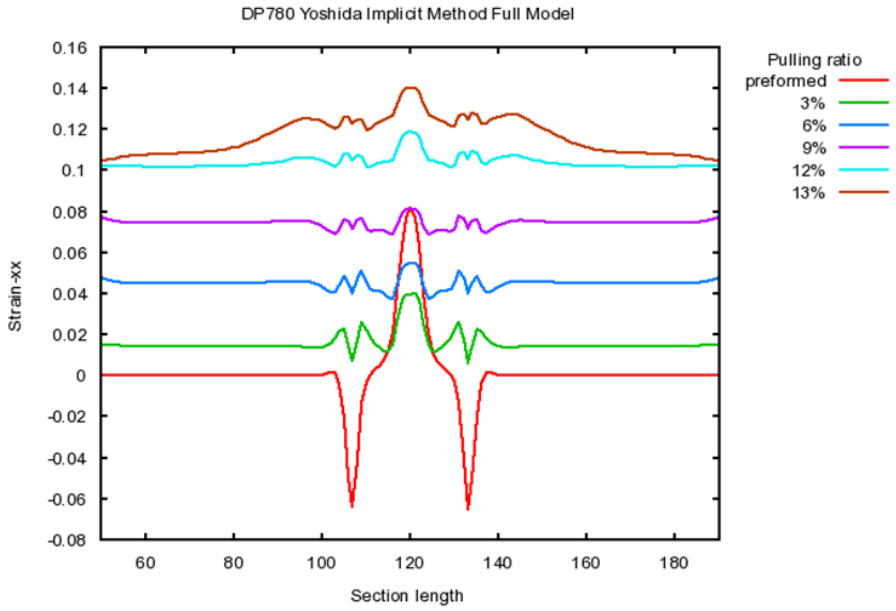

Figure 5.38. Exx history using isotropic/kinematic hardening and implicit solver.

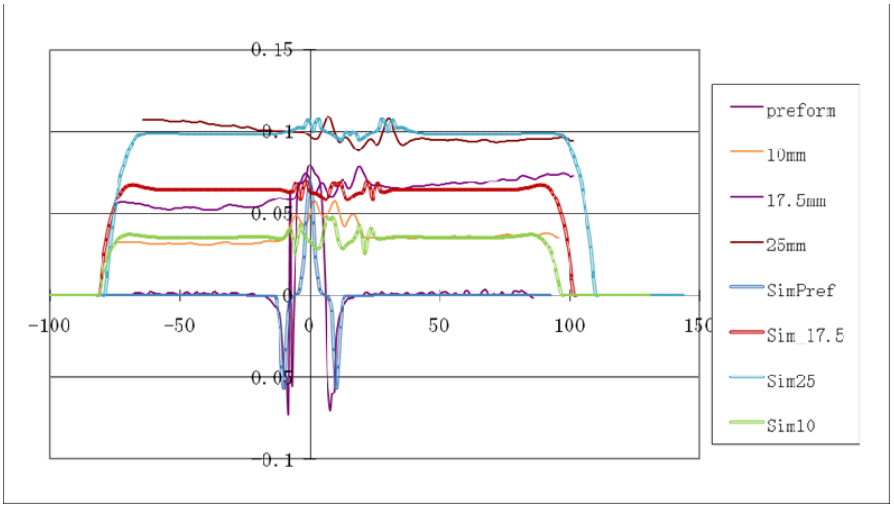

Figure 5.39. Exx comparison of simulation with experimental result for DP780.

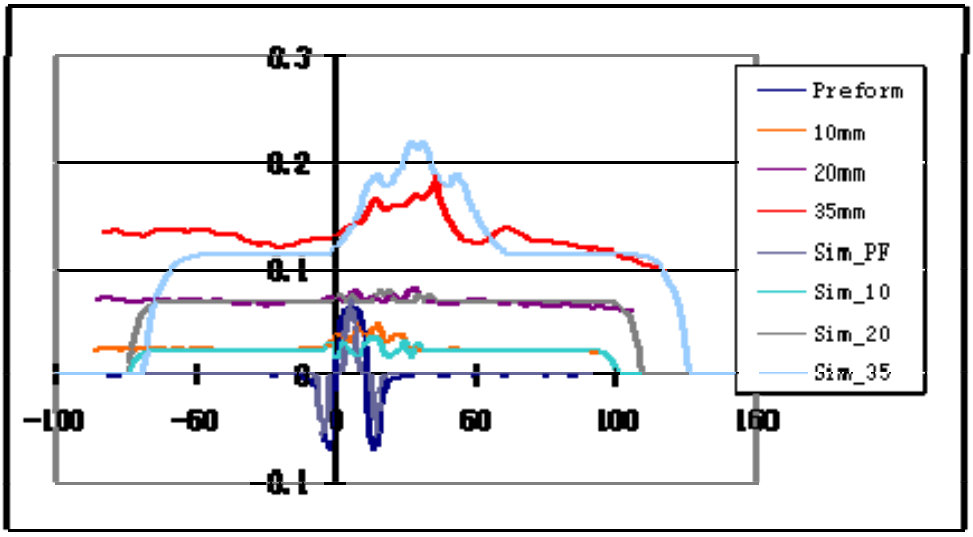

Figure 5.40. Exx comparison of simulation with experimental result for 590R.

5.4.2.3. Forming Limit

Figure 5.41 shows the forming limit diagram (FLD) strain distribution on the major-minor strain plane when fracture initiates. It can be seen that all strain points at the edge are along the uniaxial tension line and far below the FLC. This indicates that the conventional FLC can not be used to predict AHSS edge cracking.

The comparison of different forming limits and strain paths is shown in Figure 5.42. The strain paths at four different locations are shown in the figure. The edge point at the peak (EP) of the pre-forming moves up and down along the uniaxial tension path during bending and unbending. The edge point at the valley (EV) moves along the uniaxial compression line. The center point at the peak (CP) is in plane strain condition

and moves along the major strain axis. The center point at the valley (CV) moves along the minor strain axis. The FLC is drawn based on the sheet thickness and n value. It lies far above the failure strain point. The milled edge failure is shown in a horizontal line at 0.3 major strain. It is close to the intersection of the FLD and the uniaxial tension line. The sheared edge failure line is at 0.15 major strain. The failure strain of a sheared edge with pre-forming is at 0.11 major strain. This line can be used to predict failure in this case.

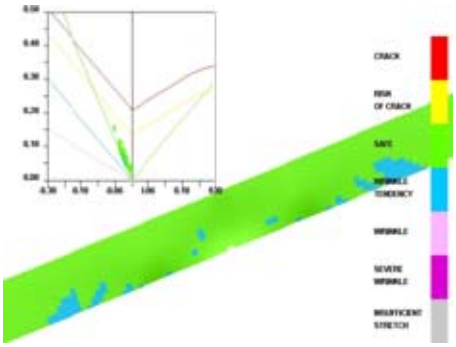

Figure 5.41. FLD strain mapping at fracture initiation.

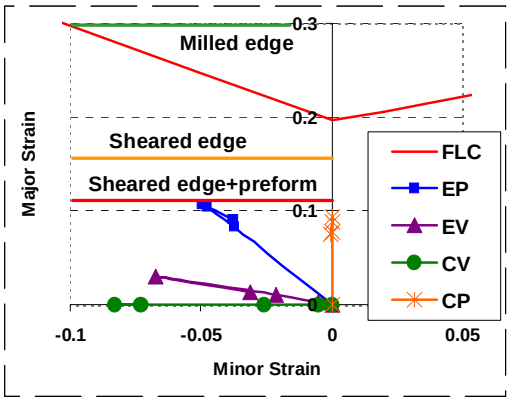

Figure 5.42. Comparison of different forming limits and strain paths.

5.5. CASE STUDY

A case study is given in this section to demonstrate the application of the studies in the previous sections. The case is flanging of a DP780 reinforcement part, as shown in Figure 5.43. The part was stamped using pre-forming followed by trimming and flanging operations. The hole expansion ratio measured from the conical punch hole expansion test is about 15% for this material, as shown in Table 5.1.

As shown in Figure 5.1 in Section 5.1., the maximum principal strain near the edges is about 22% from the pre-forming stage, which is below the forming limit but exceeds the stretch flangeability limit. This is confirmed in the actual stamping trials and the cracking locations which match the computer simulation predicted locations. It can be seen that a scallop type pre-form is not suitable for this case. The pre-form shape needs to be modified so that the edge to be flanged undergoes minimal or no deformation during the pre-forming stage. The modified pre-form shape is shown in Figure 5.44 and the maximum major strain is reduced to 10% at the free edges after the flanging operation, which is below the stretch flangeability limit. As a result, the part was successfully stamped without any edge cracking.

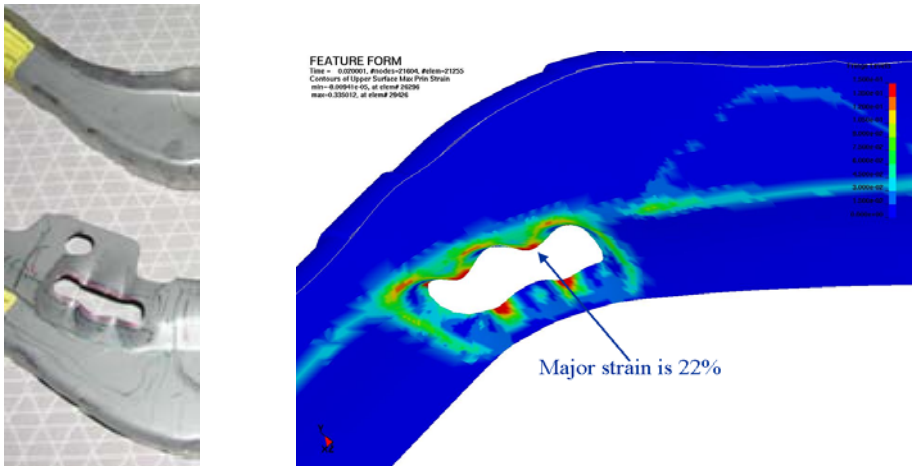

(a) (b)

Figure 5.43. Part of case study, (a) Pre-form and flange, (b) Principal strain after pre-forming (Major strain = 22%).

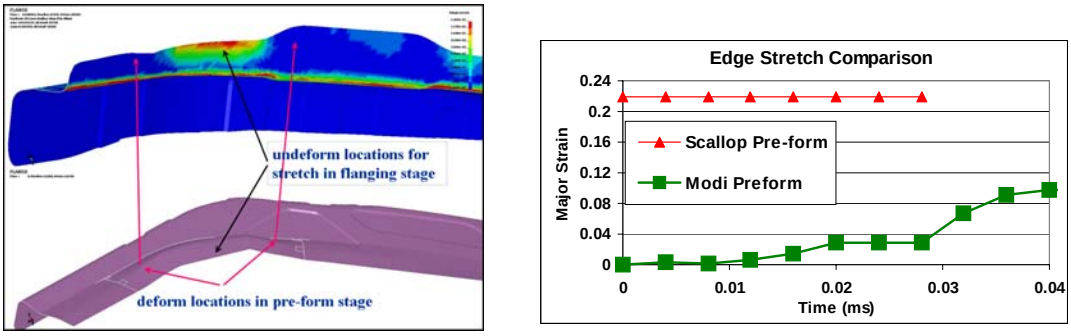

(a) (b)

Figure 5.44. (a) Modified pre-form shape (b) Maximum principal strain is reduced to 10%.

5.6. CONCLUSIONS

Conclusions can be drawn from the studies of this chapter:

- AHSS sheared edge shape is less regular and the four zone feature is not consistent. An alternative sheared edge quality evaluation method by measuring flow line angle change is presented, which is a more reliable approach to represent edge shear deformation of AHSS.
- MMC failure criteria can be used in shearing simulations. Simulation results agree well with experimental data.
- When the shearing deformation is included in the hole expansion simulation, the equivalent plastic strain or edge damage is significantly higher, therefore the shearing deformation must be included in hole-expansion simulation for correct prediction.

- Pre-forming is important in the prevention of edge cracking of AHSS in flanging and edge stretching processes. The conventional approach needs to be modified to be used for AHSS pre-forming.
- Surface strain distributions of experimental pre-forming and stretching can be measured with DIC technique, which provides full field and history of strain distributions.
- There is a critical strain value for pre-forming and edge stretching which is a boundary of failure occurring in or out of the pre-formed region. This strain value depends on the pre-formed geometry, edge damage severity, steel grade and material orientation.
- The conventional FLD cannot be used to predict edge failure in pre-forming and post stretching since the failure limit is much lower due to sheared edge and stretch bending deterioration. The limit strain can be measured with the pre-form and stretch testing.
- Simulation technologies have been developed to predict the bending and unbending strains of pre-forming and subsequent stretching which uses implicit solver with isotropic/kinematic hardening model. A computer assisted technology is important for optimal designs of pre-forming.

CHAPTER 6. SIMPLIFIED METHODS

6.1 INTRODUCTION

As it can be seen in the previous chapters, FEA is a powerful numerical technique for metal forming simulation. It has the capability of handling very general geometries, different deformation models and material behaviours, and integrating various failure criteria. However, some disadvantages are also seen as it is time consuming and requires high computational cost. The preparation (pre-processing) is complicated work and requires special training. It requires extensive work on parametric study to obtain a proper setup to avoid numerical errors. Therefore simplified analysis approaches are more favourable in some specific applications which can analyse problems faster and more accurately. Some simplified methods provide quick solutions to specific problems or a particular location within the component.

In this chapter, simplified numerical methods are developed to handle plane stress and plane strain problems in forming processes. The flange region during the deep drawing of prismatic cups has been analysed using several different numerical methods. The intention is to provide deformation information and to produce optimal blank shapes with minimum computational effort. The first one is the plane stress characteristics (PSC) method. The PSC formulation of planar anisotropy by including the r value has been developed and the characteristics of stress and velocity coincidence were established. An application example is to develop optimal (or near-net shape) shaped blanks when deep drawing prismatic cups. Another method is the plane strain slip line field (SLF) analysis. A quick-run program was developed for blank development and flange deformation analysis.

An application example was used to show the earing development for the entire process of circular cup drawing.

6.2 THE METHOD OF PLANE STRESS CHARACTERISTICS

The PSC method is based on plane stress formulation and thickness changes in the flange can be analyzed. The technique is described in some detail in the book by Szczepinski [150]. The current study improves that by Szczepinski by incorporating anisotropy into the solution, assuming the material is planar isotropic, and was able to establish that the characteristics of stress and velocity coincided. The derivation is given herein:

6.2.1. Formulation

Hill's anisotropic yield function for a normal anisotropic solid, under the conditions of plane stress is [144]

$$(1+r)\,(\sigma_{xx}+\sigma_{yy})-2\,r\sigma_{xx}\,\sigma_{yy}+(2+4r)+\sigma_{yy}=(1+r)\,Y \qquad (6\text{-}1)$$

where Y is the uniaxial yield strength of the material in the x-y plane. Upon applying the flow rule to (6-1), it follows that the components of the rate of deformation tensor are,

$$d\varepsilon_{xx}=\frac{\partial Vx}{\partial x}=2d\lambda\,[(1+r)\,\sigma_{xx}-r\,\sigma_{yy}]$$

$$d\varepsilon_{yy}=\frac{\partial Vy}{\partial y}=2d\lambda\,[(1+r)\,\sigma_{yy}-r\,\sigma_{xx}]$$

$$d\varepsilon_{xy}=d\varepsilon_{yx}=\frac{1}{2}\left(\frac{\partial Vx}{\partial y}+\frac{\partial Vy}{\partial x}\right)=2d\lambda\,(1+2r)\,\sigma_{xy} \qquad (6\text{-}2)$$

In the above dλ is a proportionality factor and V x and V y the in-plane components of velocity. Equations (6-2) can also be expressed as

$$\frac{\partial Vx/\partial x}{(1+\mathrm{r})\,\sigma_{xx} - \mathrm{r}\sigma_{yy}} = \frac{\partial Vy/\partial y}{(1+\mathrm{r})\,\sigma_{yy} - \mathrm{r}\sigma_{xxx}} = \frac{\partial Vx/\partial y + \partial Vy/\partial x}{(2+4\mathrm{r})\,\sigma_{xy}} = 2d\lambda \qquad (6\text{-}3)$$

From (6-3) it follows that

$$(1+\mathrm{r})\,\sigma_{yy} - \mathrm{r}\sigma_{xx}\,\partial Vx/\partial x - [(1+\mathrm{r})\,\sigma_{xx} - \mathrm{r}\,\sigma_{yy})]\,\partial Vy/\partial y = 0$$

$$(2+4\mathrm{r})\,\sigma_{xx}\,\partial Vx/\partial x - [(1+\mathrm{r})\,\sigma_{xx} - \mathrm{r}\,\sigma_{yy})]\,(\partial Vx/\partial y + \partial Vy/\partial x) = 0 \qquad (6\text{-}4)$$

The above equations can be supplemented with the following relationships

$$\begin{aligned} (\frac{\partial Vx}{\partial x})dx + (\frac{\partial Vx}{\partial y})dy &= dVx \\ (\frac{\partial Vy}{\partial x})dx + (\frac{\partial Vy}{\partial y})dy &= dVy \end{aligned} \qquad (6\text{-}5)$$

Together equations (6-4) and (6-5) are hyperbolic and can be solved by the method of characteristics [150]. By setting the determinant of the coefficients of the partial derivatives of Vx and Vy to zero, the characteristic slopes are found to be

$$\frac{dy}{dx} = \frac{(1+2\mathrm{r})\,\sigma_{xy} \pm \{[(1+2\mathrm{r})\,\sigma_{xy}]^2 - [(1+\mathrm{r})\,\sigma_{yy} - r\sigma_{xx}][1+\mathrm{r}\,\sigma_{xx} - \mathrm{r}\,\sigma_{yy}]^2\}}{\mathrm{r}\sigma_{xx} - (1+\mathrm{r})\,\sigma_{yy}} \qquad (6\text{-}6)$$

It is convenient to express the stress components in terms of two parameters φ and ω where,

$$\sigma_{xx} = Y(\frac{1+\mathrm{r}}{2})^{1/2}\cos\omega + Y(\frac{1+\mathrm{r}}{2+4r})^{1/2}\sin\omega\cos 2\varphi$$

$$\sigma_{yy} = Y(\frac{1+\mathrm{r}}{2})^{1/2}\cos\omega - Y(\frac{1+\mathrm{r}}{2+4r})^{1/2}\sin\omega\cos 2\varphi$$

$$\sigma_{xy} = Y(\frac{1+\mathrm{r}}{2+4r})^{1/2}\sin\omega\cos 2\varphi \qquad (6\text{-}7)$$

The above expressions satisfy the yield criterion (6-1) and φ and ω are defined as

$$\cos\omega = (\sigma_{xx} + \sigma_{yy})/[Y(2+2r)^{1/2}]$$

$$\tan 2\varphi = 2\sigma_{xy}/(\sigma_{xx} - \sigma_{yy}) \qquad (6\text{-}8)$$

Upon substituting (6-7) into (6-6) there results the following expression for the slopes of the velocity characteristics

$$\frac{dy}{dx} = \frac{R\sin\omega\sin 2\varphi \pm [R^2 - (R^2+1)\cos^2\omega]^{1/2}}{R\sin\omega\cos 2\varphi - \cos\omega} \qquad (6\text{-}9)$$

In the above, the plus and minus signs refer to the slopes of the α and β characteristics respectively, while $R = (1+2r)^{1/2}$. The ordinary differential equations for velocity that must be satisfied along these characteristics can be shown to equal

$$dV_x/dV_y = -\,dy/dx \qquad (6\text{-}10)$$

For the isotropic case the characteristics of stress and velocity coincide and the slopes of the characteristics are given by

$$\frac{dy}{dx} = \frac{\sqrt{3}\sin\omega\sin 2\varphi \pm \sqrt{3 - 4\cos^2\omega}}{\sqrt{3}\sin\omega\sin 2\varphi - \cos\omega} \qquad (6\text{-}11)$$

The plus sign refers to the α-characteristics and the negative sign to the β-characteristics. The differential relations that must be satisfied along these characteristics are,

$$2\left(d\varphi \pm \frac{\sqrt{3 - 4\cos^2\omega}}{2\sin\omega} d\omega \right)$$

$$= \left((1 - \sqrt{3}\cot\omega\cos 2\varphi)\frac{\partial \ln h}{\partial y} + \sqrt{3}\cot\omega\sin 2\varphi \frac{\partial \ln h}{\partial x} \right) dx \qquad (6\text{-}12)$$

$$- \left(\sqrt{3}\cot\omega\sin 2\varphi \frac{\partial \ln h}{\partial y} + (1 + \sqrt{3}\cot\omega\cos 2\varphi)\frac{\partial \ln h}{\partial x} \right) dy$$

In the above equations, h is the thickness of the material, φ is the anticlockwise rotation from the x-axis to the maximum algebraic principal stress and ω is a parameter which bears the following relationship to the in-plane principal stresses,

$$(\sigma_{11}+\sigma_{22})=2\sqrt{3}\ 2\ k\cos\omega \ \text{ and } \ (\sigma_{11}-\sigma_{22})=2k\sin\omega \qquad (6\text{-}13)$$

The differential relationship that must be satisfied for the x and y velocity components along the characteristics is,

$$dV_x/dV_y = -\,dy/dx \qquad (6\text{-}14)$$

6.2.2. Deep Drawing: An Analysis of the Deformation in the Flange

Deformation in the flange of a cup during deep drawing is analyzed using the above equations. The material is assumed to be planar isotropic and to work harden isotropically. For unsteady state problems (like deep drawing), the network of characteristics has to be continuously regenerated due to the change in geometry of the outside edge of the blank. In the deep drawing problem the outer edge of the blank is stress free, and hence the quantities ω and **φ** are known around the perimeter. For an initially circular blank, the characteristics can be extended inward to meet the inside

boundary which is defined by the shape of the die cavity. The calculations are performed using (6-11) and (6-12) in their finite difference form, and can be carried out on a personal computer with high speed and accuracy. If desired, the characteristics can be displayed graphically. Values for ω and φ are found at discrete points along the inside boundary, and intermediate values can be obtained by interpolation. The finer the network of characteristics the more accurate is the solution.

The assumption for the velocity conditions at the inside boundary is that the velocity is normal to, and constant along, the boundary. Hence, an equivalent network of characteristics can be generated but now starting from conveniently spaced points around the inside boundary and moving out to intersect the periphery of the blank. This will enable the x and y velocity components to be evaluated at discrete points at the outside boundary; and for a given time step the new position of the free edge of the blank can be calculated. This was the method adopted to calculate the change in the geometry of the outside edge of the blank. The whole procedure is now repeated with new starting values for φ along the up-dated outside edge of the blank, and a new network of characteristics is generated inwards.

The object of the present study was to develop optimum blank shapes when deep drawing prismatic cups. However, some preliminary calculations were performed to examine the flow of material in the flange when deep drawing a square cup from a circular disc. Two flow patterns were examined. In the first case it was assumed that the first network of characteristics, generated from the boundary of the initially undeformed blank, remain unchanged throughout the deformation processes. This is not true, but the

change in the outside boundary of the blank can be calculated on this basis. The more realistic calculation is to generate a new network of characteristics as the outside boundary of the blank changes, this can be done for discrete time intervals as described earlier. The results of the two methods of calculation are shown in Figure 6-1, which show the flow lines and blank contours, at discrete time intervals, for 1/8 of the flange. The dashed lines represent results from the unchanging network of characteristics, while the solid lines indicate the results when continuously updating the characteristics. Since there are no severe strain gradients within the flange of the cup, retaining terms on the right hand side of equation (6-12) had little influence on the calculated blank shape.

The next section presents the results for the development of an optimum blank shape when deep drawing a square cup. The procedure was as described above, where at each time step a new network of characteristics is developed due to the change in geometry of the outside boundary of the blank.

6.2.3. Development of Optimum Blank Shapes

When developing an optimum shaped blank, the strategy is to ensure that the travel times of all particles from the outside boundary to the die cavity boundary are the same. The ideal blank can be developed iteratively using a computer, but the computation time can be reduced if the initial blank shape is close to the optimum. A near net shaped blank can be developed using plane strain slip line field analysis as the initial blank [146,149].

Given the initial blank shape a network of characteristics is developed using the finite difference form of equations (6-11) and (6-12). As described in the preceding section, an equivalent field is then constructed moving outwards, from the die boundary back to the blank edge. This field is then used to solve for the velocities at discrete points around the blank boundary. The velocities are determined using the finite difference form of equations (6-11) and (6-14). A suitable time step is chosen and the new position of the outer boundary determined. Since discrete points on the outside boundary are moved inwards, these have to be connected to form the new outside boundary. Three points at a time were selected and fitted with a polynomial. This enabled the slope, and hence φ , to be determined around the new outside edge of the blank. The process is then repeated, a new network of characteristics is generated from the outside edge of the blank to the punch boundary; an equivalent field is then constructed starting at the die boundary in order to determine the velocity at discrete points on the periphery of the blank. The process is continued until a particle from the blank boundary reaches the die cavity, since the initial blank shape may not be optimum the majority of the particles will not yet have reached the inside boundary. The distance of the particles from the inside boundary provides an indication as to how the shape of the initial blank must be modified in order that all particles reach the die cavity from the outside edge simultaneously.

An optimum blank shape for a square cup is illustrated in Figure 6.2. The initial blank profile is also shown for comparison, and it took about eight iterations to develop the optimum shape from the initial blank. With the existing computer program, seven time steps were selected (but this is optional) to cover the inward flow of the material

from the outside edge of the blank to the die cavity. The inward flow pattern is also shown in Figure 6.2, along with the blank contours at each stage in the deformation process.

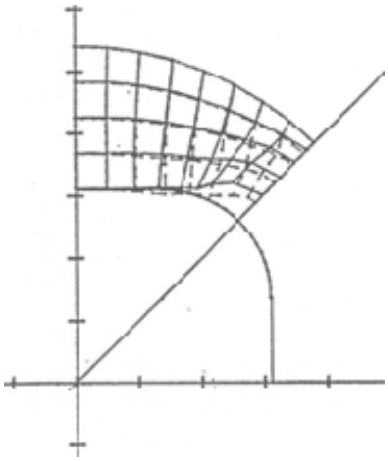

Figure 6.1. Comparison of flow patterns when draw a square cup from circular blank.

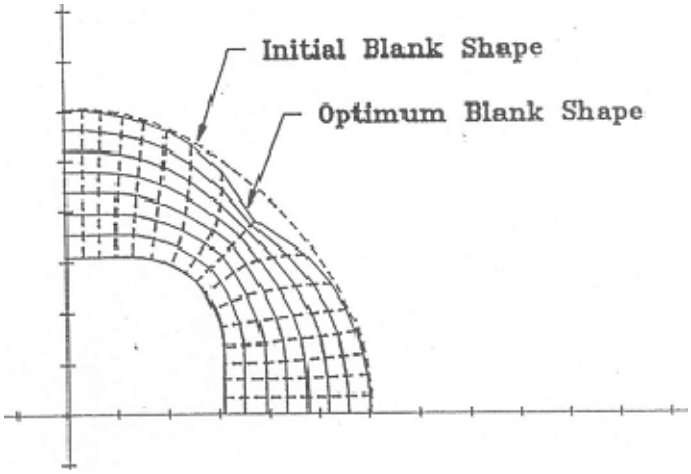

Figure 6.2. Optimum blank shape for a square cup.

Figure 6.3 demonstrates how the characteristics were generated, in order to calculate the shape of the outside edge of the blank at different stages during the drawing operation. Figure 6.3(a) shows four stages in the deep drawing of a square cup starting with an optimum shaped blank, the network of characteristics are generated inwards from the outside boundary. The same four stages in the deformation process are also shown in Figure 6.3(b), in this diagram the equivalent network of characteristics are shown, i.e. constructing the field outwards from the die boundary in order to find the velocity at points along the outside edge of the blank.

Optimum blanks were also developed for elliptical punches, and some of these results are discussed in the next section.

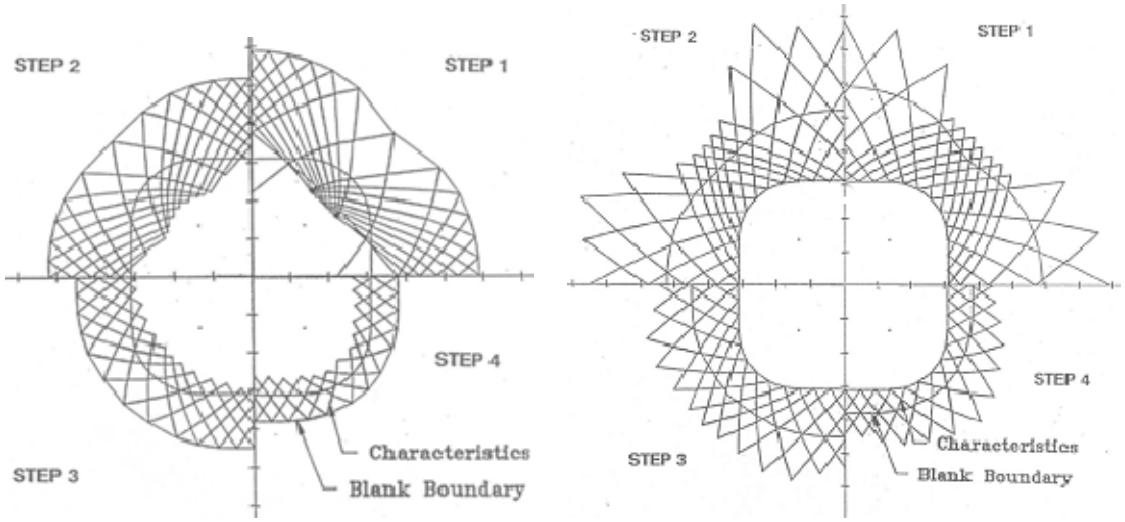

(a) (b)

Figure 6.3. Characteristics developed for a square cup drawing. (a) Generated inwards at four stages in the process, (b) an equivalent set of characteristics generated outwards.

6.2.4. Comparison with Experimental Results and Other Numerical Procedures

Ideal blank shapes were developed for elliptical punches and one such contour is shown in Figure 6.4. The punch geometry was taken from the work of Iseki and Murata [156], who developed ideal blank shapes using a rigid-plastic finite element code, assuming the flange of the cup was deformed under a state of plane stress. The blank shape predicted in Ref. [156] is reproduced in Figure 6.4 and it can be seen that it is indistinguishable from the contour predicted by the present method. Also shown for comparison is the ideal blank contour generated using plane strain slip line field analysis. Similar results for a square punch are shown in Figure 6.5. The finite element results are

again taken from Ref. [156], and the blank contour is in close agreement with that determined using plane stress characteristics.

Comparison with an experimentally determined optimum blank is shown in Figure 6.6. Square cups were drawn from an aluminum killed drawing quality steel, 1.0 mm thick. The experiments were performed on a Hille cupping press using a blank holder force of 7.2 KN. The square die cavity had a 62 mm side with a 17.5 mm corner radius. The experimentally determined optimum profile agrees very well with that predicted by the method of plane stress characteristics.

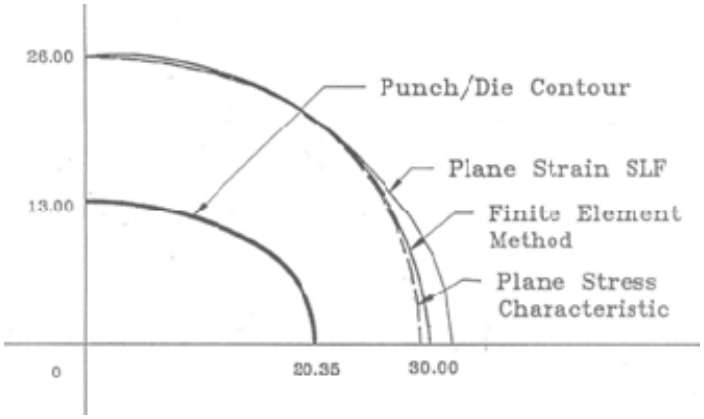

Figure 6.4. Ideal blank shapes developed for elliptical punch.

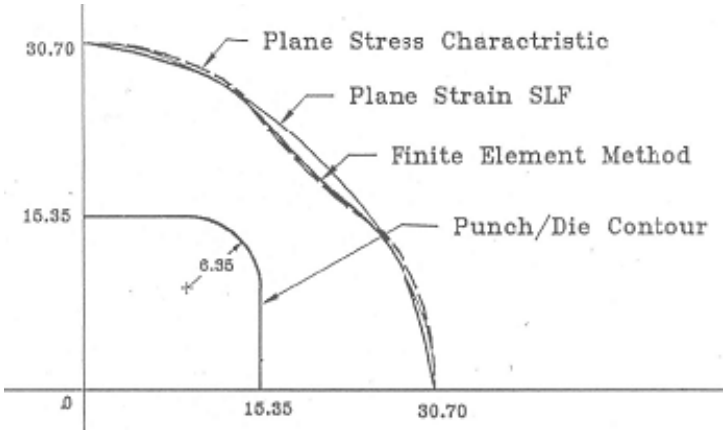

Figure 6.5. Ideal blank shapes developed for square punch.

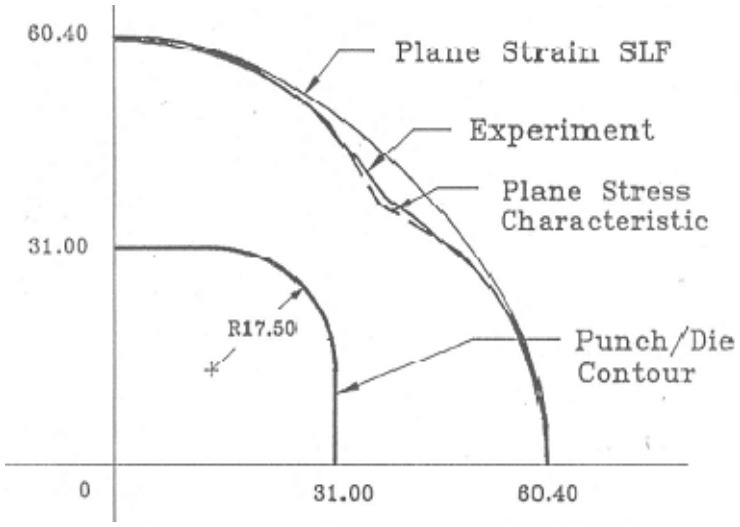

Figure 6.6. Optimum blanks calculated by SLF and PSC and compared with an experimentally determined blank.

6.3. THE METHOD OF SLIP LINE FIELD (SLF)

The slip line field method is based on plane strain formulation and assumes that the thickness does not change in the flange. The formulations are given by Hill [144] and the complete details will not be repeated here. An example is given in this section for the prediction of four fold symmetrical earing when deep drawing cylindrical cups.

6.3.1. **Prediction of Earing in Cylindrical Cups Drawn from Anisotropic Sheet**

The anisotropic model employed had been proposed earlier by Hill [157]. The general form of the yield criterion given is

$$2f(\sigma_{ij}) = F(\sigma_{yy}+\sigma_{zz})^2 + G(\sigma_{zz}+\sigma_{xx})^2 + H(\sigma_{xx}+\sigma_{yy})^2 + 2L(\sigma_{yz})^2 + 2M(\sigma_{zx})^2 + 2N(\sigma_{xy})^2 \quad (6\text{-}15)$$

where *F*, *G*, *H* etc. are parameters representative of the current state of anisotropy. For plane strain the above equation reduces to

$$\{\frac{FG+GH+HF}{F+G}\}(\sigma_{xx}-\sigma_{yy})^2+2N\sigma_{xy}^2=1 \qquad (6\text{-}16)$$

The equilibrium stress equations along the α and β lines can be formulated as

$$\begin{aligned} &P+2T\,g(\phi)=\text{const}\ \alpha \\ &P-2T\,g(\phi)=\text{const}\ \beta \end{aligned} \qquad (6\text{-}17)$$

In the above equation $\boldsymbol{p}=-(\sigma_\alpha-\sigma_\beta)/2$ and is the mean compressive stress, $\boldsymbol{T}$ is the yield stress in shear with respect to the principal *x*-*y* axes of anisotropy and $g(\phi)$ is

$$g(\phi)=\frac{\sin 2\phi\cos 2\phi}{2(1-c\sin^2 2\phi)^{1/2}}+\int_0^{\phi}(1-c\sin^2 2\phi)^{1/2}d\phi \qquad (6\text{-}18)$$

The quantity c is a lumped anisotropic parameter and is given by

$$c=1-\frac{N(F+G)}{2(FG+GH+HF)} \qquad (6\text{-}19)$$

When c = 0, Eqns (6-17) reduce to the Hencky equations for an isotropic material. The velocity equations along the characteristics are as follows [144]

$$\begin{aligned} &du-v\,d\phi=0 \quad \text{along an } \alpha \text{ characteristic} \\ &dv+u\,d\phi=0 \quad \text{along a } \beta \text{ characteristic} \end{aligned} \qquad (6\text{-}20)$$

where u and v are the components of velocity along the α and β characteristics, respectively. Equations (6-20) are identical to the Geiringer equations for an isotropic solid.

The characteristics of stress and velocity coincide for the anisotropic solid, and form an orthogonal network. The velocity characteristics are aligned with the directions of maximum shear strain. However, in general, the principal strain rate axes and the principal stress axes are not coincident, and hence the characteristics will not normally meet a free surface at ±45°.

The principal axes of anisotropy of a sheet metal are usually assumed to be along the rolling and transverse directions. A circular disk cut from the sheet will have one diameter aligned with the rolling (x) direction and one at right angles coinciding with the transverse (y) direction. Thus the orientation of any point on the blank boundary with respect to the x-direction of anisotropy is known. It can be shown [144] that the slope of a characteristic with respect to the x-direction of anisotropy is

$$\phi = (\delta - \gamma) = \frac{1}{2}\cot^{-1}\{(1-c)\tan 2\gamma\} \tag{6-21}$$

where γ is the angle between the free surface and the x-direction of anisotropy and δ is defined as the angle the characteristic makes with the free surface.

The construction of the stress and velocity characteristics is now essentially the same as described in Ref. [152], and in the preceding section. The stress state is constant at the outside edge of the blank and the slope of the characteristics, as they intersect the free surface, are known from Equation (6-21). Hence the quality g(ϕ) in Equation (6-18)

is known at every point on the rim of the blank, once a value for the anisotropic parameter c has been selected. The quantity g(ϕ) was evaluated numerically using the method of Gaussian Quadratures [158], at selected points around the rim of the blank. The stress characteristics can now be extended inwards as shown in Figure 6.7, and the hydrostatic stress quantity p/2T and the value of g(ϕ) evaluated at a typical intersection point C of two characteristics using Equations (6-17). Once $g(\phi_c)$ has been evaluated it is possible to calculate the slope ϕ_c using an iterative procedure. Since the x-y coordinates are known at every point on the rim of the blank then the coordinates of point C i.e. Xc and Yc can be determined. This can be achieved by replacing the curved line elements AC and BC in Figure 6.7 by chords with mean slopes of

$$(90 + \phi_A + \phi_c)/2 \text{ and } (\phi_B + \phi_c)/2 \tag{6-22}$$

respectively. This process is repeated for every intersection point as the characteristic mesh is extended inwards. The angle of intersection of the characteristic with the inner (punch) boundary can then be evaluated; some interpolation maybe necessary. The velocity at the inner boundary is assumed constant and directed inwards and everywhere normal to the boundary. The velocity characteristics, given by Equation (6-20), can now be extended outwards into the flange to meet the free surface. The velocity components are then known at discrete points at the free surface, and for a chosen time interval, the outside boundary can be stepped inwards. With the aid of a smoothing algorithm the orientation of the new outer boundary with respect to the x-axis of anisotropy is known,

and the whole process is then repeated with the stress characteristics being generated inwards.

Figure 6.8 (a) shows the stress characteristics which have been propagated inwards from the outside boundary of an initially circular blank at the start of the drawing process; because of symmetry. attention can be restricted to a 45º quadrant. Figure 6.8(b) shows the velocity characteristics mapped outwards from the inner boundary. The value for the anisotropy parameter in these calculations was C = -0.3. Figure 6.9 illustrates how the "ears" and "hollows" develop as the blank is drawn inwards. Four fold symmetrical earing is exhibited and the calculation was stopped when a point on the rim of the blank had traveled inwards to arrive at the inside boundary. When c is negative the "ears" form in the ±45º directions, and for c positive the "ears" form in the rolling and transverse directions.

It is also possible to generate optimum blanks for any state of anisotropy characterized by the c-parameter. An optimum blank for c = -0.3 is shown in Figure 6.10, and would produce a flat topped cup upon completion of the drawing process.

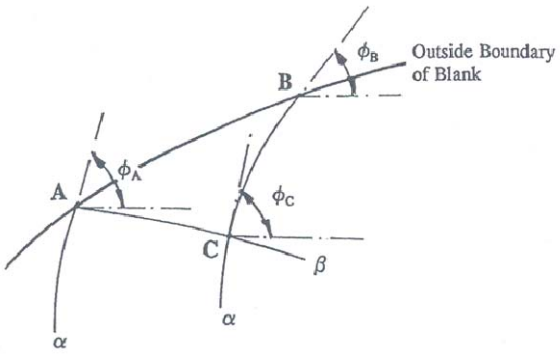

Figure 6.7. Extension of the slip line field from a stress free boundary along which ***p*** and ϕ are known.

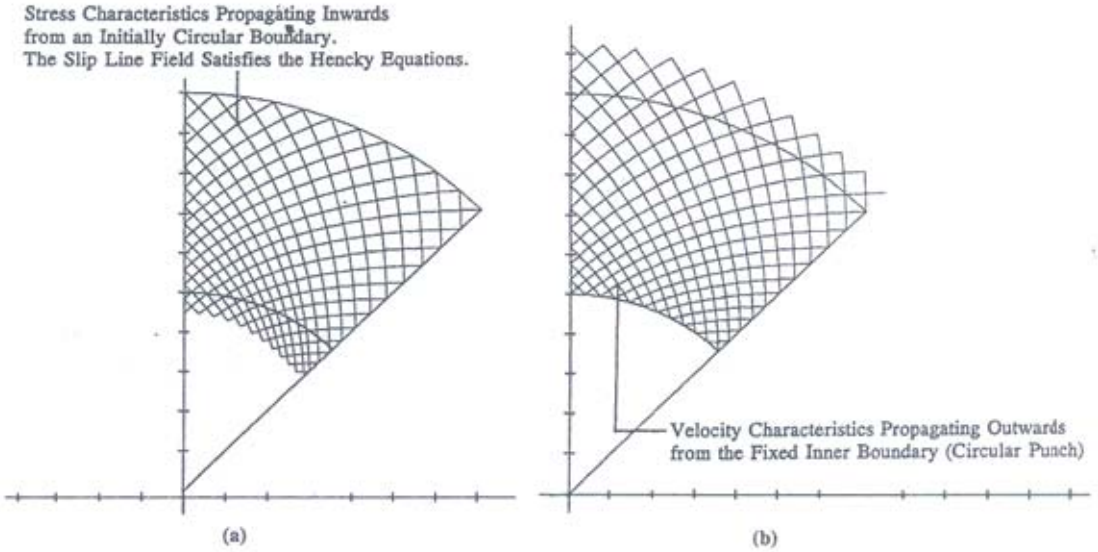

Figure 6.8. (a) The stress characteristics shown propagating inwards from the blank boundary, when modeling the deep drawing of a cylindrical cup from an initially circular blank, cut from anisotropic sheet material. (b) Similar to (a), but here the velocity characteristics are shown propagating outwards from the inside circular boundary (corresponding to the punch boundary).

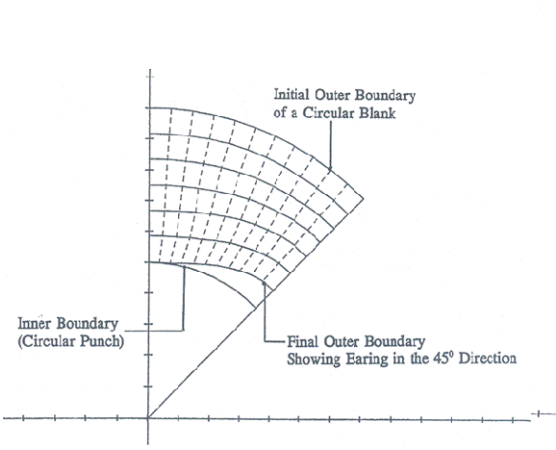

Figure 6.9. The "ears" and "hollows" develop as the blank is drawn inwards

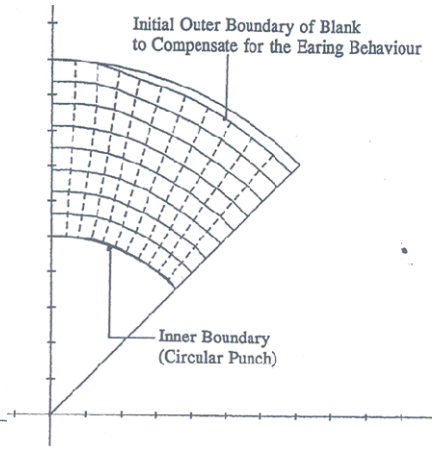

Figure 6.10. Optimum blank to make a flat topped cup.

6.4. CONCLUSIONS

- The PSC formulations of planar anisotropy including the r value have been developed and the characteristics of stress and velocity coincidence were established.
- The PSC method can be used to analyze the flange deformations and obtain optimum blank shapes. The predicted optimum profiles agree very well with those determined using a FEA and the experimental data when deep drawing square cups.
- The method of plane strain characteristics can be used to predict four fold symmetrical earing throughout the entire deep drawing cylindrical cups from initially circular disks.

CHAPTER 7. GENERAL CONCLUSIONS

- Forming issues such as springback, shear fracture and edge crack are barriers to further applications of AHSS to automotive applications. Many of these problems cannot be predicted using conventional simulation methods because the AHSS behaviours are significantly different from conventional steels in work hardening and fracture mechanism. In this study, new simulation technology has been developed to improve the predictability for AHSS forming. The technologies integrated various aspects of simulation techniques including optimisation of simulation parameters, development of material models, establishment of local formability criteria and validation with experimental data.

- Modified Yoshida's nonlinear isotropic/kinematic hardening material model has been implemented. This model adequately describes the Baushinger effect of AHSS deformation. Significant improvement has been achieved in simulation for the problems of loading/reverse loading (bending/unbending).

- Springback prediction has been significantly improved using the newly developed simulation technology which includes the implementation of the smooth contact, selective mass scaling and Yoshida nonlinear isotropic/kinematic hardening model. Prediction accuracy for an automotive load beam made from DP980 improved to 93% from 55% using the conventional approach.

- The MMC fracture criterion has been implemented and has adequately predicted AHSS fractures. Various experiments have been conducted to calibrate the parameters. A wide range of fracture strain limit has been generated.

- Validation of simulations that made use of the MMC fracture criterion for shear fractures showed good agreement with the experimental data on the SFS and BUT tests. A case study on a larger part showed that using the MMC model improves shear fracture prediction for sharp radii, but is less accurate in areas with large radii. The MMC model should be used for shear fracture predictions in tight radii, and the conventional FLC should be used for other failure predictions in sheet metal forming simulations of AHSS.

- AHSS sheared edge shape is less regular and the four zone feature is not consistent. An alternative approach has been proposed to measure sheared edge deformation and work hardening. Measuring flow line angle change is a more reliable approach to evaluate sheared edge deformation of AHSS.
- MMC failure criterion has been used in shearing simulations of AHSS. When the shearing deformation is included in the hole expansion simulation, the equivalent plastic strain (or edge damage) is significantly higher. Therefore the shearing deformation must be included in hole-expansion simulation for correct prediction.
- Conventional pre-forming approaches are not always applied to AHSS edge stretching. There is a critical strain value for pre-forming and edge stretching which is a boundary of failure occurring in or out of the pre-formed region. This strain value

depends on the pre-formed geometry, edge damage severity, steel grade and material orientation.

- The conventional FLD cannot be used to predict edge failure in pre-forming and post stretching since the failure limit is much lower due to sheared edge and stretch bending deterioration. The limit strain can be measured with the pre-form and stretch test. Simulation technologies have been developed to predict the bending and unbending strains of pre-forming and subsequent stretching which uses implicit solver with isotropic/kinematic hardening model.
- The PSC formulation of normal anisotropy by including the R value has been developed and the characteristics of stress and velocity coincidence were established. The PSC method can be used to analyze the flange deformations and obtain optimum blank shapes. The method of plane strain characteristics can be used to predict four fold symmetrical earing throughout the entire deep drawing process of a cylindrical cup.

BIBLIOGRAPHY

1. Auto-Steel Partnership, "*Final Report: Light Weight Front End Structure*", www.autosteel.org.
2. D. Schultz and Abey Abraham, " *North American Light Vehicle Metallic Material Trends***",** Ducker Worldwide , Great Design in Steel, 2009, www.autosteel.org.
3. M. F. Shi and X. Chen, "*Stretch Flange-ability Limits of Advanced High Strength Steels*", SAE technical paper 2007-01-1693
4. International Iron and Steel Institute (IISI) "*Advanced High Strength Steel Applications Guidelines*",2005, www.autosteel.org.
5. X. Chen, D.R. Coopmans, R.D. Dell'Osso, P.J. Belanger,"*Stamping and Crash Performance of Dual Phase Steel"*, International Body Engineering Conference (IBEC), 2001.
6. X. Chen, M.F. Shi, P.M. McKune, S.M. Chen, "*Applications of High Strength Steels in Hydroforming Dual Phase Vs. HSLA",* SAE Technical Paper, 2001-01-1133.
7. X. Chen, M.F. Shi, *"Denting Simulation and Verification",* Sheet Metal Forming, P25, 2002, Society of Automotive Engineering. SAE Technical Paper, 2002-01-0789.
8. Hyunok Kim, Yu-Ping Yang, Rich Green, "*Failure Analysis of Advanced High Strength Steels during Draw-Bending*", final report to Auto-Steel Partenship, October,2009, www.autosteel.org.
9. A. Konieczny, "*On Formability Assessment of the Automotive Dual Phase Steels*," SAE Technical Paper # 2001-01-3075, 2001.
10. S. P. Keeler, W. G. Brazier, "*Relationship between Laboratory Material Characterization and Press Shop Formability*," Proc. Of Microalloying 75, New York, pp. 517-530, 1977.
11. X.M. Chen, D.A. Witmer, M. Kamura, and Y. Omiya, "*Metal Forming Characterization and Simulation of Advanced High Strength Steels*", SAE Technical Paper # 2004-01-1048 (2004)
12. American Iron and Steel Institute, "*Advanced High Strength Steel Applications–Design and Stamping Process Guidelines*", 2010, www.autosteel.org.
13. C. Du, Y. Hu, M.F. Shi, X.M. Chen, S.D. Liu, S. D., and H. Yao, "*A Rail Type Stamping Springback- Experiment vs. Simulation*", USNCCM-VI Conference, Dearborn, 2001.
14. J. Fekete, "*Product and Process Effects on Stamping Performance of Advanced high-strength steels*", Great Design in Steel Seminar, American Iron and Steel Institute, March, 2006, www.autosteel.org
15. C. Du, Jin Wu, Marcio Militisky, James Principe, Mark Garnett, Li Zhang "*Springback Control with Variable Binder Force-Experiments and FEA Simulation*", The 8th International Conference on Numerical Methods of Industry Forming Processes, Columbus, USA, 2004.
16. M.Y. Demeri, M. Lou and M.J. Saran, "*A Benchmark Test for Springback Simulation in Sheet Metal Forming*", SAE 2000-01-2657, International Body Engineering Conference, Detroit, Michigan (2000).

17. X. Chen, Feng Ren, Ming Shi, Cedric Xia, "Springback *Prediction on Slit-Ring Test*", Proceedings of the 5th International Conference NUMISHEET, 2005
18. M. Kadkhodayan, Iman Zafarparandeh, "*L-bending Analysis with an Emphasis on Springback*", Proc. of Numisheet2008, Interlaken, Switzerland, September, 2008.
19. A. Ghaei, A. Taherizadeh, D. E. Green "*The effect of hardening model on springback prediction for a channel draw process*", Proc. of Numisheet2008, Interlaken, Switzerland, September, 2008.
20. M. Goslingl, A. Brosinsl, A. E. Tekkayal, "*Study on the Accuracy of Springback Predictions by Finite Element Analysis*", Proc. of Numisheet2008, Interlaken, Switzerland, September, 2008.
21. K. Roll, T.Lemke, K, Wiegand, "*Possibilities and Strategies for Simulations and Compensation for Springback*", Proc. of NUMISHEET2005, Part-A, 295-302, 2005.
22. Q.V. Bui, L., Papeleux, J.P. Ponthot, "*Numerical simulation of sp,"ingback using enhanced assumed strain elements*", Journal of Materials Processing Technolology, 153-154:314-318,2004.
23. L. Papeleux J.P. Ponthot, "*Finite element simulation of springback in sheet metal forming*", Journal of Materials Processing Technology, 125-126:785-791,2002.
24. I.N. Chou, C. Hung, "*Finite element analysis and optimization on springback reduction*", International Journal of Machine Tools and Manufacturing, 39:517-536,1999.
25. K.P. Li, W.P. Carden and R.H. Woganer, "*Simulation of Springback*", Int. J. Mech. Sci. 44, 103-122
26. S. Xu, Kunmin Zhao, Terry Lanker, Jimmy Zhang and C.T. Wang, "*On Improving the Accuracy of Springback Prediction and Die Compensation*, SAE Technical Paper 2007-01-1687.
27. R. H. Wagoner and M Li, "*Advances in Springback",* Proc. of NUMISHEET2005, Part-A, 209-214, 2005.
28. W. Gan, R.H. Wagoner, "*Die design method for sheet springback",* International Journal of Mechanical Sciences 46:1097- 1113, 2004.
29. W.D. Carden, L.M. Geng, D.K. Matlock, R.H. Wagoner, "*Measurement of springback,* International Journal of Mechanical Sciences 44:79-101,2002.
30. X. Chen, M.F. Shi, Xinghai Zhu, Changqing Du, Z. Cedric Xia, Siguang Xu and Chuan-Tao Wang, "*Springback Prediction Improvement Using New Simulation Technologies*", SAE Technical Paper 2009-01-0981.
31. Proceeding of NUMlSHEET 1993, Toyko, Japan
32. Proceeding of NUMlSHEET1996, Dearborn, MI, USA
33. Proceeding of NUMlSHEET 1999, Besancon, France
34. Proceeding of NUMlSHEET2002 Jeju, Korea,
35. Proceeding of NUMlSHEET2005, Detroit, USA
36. Proceeding of NUMlSHEET2008, Intertaken, Switzerland
37. R.H. Wagoner, M. Li, "*Simulation of springback:Through-thickness integration", International Journal of Plasticity*. Vol. 23, 2007, pp. 345-360, ISSN 0749-6419.

38. Z. Cedric Xia and Danielle Zeng, "*Understanding Through-Thickness Integration in Springback Simulation*", Proc. of NUMISHETT2005, Part- A, 241-246, 2005.
39. H. Yao, S. D. Liu, C. Du, and Y. Hu, "*Techniques to improve spring back prediction accuracy using dynamic explicit FEA codes*", SAE Technical Paper, 2002-01-0159.
40. USAMP Project AMD 408, "*Final Report: Die Face Engineering for Advanced Sheet Forming*", 2005, www.uscar.org.
41. N. Ma, Yasuyoshi Umezul, Yuko Watanabel, Takaki Ogawa, "*Springback Prediction by Yoshida-Uemori Model and Compensation of Tool Surface Using JSTAMP*", Proc. of Numisheet2008, September, 2008, Interlaken, Switzerland.
42. N. Iwata, H. Tsutamori, M. Niihara, H.Ishikura, Y.Umezu, A.Murata, Y. Yoga : *Numerical Prediction of Springback Shape of Severely Bent Sheet Metal,* Proc. of NUMIFORM'07, Part-B, 799-804, 2007
43. S.W. Lee, D.Y. Yang, " *An assessment of numerical parameters influencing springback in explicit finite element analysis of sheet metal forming process",* Journal of Materials Processing Technology, Vol. 80-81,1998, pp. 60-67, ISSN 0924-0136.
44. Xu, W.L.; Ma, C.H.; Li, C.H.; Feng, W.J., "*Sensitive factors in springback simululation for sheet metal forming",* Journal of Materials Processing Technology, Vol. 151,2004, pp. 217-222, ISSN 0924-0136.
45. H. Zhu, L. Huang and C. Wong, "*Unloading Modulus on Springback in Steels*", SAE Technical Paper 2004-01-1050
46. L. Sun, R. Wangoner, "*Complex unloading behavior: Nature of the defromation and its consistent constitutive representation*", Proc. Numisheet 2011, Seoul, Korea.
47. F. Yoshida, and T. Uemori, "*A model of large- strain cyclic plasticity* describing *the Bauschinger effect andworkhardening stagnation",* Int. J. Plasticity, 18,661-686, 2002.
48. F. Yoshida, and T. Uemori, "*A model of large- strain cyclic plasticity and its application to springback simulation",* Int. J. Mechanical Sciences, 45, 1687-1702,2003.
49. X. Li, Y. Yang, Y. Wang,, J. Bao, S. Li, "*Effect of material-hardening model on the springback simulation accuracy of V- free bending.* Journal of Materials Processing Technology, 123:209-211,2002.
50. J.L. Chaboche, "*Time independent constitutive theory for cyclic plasticity*", Int. Plasticity, vol.2, 149-188, 1986.
51. F. Yoshida, T. Uemon , S. Abe , R. Hmo, "*A Model of Large-strain Cyclic Plasticity and Its Numerical Simulation Applications to Springback* ", Proc. of Numisheet2008, September, 2008 -Interlaken, Switzerland.
52. K. Chung, M. Lee, D. Kim, C. Kim, M.L. Wenner, F. Barlat, "*Springback evaluation of automotive sheets based on isotropic-kinematic hardening laws and non-quadratic anisotropic yield functions Part I: theory and formulation*", International Journal of Plasticity 21:861- 882,2005.

53. Y. Choi, C. Han, J.K. Lee, R.H. Wagoner, "*Modeling multi-axial deformation of planar anisotropic elasto-plastic materials, part I: Theory*", International Journal of Plasticity 221745-1764,2006.
54. B.K. Chun, H. Y. Kim, J.K. Lee, "*Modeling the Bauschinger effect for sheet metals, part I: theory*", International Journal of Plasticity 18:571-595, 2002.
55. J. Gau, G.L. Kinzel, "*A new model for spring back prediction in which the Bauschinger effect is considered*", International Journal of Mechanical Sciences 43:1813-183, 2001.
56. M. F. Shi, Xinhai Zhu, Cedric Xia, Thomas Stoughton, "*Determination of Non-linear Isotropic/Kinematic Hardening Constitutive Parameters for AHSS using Tension and Compression Tests*", Numisheet 2008, Interlaken, Switzerland, September, 2008.
57. D. Zeng and Z. Cedric Xia, "*An Anisotropic Hardening Model for Springback Prediction",* Proc. of NUMISHEET2005, Part- A, 241-246, 2005.
58. R. Hill, " *A theory of the yielding and plastic flow of anisotropic metals",* Proc. Royal Society of London, A193, 281-297,1948.
59. R. Hill, " *Constitutive modelling of orthotropic plasticity in sheet metals",* J. Mechanics and Physics of Solids, 38, 405-417,1990.
60. M. Gotoh, "*A theory of plastic anisotropy based on ayieldfunction offourth order (plane stress state) –I",* Int. J, Mechanical Sciences, 19,505-12,1979.
61. A. Tang, W, Lee, J, He, J, Xu, K, Liu and C.C.Chen: *Die face Engineering Based on Springback Compensation Strategy and Implemention,* Proc. of NUMISHEET2005, Part-A, 314-321, 2005.
62. X. Chen, Meng Luo, M.F. Shi, Hua-Chu Shih and Tomasz Wierzbicki, "*AHSS Shear Fracture Predictions Based on a Recently Developed Fracture Criterion*", SAE technical paper, 2010-01-0988.
63. Hua-Chu Shih and Ming F. Shi, "*Experimental Study On Shear Fracture Of Advanced High Strength Steels*", MSEC-ICMP 2008-72046.
64. A.W.Hudgins, D.K. Matlock and J.G. Speer, "*Shear Failures in Bending of Advanced High Strengh Steels*", Proceeding of International Deep Drawing Research Group Conference, P53, June 2009.
65. J. H. Kim, Ji Hyun Sung and R.H. Wagoner, "*Thermo-Mechanical Modeling of Draw-Bend Fomability Tests*", Proceeding of International Deep Drawing Research Group Conference, P503,June 2009.
66. M.S. Walp, A. Wurm, J. F. Siekirk III, and A. K. Desai, "*Shear Fracture in Advanced High Strength Steels*", SAE Technical Publication #2006-01-1433, 2006.
67. S. Sriram, C. Wong, M. Huang, and B. Yan, "*Stretch Bendability of Advanced High Strength Steels*", SAE Technical Report #2003-01-1151, 2003.
68. D. Kitting, A. Ofenheimer, M. Jain, H. Pauli, and G. Rabler, "*Experimental Characterisation of Failure of Stretch-Bend Steel Sheets*", Numisheet, Interlaken, Switzerland, pp. 315-320, 2008.
69. M. Huang, L. Zhang, and L. Yang, "*On The Failure of AHSS at Tooling Radius*", Numisheet2008, Interlaken, Switzerland, pp. 307-309, 2008.

70. M. Yoshida, F. Yoshida, H. Konishi, and K. Fukumoto, "*Fracture limits of sheet metals under stretch bending*", International Journal of Mechanical Sciences, vol. 47, pp. 1885-1896,2005.
71. Hua-Chu Shih, Ming F. Shi, Z. Cedric Xia and Danielle Zeng, "*Experimental Study On Shear Fracture Of Advanced High Strength Steels Part II*", MSEC 2009-84070.
72. M. Luo, "*Validation of the MMC fracture model on USS stretch-forming test*", Technical Report 198, Impact and Crashworthiness Lab, Massachusetts Institute of Technology, 2009.
73. B. S. Levy, and C. J.Van Tyne, "*Predicting breakage on a die radius with a straight bend axis during sheet forming*", Journal of Materials Processing Technology, vol. 209, pp. 2038-2046, 2009.
74. Walters, "*Development of a punching technique for ductile fracture testing over a wide range of stress states and strain rates*", Ph.D. Thesis, Massachusetts Institute of Technology, 2009.
75. L. M. Smith, R. C. Averill, J. P. Lucas, T. B. Stoughton, and P. H. Matin, "Influence *of transverse normal stress on sheet metal formability*", International Journal of Plasticity, vol. 19, pp. 1567-1583,2003.
76. T. B. Stoughton, and X. Zhu, "*Review of theoretical models of the strain-based FLD and their relevance to the stress-based FLD*", International Journal of Plasticity, vol. 20, pp. 1463-1486
77. J. Wu, D. Zhou, L. Zhang, Y. Zhou, C. Du and M. F. Shi, "*A Failure Criterion for Stretch Bendability of Advanced High Strength Steels*", 2006 SAE International Congress and Expositions, Technical Paper No. 2006-01-0349.
78. M. G. Cockcroft, and D. J. Latham, "*Ductility and the workability of metals*," Journal of the Institute of Metals, vol. 96, pp. 33-39, 1968.
79. J.R. Rice, D.M. Tracey, "*On the ductile enlargement of voids in triaxial stress fields*", J. Mech. Phys. Solids 17 (1969) 201-217.
80. Gurson A.L., "*Continuum theory of ductile rupture by void nucleation and growth. Part I, yield criteria and flow rules for porous ductile media*", J. of Eng. Material Technology, 1977.
81. H. Kim, A. R. Bandar, Y. P. Yang, J. H. Sung, and R. H. Wagoner, "*Failure Analysis of Advanced High Strength Steels (AHSS) During Draw Bending*." International Deep Drawing Research Group, Golden, CO, USA, pp. 449-460, 2009.
82. Y. Bao, and T. Wierzbicki, "*A Comparative Study on Various Ductile Crack Formation Criteria*", Journal of Engineering Materials and Technology, vol. 126, pp. 314-324, 2004.
83. Y. Bai, and T. Wierzbicki, "*Predicting Fracture of AHSS Sheets on the Punch and Die Radii Sidewall.*" Numisheet, Interlaken, Switzerland, pp. 297-306, 2008.
84. M. Luo, X. Chen Ming F. Shi, Hua-Chu Shih, "*Numerical Analysis of AHSS Fracture in a Stretch-bending Test*", Numiform 2010, Korea.
85. M. Dunand and D. Mohr, "*Ductile Fracture of AHSS Sheet under Multi-axial Loading: Experiments and Modeling*", Proc. Numisheet 2011, Seoul, Korea.

86. K. Nielsen, V. Tvergaard, Eng. Fract. Mech., 77, 1031-1047 (2010)
87. X. M. Chen , C.Du, X. Wu , X. Zhu ,and S-D. Liu, "*Sheet Metal Shearing and Edge Characterization of Dual Phase Sheets*", IDDRG International Conference, June 2009.
88. W. Johnson, S. K. Ghosh, and S. R. Reid, "*Piercing and Hole-Flanging of Sheet Metal - A Survey*", Memoires Scientifiques De La Revue De Metallurgie, vol. 77, pp. 585-606, 1980.
89. A. Konieczny and T. Henderson "*On Formability Limitations in Stamping Involving Sheared Edge Stretching* ", SAE Technical paper # 2007-01-0340.
90. A. Dalloz. A-F. Gorgues-Lorenzon, A. Pineau, J. Besson, T. Sturel, "*Influence of the Cutting Process on Damage in Dual Phase Steels*", Material Science and Technology (MS&T07), Detroit, Michigan, USA, 2007.
91. S. Sriram and J. Chintamani, "*Guidelines for Stretch Flanging Advanced High Strength Steels*", Proceedings of the NUMISHEET 2005, Dearborn, Michjgan.
92. J. Chintamani, S. Sriram, "*Sheared edge Characterization of Steel Products Used for Closure Panel Applications*", SAE Technical Paper 2006-01-1589.
93. R.D. Adamczyk, D. W. Dikinson, and K.P. Krupitzer, "*The Edge Fonnability of High-Strength Cold- Rolled Steel*," SAE Technical Report #830237,1983.
94. R.J. Comstock, D.K. Scherrer, and R.D. Adamczyk, "*Hole Expansion in a Variety of Sheet Steels,*" Journal of Materials Engineering and Performance, vol. 15,2006, pp. 675-683.
95. A. Karelova. and C. Krempaszky, "*Influence of the Edge Conditions on the Hole Expansion Property of Dual Phase and Complex Phase Steels*", MS&T, 2007, pp. 159-169.
96. ISO –International Organization for "*Standardization Method of Hole Expanding Test*", ISO/TS 16630-2003.
97. Y. Seo,"*Improve blank condition in progressive stamping: Reduction edge defects improves subsequent forming*", Stamping Journal, Vol.15, 2003, pp.38-40.
98. S.P. Keeler, "*Understanding Sheet Metal Formability, Part5-Die Design and Lubrication*", Machinery, Vol.74, no.10, June, 1968.
99. C. Chiriac, "*Sheared Edge Performance of DP780 Steels -Conventional vs. Improved Bending and Flanging (IBF) Steels*", Materials Science and Technology (MS&T) 2010 , Houston, Texas.
100. B.S. Levy, C.J. Van Tyne, "*Failure during Sheared Edge Stretching*", J. of Material Engineering and Performance, 2006.
101. Chiriac, C., "*A Study of the Plastic Deformation of Sheared Edges of Dual Phase 780 Steel*", *SAE Technical Report #2010-01-044,* 2010.
102. R.D.K. Misra, S.W. Thompson, T.A. Hylton, and A.I. Boucek, "*Microstructures of Hot-rolled high strength steels with significant differences in edge formability*", *Metallurgical and Materials Transactions A,* vol. 32, 2001, pp. 745-760.
103. X. Fang, Z. Fan, B. Ralph, P. Evans, "*The Relationship Between Tensile Properties and Hole Expansion property of C-Mn Steels*", Journal of Materials Science 38(2003), p. 3877-3882.
104. Y. Takahashi, O. Kawano, Y. Tanaka, M. Ohara, "*Fracture Mechanical Study on Edge Flange ability of High Tensile Strength Steel Sheets*", MS&T 2009 Conference Proceedings, p.1317-1328.
105. K. Hasegawa, K. Kawamura, T. Urabe, and Y. Hosoya, "*Effects of microstructure on stretch-flange-formability of 980 MPa grade cold-rolled ultra high-strength steel sheets,*" ISIJ International, vol. 44, pp. 603-609, 2004.

106. E Iizuka, K Hashimoto, "*Effects of Anisotropic Yield Functions on the Accuracy of Forming Simulations of Hole Expansion*", IDDRG 2009 Conference, p 153-163.
107. Y. Ito, K. Hashiguchi, N. Ohashi, "*Effect of Plastic Anisotropy on the Bore Expanding Behavior of Cold Rolled Steel Sheets*", Research Laboratories, Kawasaki Steel Corporation.
108. J. Wang, T.M. Link, M.J. Merwin, "*AHSS Edge Formability in Sheared-Edge Tension*", AIST 2008 Conference Proceedings, p.361-366.
109. X. Chen, Ke Chen, Lorenzo Smith, "*Pre-Forming Effects on AHSS Edge Cracking* ", Proc. of Numisheet 2011, Soul, Korea.
110. X. Wu, Chunlei Xie, and Hamed Bahmanpour, "*Flange Shear Affected Zone Study*", Technical Report to Auto Steel Partnership, September, 2008. www.autosteel.org.
111. D. Zhou, C. Du, J. Siekirk, J. McQuaire, X. Chen and B.S. Levy, "*A Practical Failure Limit for Sheared Edge Stretching of Automotive Body Panels*", SAE Technical Paper, 2010-01-0159.
112. N.M.Wang and M.L. Wenner, "*An Analytical and Experimental Study of Stretch Flanging*", Int. J. Mech. Sci., 16, p135, 1974.
113. C.T. Wang, G Kinzel and T. Altan, "*Failure and suggestions regarding this paper. Wrinkling Criteria and Mathematical Modeling of Shrink and Stretch Flanging Operations in Sheet Metal Forming*", Journal of Materials Processing Technology, 53, p759, 1995.
114. C. McEwan, R. Underhill, N. Langerak, G. Botman and M. de Bruine, "*A New Approach to Predict Edge Splits – The combined FLC/HEC Diagram*", IDDRG 2009 International Conference, June 2009, Golden, Co., USA.
115. D. Zeng, Z. Cedric Xia, "*Stretch flanging formability prediction and optimization*", SAE Technical Paper, 2006-01-0403.
116. X. M. Chen, P.M. Mckune D.G. Prince, "*Automotive Application of Stretch Flange High Strength Steel*", SAE technical paper, 2003-01-0690.
117. S.E. Clift, P. Hartley, C.E.N. Sturgess, G.W. Rowe, "*Fracture Prediction in Plastic Deformation Process*", Int. J. Mech.Sci. 32 (1990) 1-17.
118. A.M. Goijaerts, L.E. Govaert, D. Brokken, "*Evaluation of ductile fracture criteria model for different metals in blanking,*" Journal of Materials Processing Technology, vol. 192-193, pp. 237-242, 2007.
119. A.M. Goijaerts, L.E. Govaert, F.P.T. Baaijens, "*Prediction of ductile fracture in metal blanking*", J. Manuf. Sci. Eng:, Trans. ASME 122 (2000) 476-483.
120. Y.W. Stegeman, A.M. Goijaerts, L.E. Govaert, D. Brokken, "*An experimental and numerical study of planar blanking process process*", Journal of Materials Processing Technology, vol. 192-193, pp. 237-242, 2007.
121. D. Brokken, W. A. M. Brekelmans, "*Numerical modeling of the metal blanking process*", Journal of Materials Processing Technology 83(1-3): 192-199, 1988.
122. R. Hambli and F. Guerin, "*Application of a neural network for optimum clearance prediction in sheet metal blanking processes*", Finite Elements in Analysis and Design 39(11): 1039-1052, 2003.
123. C. Husson, J. P. M. Correia, "*Finite elements simulations of thin copper sheets blanking: Study of blanking parameters on sheared edge quality*", Journal of Materials Processing Technology 199(1-3): 74-83, 2008.
124. S. Thipprakmas, M. Jin, "*An investigation of material flow analysis in fineblanking process*", Journal of Materials Processing Technology 192-193: 237-242.

125. R. Wiedenmann, P. Sartkulvanich, and T. Altan, "*Finite Element Analysis on the Effect of Sheared Edge Quality in Blanking Upon Hole Expansion of Advanced High Strength Steel*", IDDRG, pp. 559-570. June 2009, Golden, Co., USA.
126. G. Avramovic-Cingara, C. A. R. Saleh, M. K. Jain and D. S. Wilkinson, "*Void Nucleation and Growth in Dual-Phase Steel 600 during Uniaxial Tensile Testing*," Metallurgical and Materials Transactions A, vol. 40, pp. 3117-3127, 2009.
127. D. Steinbrunner, D. Matlock, and G. Krauss, "*Void formation during tensile testing of dual phase steels*," Metallurgical and Materials Transactions A, vol. 19, pp. 579-589, 1988.
128. G. Avramovic-Cingara, Y. Ososkov, M. K. Jain, and D. S. Wilkinson, "*Effect of martensite distribution on damage behaviour in DP600 dual phase steels*," Materials Science and Engineering: A, vol. 516, pp. 7-16, 2009.
129. N. Kim, and G. Thomas, "*Effects of morphology on the mechanical behavior of a dual phase Fe/2Si/0.l C steel*," Metallurgical and Materials Transactions A, vol. 12, pp. 483-489, 1981.
130. S. Kim, and S. Lee, "*Effects of martensite morphology and volume fraction on quasi-static and dynamic deformation behavior of dual-phase steels*," Metallurgical and Materials Transactions A, vol. 31, pp. 1753-1760, 2000
131. C. Thomser, V. Uthaisangsuk, and W. Bleck, "*Influence of Martensite Distribution on the Mechanical Properties of Dual Phase Steels: Experiments and Simulation,*" Steel Research International, vol. 80, pp. 582-587, Aug, 2009.
132. U. Prahl, S. Papaefthymiou, V. Uthaisangsuk, W. Bleck, J. Sietsma, and S. van der Zwaag, "*Micromechanics-based modelling of properties and failure of multiphase steels,*" Computational Materials Science, vol. 39, pp. 17-22, 2007.
133. C. Krempaszky, J. Ocenasek, V. Espinoza, P. Tsipouridis, E. Werner, T. Hebesberger, and A. Pichler, "*Micromechanical Modeling of the Formability of Advanced High Strength Steels.*" International Conference on New Developments in Advanced High-Strength Sheet Steels, Orlando, FL, USA, pp. 305-314, 2008.
134. J. Hoon Kim, Myoung-Gyu Lee, Robert H. Wagoner, David K. Matlock, "*Hole expansion formability of dual-phase steel using representative volume element approach with boundary-smoothing technique*", Materials Science & Engineering, 2010.
135. X. Wu, C. Xie, H. Bahmanpour, and J. Bai, "*Microstructure Characterization of Dual Phase Steels and Its Representation in A Meso-Scale Formability Simulation Method*", Plasticity 2009, St Thomas, Jan 3-8, 2009.
136. W. N. Liu, K. S. Choi, X. Sun, and M. A. Khaleel, "*Modeling of Failure Modes Induced by Plastic Strain Localization in Dual Phase Steels.*" SAE World Congress, vol 2008-01-1114, SAE, Detroit, MI, USA, pp. 1-7, 2008.
137. J.L. Duncan, R. Sowerby & E. Chu, "*The Development of Sheet Metal Modeling*", Computer Modeling of Sheet Metal Forming Process, N.M. Wang and S.C. Tang, eds., The Metallurgical Society, Warrendale, PA, pp. 1-11, (1986).
138. J. Mulder, J. Novy, H. Vegter, "*Analytical and numerical simulation of deep drawing and ironing*", Proc. of Numisheet 2011, Seoul, Korea, August, 2011.
139. Proc. of NUMlSHEET2011 Benchmark, Seoul, Korea, August, 2011.
140. D.M. Woo, "*On the Complete Solution of the Deep Drawing Problem*", Int. J. Mech. Sci., Vol.10 (1968), pp.83-94.
141. B. Kaftanoglu and B. Kilkis, "*Theory of Deep-Drawing of Square Blanks and the Numerical Solution of the Flange Regions*", Memorires Scientifiques Revue Metallurgic, pp. 525-534, (1980).
142. B. Avitaur, "*Metal Forming : The Application of Limit Analysis*", Marcel Dekker, 1980.
143. W. Johnson, R. Sowerby, and R.D. Venter, "*Plane Strain Slip Line Field for Deformation Processes",* Pergamon Press, Oxford (1982).
144. R. Hill, "*The Mathematical Theory of Plasticity"*, Oxford University Press (1950).

145. R. Sowerby, "*The Modeling of Sheet Metal Forming Processes*", Interdisciplinary Issues in Materials Processing and Manufacturing, ASME, pp.131-137, (1987).
146. R. Sowerby, N. Chandrasekaran, X. Chen, M. Rooks and P. Correa, "*The Development of Computer Aids for Sheet Metal Stampings*", CAD/CAM & FEM in Metal Working, S.K. Ghosh & A. Niku-Lari ed., Pergamon Press, (1988).
147. V. V. Hazek, and K. Lange, "*Use of the slip line field method in deep drawing large irregular shaped components*", Proc. 7th NAMRC, Ann Arbor, MI, U.S.A. pp.65-71, SME, Lyon (1979).
148. T. Jimma, "*Earing of deep drawn cylindrical cups*", Plastic properties and machining, 11, pp.707 (1970-71), (in Japanese).
149. H. Gloeckl and K. Lange, "*Computer Aided Design of Blanks for Deep Drawing Large Irregular Shaped Components*", Proc. 11th NAMRC, Madison, Wisconsin, U.S.A. pp.243-251, AMRI of SME, Lyon (1983).
150. Szczepinski, W., *Introduction to the Mechanics of Plastic Forming of Metals*, PWN-Polish Scientific Publishers, Warszawa (1979).
151. J.H. Vogel, J. Amoedo and D. Lee, "*An Integrated Process Design Method for Sheet Material Forming*", Proc. of IDDRG, (1988), U.S
152. X. Chen, R. Sowerby, "*The Development of Ideal Blank Shapes by the Method of Plane Stress Characteristics*", The International Journal of Mechanical Science, Vol.34, No.2, pp159-166, 1992.
153. X. Chen, R. Sowerby, "*Comparison of Different Methods on the Analysis of Cup Drawing*", Proc. 17th International Deep Drawing Research Group Biennial Congress, Beijing, (1990).
154. X. Chen, R. Sowerby, "*Blank Development and the Prediction of Earing in Cup Drawing*", The International Journal of Mechanical Science, Vol.8, No.5, pp509-516, 1996.
155. M. Kamura, Yoshinobu Omiya, Jody Shaw, Ming Chen, "*Formability and Spring Back Characterization of Advanced High Strength Steel*", SAE Technical Paper, 2003-01-0522.
156. H. Iseki and T. Murota, "*On the determination of the optimum blank shape of non-axisymmetric drawn cup by the finite element method*", Bulletin of JSME, Vol.29, 1986, pp.1033-1040.
157. R. Hill, "*The theory of the yielding and flow of anisotropic metals*", Proc. Roy. Soc., A198, 281 (1984).
158. A. Ralston and P. Rabinowitz, "*A first course in numerical analysis*", McGraw-Hill (1978).